Optimizing the CVD-plasma for On-chip Spectrometers

Process Development Using ICP-CVD Parameter Tuning

AP3902: Master Thesis Applied Physics

Jurre Heeringa

Delft University of Technology

TU Delft

Optimizing the CVD-plasma for On-chip Spectrometers

Process Development Using ICP-CVD Parameter Tuning

by

Jurre Heeringa

to obtain the degree of Master of Science
at the Delft University of Technology,
to be defended publicly on Tuesday 2 September, 2025 at 14:00 AM.

Student number:	6096093	
Project duration:	October 7, 2024 – July 25, 2025	
Thesis committee:	Dr. A. Endo,	TU Delft, Supervisor
	Prof. dr. ir. J.J.A. Baselmans,	TU Delft, Examiner
	Dr. S. Goswami,	TU Delft, QuTech, Examiner
	Ir. L.G.G. Olde Scholtenhuis,	TU Delft, Daily supervisor

Cover: Schematic representation of an Inductively Coupled Plasma-Enhanced Chemical Vapor Deposition (ICP-CVD) process.

An electronic version of this thesis is available at `http://repository.tudelft.nl/`.

TU Delft

Abstract

Uncovering the formation history of dusty star-forming galaxies in the early universe requires wide-band spectroscopic instruments capable of detecting redshifted emission lines in the millimeter and submillimeter regime. The on-chip spectrometer DESHIMA 2.0 addresses this by integrating filterbanks and kinetic inductance detectors (KIDs) onto a single chip, enabling wide frequency coverage in a compact footprint. However, performance is currently limited by losses in the dielectric layer of its microstrip lines, which reduce transmission efficiency and sensitivity. Minimizing these losses is crucial not only to enhance signal throughput but also to enable the use of parallel-plate capacitors (PPCs), which significantly reduce resonator size, increase detector count, and thus improve spectral resolution. Achieving low-loss dielectric films is therefore essential for the next generation of high-resolution spectrometers such as TIFUUN.

To support this development, this thesis focuses on optimizing the deposition of hydrogenated amorphous silicon (a-Si:H) films using Inductively Coupled Plasma Enhanced Chemical Vapor Deposition (ICP-CVD). These films function as dielectric layers in both microstrip lines forming the filterbank (90–360 GHz) and in PPCs (1–10 GHz).

Since direct measurement of dielectric losses was beyond the scope of this project, optimization was based on properties known to correlate with loss mechanisms—namely two-level systems (TLSs) and absorption in the vibrational tail. TLSs are expected to dominate at PPC operating frequencies, while vibrational absorption is more relevant in the filterbank. The optimized properties include residual stress, thickness non-uniformity, optical and infrared refractive index, band gap, void-volume fraction, hydrogen content, and microstructure parameter.

A Taguchi L18 orthogonal array was used to systematically vary seven deposition parameters: table temperature, silane flow rate, ICP power, table RF power, gas ratio (silane/argon), pressure, and native oxide removal method (argon milling vs HF dip). Film properties were evaluated using ellipsometry, FTIR spectroscopy, and a stressmeter.

ANOVA revealed table RF power as the dominant factor, with the highest contribution to five of the eight properties: thickness uniformity, refractive index, hydrogen content, microstructure, and residual stress. In the latter, increasing power shifted the film from tensile to strongly compressive regimes. Other parameters had more moderate effects: chamber pressure had strongest influence on void-volume fraction and infrared index, while silane flow rate and wafer preparation affected the band gap most significantly. Despite some models exhibiting high residuals, indicating unmodeled interactions between the parameters, the overall analysis successfully identified key relationships between the deposition parameters and the material properties.

Two optimized recipes were selected using Grey Relational Analysis, with equal weighting assigned to hydrogen content and void-related properties. Recipe 19 achieved minimal hydrogen content (4.3 at.%) and low residual stress, making it a strong candidate for minimizing dielectric losses in the filterbank. However, it also showed high void fraction and surface inhomogeneity. Recipe 20, aimed at maximizing hydrogen content, reached 16.3 at.% but showed only average performance and suffered from high compressive stress (–745 MPa). As a more robust alternative, Recipe 9 offered low void content, moderate hydrogen level, favorable stress (+125 MPa), and good uniformity—making it the most practical candidate for integration into both filterbank and PPC structures.

Future work should focus on direct measurement of dielectric loss tangent and TLS density under cryogenic conditions to validate the predicted performance in superconducting spectrometers.

Acknowledgements

First, I want to thank Akira and Leon for supervising me throughout this thesis. Akira's enthusiasm for the capabilities for the on-chip spectrometer was contagious and one of the key reasons I chose to do my thesis within this research group. A special thanks goes to Leon, my daily supervisor, it was a real pleasure to work with him. He has an outstanding ability to respond to questions in a logical yet critical way, which I found truly inspiring. On top of that, his constant availability and his natural way of ending a brainstorm session with a laugh, made working together very enjoyable.

I also want to thank the entire Terahertz Sensing group for creating such a friendly environment, it was a pleasure to be part of it. A special thanks to the other master students I shared the office with: Tycho, Pieter, Marick, Peijun and Lorenzo, for the many fun coffee breaks and the laughs we shared along the way.

A special thanks to Paolo for all the advise he shared during the times we met in the cleanroom. His expertise helped me to work more efficiently or gave me new insights. He regularly surprised me with a joke, which made it fun to be around him. On top of that, he also grew a thermal oxide layer on my wafers, which was an essential step in my processing, so literately could not have done this without him.

I would also like to thank my friends from both Medemblik and Delft, and my housemates for always being there, whether it is for a good conversation or just for having some laughs.

Last but not least, I want to give my special thanks to my girlfriend Jutta, my parents Andre and Nelly-An, and my sisters Roos and Nienke. Not only their support during this project, but for simply being the amazing people they are. I am grateful to have them in my life.

The use of Artificial Intelligence during the Master Thesis Project is permitted, provided it is explicitly acknowledged. Therefore, I want to state that I have made use of OpenAI's ChatGPT models to generate critical feedback on the text of my thesis. Additionally, I have used these models to solve errors in my Python code and to generate code, which I have thoroughly checked for correctness.

Contents

List of Figures

List of Tables

1

Introduction

1.1. Wideband spectroscopy at millimeter wavelengths to uncover galaxy evolution in the early universe

More than half of all the stars that are born through the history of the universe were formed in dusty star-forming galaxies (DSFGs) [1]. Therefore, constructing a map that contains the distribution of these galaxies in the early universe is an important part of the puzzle how the early universe evolved. However, because these galaxies are heavily obscured by dust, they appear faint or are invisible at optical wavelengths [1]. Luckily, the cool interstellar gas within DSFGs, from which stars are born, does emit radiation at specific frequencies known as emission lines. Lines such as [CII] have emission frequencies above 1.0 THz, but due to the high redshifts of DSFGs, they are observed in the millimeter-to-submillimeter range (0.1–1 THz). These emission lines provide crucial information about a galaxy's kinematics, star-forming activity, and are essential for determining its redshift [1].

Especially, measuring the redshift is important for generating a map of the early universe. As the Universe is expanding, it stretches the wavelength of the light that travels from the galaxy to the telescope. This shift in observed frequency, caused by the galaxy's distance and the expansion of space, is known as redshift. Measuring these redshifts allows us to determine how far back in time we are observing, and is crucial for building a three-dimensional view of galaxy formation across the history of the universe.

While large surveys in the submillimeter range have found many dusty star-forming galaxies, identifying their redshifts remains challenging. Traditional optical and near-infrared methods often fail because the dust blocks much of the light at those wavelengths. Submillimeter spectrometers, on the other hand, typically observe only a narrow range of frequencies at a time. As a result, finding the redshift of a galaxy often requires many separate observations, which makes the process slow and inefficient [2]. To overcome this, we need an instrument that can observe a wide range of frequencies simultaneously, with enough sensitivity and resolution to detect the emission lines from these galaxies directly [1].

To enable fast and efficient redshift measurements, the DESHIMA project (DEep Spectroscopic HIgh-redshift MApper) was initiated to develop a compact, chip-based spectrometer. It is designed to detect faint emission lines from dusty galaxies with high sensitivity and spectral resolution. The current version, DESHIMA 2.0, operates over a wide frequency range of 220–400 GHz, enabling the observation of galaxies at redshifts between 3.7 and 7.6 based on the [C II] 1.90 THz line [3]. With 347 spectral channels and a resolving power of $R = \frac{f}{df}$ ~500 (where f is the measured frequency and df the smallest distinguishable frequency difference) DESHIMA 2.0 can capture a broad spectral range in a single observation. This allows for simultaneous identification of redshifts and detection of multiple lines, even when operated on a single-dish telescope such as ASTE [3]. The heart of the instrument is an integrated superconducting chip, described in more detail below.

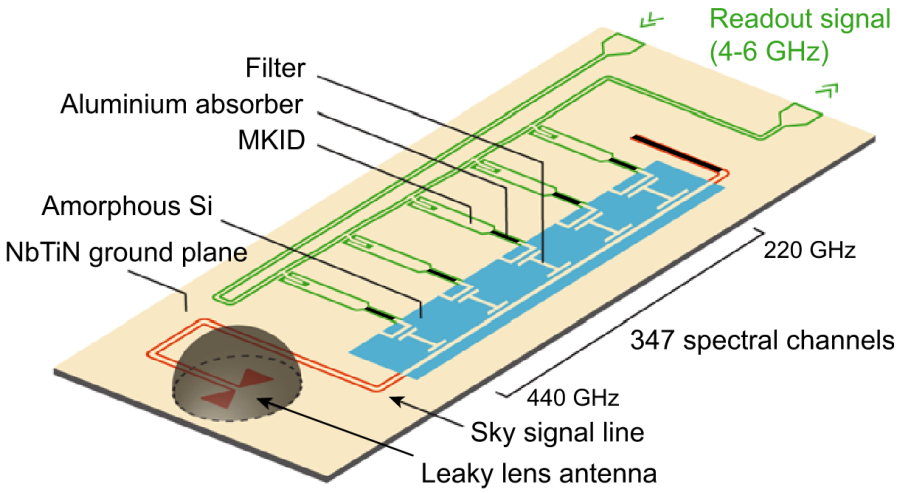

Figure 1.1: Design of the DESHIMA 2.0, a filterbank spectrometer chip. This figure features the antenna, sky signal line, filterbank, MKIDs and the readout line. The sky signal including both astronomical and atmospheric emission is coupled by an antenna and is guided to the filterbank over a transmission line. Each filter connects with an MKID, and the change in the resonance frequency by incoming photons is measured through a single readout signal. Figure is adapted from [3]

1.2. DESHIMA: On-chip filterbank spectrometer

The terahertz on-chip filterbank spectrometer is implemented on a single superconducting chip, shown in Figure 1.1. The chip consists of an antenna coupled to a transmission-line filterbank, with a microwave kinetic inductance detector (MKID) placed behind each filter. All detectors are read out simultaneously using frequency division multiplexing, at the microwave frequency range (4-6 GHz) [2].

The operation of the spectrometer works as follows: incoming radiation is absorbed by the antenna and guided via a coplanar waveguide (CPW) to the filterbank. This guiding structure, often referred to as the sky signal line, transports the astronomical signal across the chip. At the start of the filterbank section, the CPW transitions into a microstrip line that forms the basis of the filter structure. This microstrip consists of three layers: a superconducting NbTiN ground plane, a narrower NbTiN signal line, and a thin film of either amorphous silicon (a-Si:H) or amorphous silicon carbide (a-SiC:H), which functions as the dielectric between them. This dielectric layer is of particular importance in this thesis and will be discussed in detail later.

The filterbank separates the wideband signal into multiple sub-bands, each corresponding to a narrow band-pass filter. These filters are coupled to the signal line on one side and to the MKID on the other. At its resonant frequency, each filter transmits maximum power to its associated MKID. Each MKID, a CPW microwave resonator for the depicted design, absorbs the incoming radiation, causing a shift in its resonant frequency. This shift is measured as a phase change in the transmitted readout tone, with all MKIDs connected to a common readout line [2].

1.2.1. Current limitations of DESHIMA 2.0 due to dielectric losses

The filters and (part of) the sky signal line in DESHIMA 2.0 are constructed using superconducting microstrip structures, where two NbTiN layers are separated by a thin dielectric layer, see Figure 1.2. While the use of crystalline silicon (c-Si) as a low-loss dielectric is possible through a flip-bonding technique [4], deposited dielectrics are preferred because they allow more flexible chip designs and fabrication processes [5]. However, deposited dielectrics exhibit higher dielectric losses compared to crystalline materials. As a result, part of the millimeter and sub-millimeter wave signal is absorbed within the dielectric before reaching the detector. This dielectric loss is an intrinsic material property, characterized by the loss tangent, $\tan\delta$, which describes the ratio of energy dissipated compared to the energy stored [5].

The term dielectric loss captures two mechanisms of energy absorption within the dielectric material. The first arises from the excitation of vibrational modes associated with chemical bonds in the film. These bonds can be excited to specific energies. When a photon with matching energy propagates

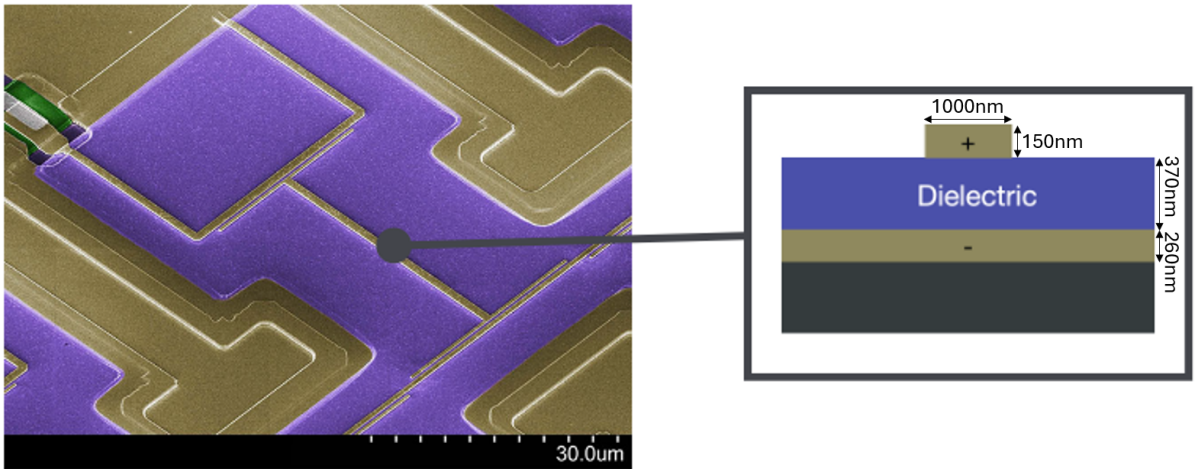

Figure 1.2: Scanning electron micrograph of a DESHIMA 2.0 filter, showing the a-Si:H dielectric layer in purple and the NbTiN superconducting layers in dark yellow. The schematic on the right shows a cross-section of the microstrip line, with layer dimensions taken from [6], [7]. Figure adapted from [5].

through the dielectric, it can excite a bond, causing it to vibrate and absorb energy from the signal [8].

The second mechanism is attributed to two-level system (TLS) losses, which are assumed to originate from microscopic defects in amorphous dielectric materials. In a disordered lattice, atoms can tunnel between two energetically similar states. TLSs couple to the electric field of the signal through their dipole moment, modifying the dielectric constant and thereby inducing absorption [9].

Both the frequency bandwidth and the resolving power R of the instrument are limited by dielectric losses, as increasing either typically requires a longer signal path through the dielectric. In a high-loss dielectric, it is not possible to achieve wide bandwidth and high resolving power at the same time. For example, achieving a wide bandwidth with low transmission loss is only possible when R is low, since this reduces the number of required channels and shortens the length of the sky signal line [5].

The deposition of dielectric films with a low-loss at millimeter to submillimeter wavelengths is also important for the TIFUUN instrument, which will use the technology of the DESHIMA 2.0 to construct multiple spectrometer pixels.

1.3. TIFUUN

A key challenge in millimeter and sub-millimeter astronomy is mapping large cosmic volumes with sufficient spectral resolution to study the evolution of matter across cosmological timescales [10]. The TIFUUN imaging spectrometer is being developed as an instrument that can be adapted to a broad range of science cases, including but not limited to line intensity mapping (LIM) of redshifted emission lines. By targeting key tracers of star formation and the interstellar medium, such as emission lines [C II] and [O III], TIFUUN aims to measure the dust-obscured star formation in the early universe [11].

TIFUUN stands for Terahertz Integral Field Unit with Universal Nanotechnology. An Integral Field Unit (IFU) is used in astronomy to observe a large area of the sky simultaneously, using a technique known as integral field spectroscopy. In this method, the signal from each spatial pixel is directed to a dedicated spectrometer, producing a spectrum for every pixel. Since each pixel observes a slightly different region of the sky, the combination of all spectra forms a 2D spatial image with a third spectral dimension [12].

A schematic of TIFUUN is shown in Figure 1.3. The incoming mm/submm radiation is collected by a wideband leaky-lens antenna array. Each antenna is connected to a unit spaxel on the IFU wafer, which contains a filterbank coupled to kinetic inductance detectors (KIDs). The bandpass filters separate the broadband signal into spectral channels, and the KIDs convert each filtered signal into a frequency-multiplexed readout tone. The IFU wafer contains a densely packed array of pixels, which allows for spectral mapping. The design of TIFUUN is adaptable and can be optimized for specific science goals.

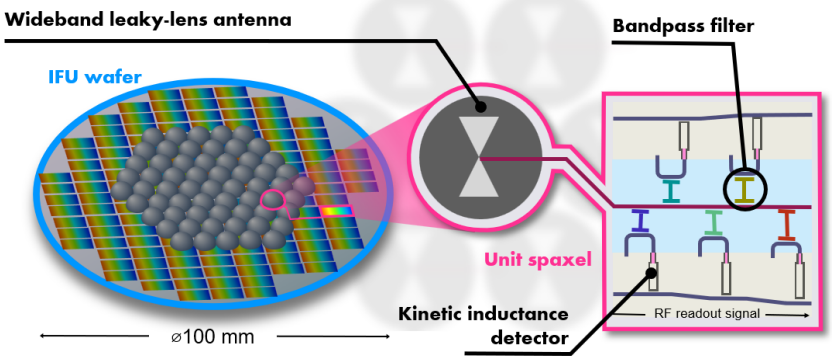

Figure 1.3: Schematic of the TIFUUN imaging spectrograph, which uses the technology of DESHIMA 2.0. Incoming radiation is collected by an array of leaky-lens antennas, with one antenna per spaxel. Each spaxel consists of its own filterbank that spectrally separates the signal, followed by kinetic inductance detectors (KIDs) that convert the filtered signals into readout tones.

1.3.1. Current limitations of TIFUUN due to dielectric losses

The current design of TIFUUN faces two limitations that could be improved by reducing losses in the deposited dielectric. The first is identical to the limitation observed in the DESHIMA design; dielectric losses within the microstrip structures of the filterbank. Since the signal from each pixel propagates through this filterbank, similar dielectric losses occur. By lowering the loss tangent, a greater fraction of the signal reaches the detector, enabling an increase in both the frequency bandwidth and the resolving power R [5], [11].

The second limitation lies in the packing density of TIFUUN. Since the entire architecture must fit onto a 4-inch wafer, the available design space is strictly limited. This sets a limit on the number of KIDs that can be integrated. Ideally, the number of KIDs should be maximized to increase the number of spectral channels per spaxel. To fit more KIDs within the same area, their size must be reduced. One effective approach is to replace the current coplanar waveguide (CPW) resonators (based on a planar structure) with parallel-plate capacitor (PPC) resonators, which are drastically smaller in size [9]. However, the deposited dielectric required for fabricating a PPC is expected to increase dielectric losses in the resonator, as discussed in more detail in the next section.

1.4. Parallel-plate capacitors: Applications and limitations

1.4.1. Application in TIFUUN

As described above, current resonator designs are based on planar structures such as coplanar waveguides (CPWs). These provide low capacitance per unit area because the electric fields extend into the surrounding air and substrate. Additionally, the gap between the center conductor and ground planes is relatively large—around 50 µm [2]—which further limits the capacitance. In contrast, PPCs confine nearly all electric field lines between two metal layers, separated by a dielectric film a few hundred nanometres thick [9], as shown in Figure 1.5. This configuration increases field confinement and significantly raises the capacitance per unit area. As a result, PPCs reduce radiative losses and allow for a more compact resonator footprint [9]. Figure 1.4 compares CPW-KIDs with PPC-KIDs.[1] Replacing CPWs with PPCs could increase the detector count from 5,000 to approximately five times that amount on the same wafer [11], thereby increasing the number of spectral channels per spaxel.

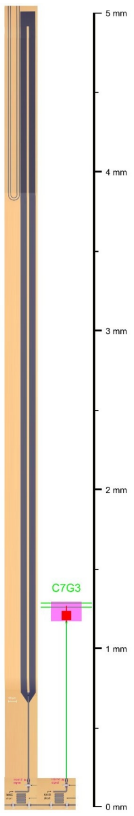

Figure 1.4: Comparison between a the size of the DESHIMA-style CPW-MKID (left) and the proposed PPC-KID design (right). Image adapted from [13].

[1] Note that the PPC-KID layout is still under development. This schematic does not represent the final TIFUUN design. In particular, the filter section (bottom) and the readout coupler (top) are outdated.

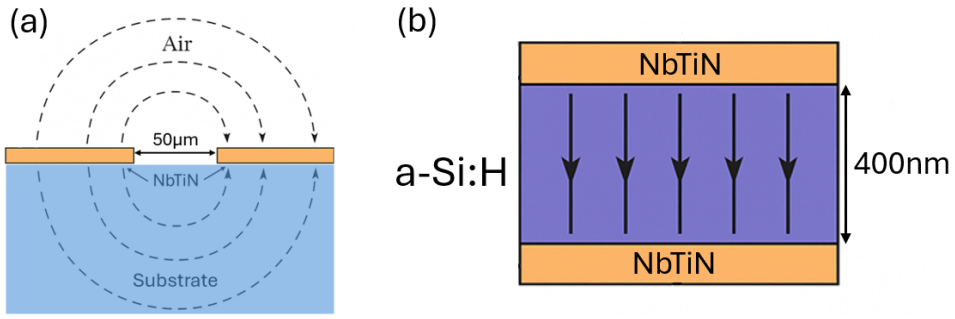

Figure 1.5: Schematic illustrating the structural difference between a coplanar waveguide (a) and a parallel-plate capacitor (b).

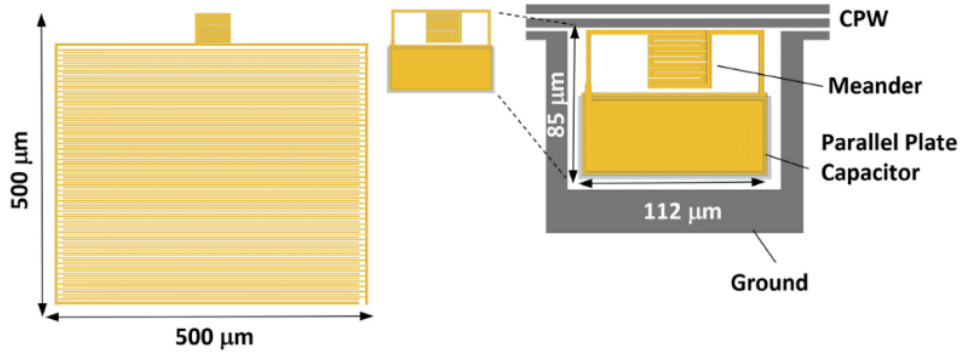

Figure 1.6: Left: Sketch of a interdigitated capacitor-based LEKID. Right: Sketch of a parallel plate capacitor based LEKID. For comparison, both use the same meander and are designed to resonate at the same frequency. At this frequency, a parallel-plate capacitor LEKID using a 25 nm-thick Al2O3 dielectric allows to strongly reduce the size of pixels by a factor 26. Figure is adapted from [15].

1.4.2. Application in optical KID arrays

On-chip spectrometers are also used in the optical frequency range, where an alternative detector design is applied. Instead of CPW-KIDs, these designs use Interdigitated Capacitor–Lumped Element Kinetic Inductance Detectors (IDC-LEKIDs). This approach is significantly different, as IDC-LEKIDs consist of an inductive line and an interdigitated capacitor (IDC), shown on the left side of Figure 1.6. The photon-sensitive element is the inductor, thus no antenna structures are needed to couple incoming radiation into the resonator [14]. Additionally, a separate filterbank (like the one in Figure 1.1) is not required. The optical photons carry sufficient energy to enable individual photon counting. In this approach, the photon energy is extracted from the peak amplitude of the signal, meaning the 'filtering' is performed during data analysis. The resonance frequency of each KID is defined by the finger lengths of the interdigitated capacitor (IDC), allowing to distinguish between the signals from different KIDs on the frequency-multiplexed readout line.

Similar to the CPW-KID, absorption of radiation by the inductor causes a shift in the resonator's frequency, which is detected as a phase change in the readout tone. However, since the IDC is also a planar structure (like CPW), it has a similar low capacitance per unit area. Replacing the IDC with a parallel-plate capacitor (PPC) would significantly reduce the capacitor size, and thus the overall size of the (PPC-LE)KID. A comparison between the IDC- and PPC-based designs is shown in Figure 1.6.

1.4.3. Current limitation of parallel-plate capacitor

Unfortunately, implementing PPCs with deposited dielectric films is likely to introduce higher dielectric losses and increased frequency noise levels compared to planar structures like CPWs and IDCs.

TLSs can couple to the electric field of the resonator via their electric dipole moment, thereby modifying the material's dielectric constant. The real part of this contribution shifts the resonant frequency, while the imaginary part increases microwave loss. Moreover, TLSs can randomly switch between states, resulting in time fluctuations in the dielectric constant. These fluctuations cause the resonant frequency to fluctuate over time, contributing to frequency noise [9].

1.5. State of the art

1.5.1. Fabrication technique: Plasma Enhanced Chemical Vapor Deposition

For the fabrication of a PPC, a commonly used technique to deposit the dielectric material is Plasma-Enhanced Chemical Vapor Deposition (PECVD). This thin-film deposition method uses plasma to enhance surface chemical reactions, allowing material growth on a substrate. The process takes place in a vacuum chamber, where the substrate is placed on a heated electrode. A gas mixture of precursors is introduced, and a radio-frequency (RF) electric field is applied between electrodes to generate a plasma. This plasma breaks the gas molecules into reactive components that interact with the substrate, forming a thin film [16].

The plasma enhances the chemical reactions, allowing for deposition at significantly lower temperatures compared to traditional CVD processes. The PECVD process also enables control over various parameters, such as gas flow rates, chamber pressure, RF power, and temperature, allowing for fine-tuning of the properties of the deposited film [16].

An advanced version of this technique is Inductively Coupled Plasma-Enhanced Chemical Vapor Deposition (ICP-CVD). The key difference lies in the method of plasma generation: while conventional PECVD excites the plasma capacitively by applying an RF voltage across two electrodes inside the chamber, ICP-CVD uses RF coils placed around the chamber to inductively generate plasma. This inductive coupling results in higher plasma densities, reduced ion bombardment on the film surface, and improved homogeneity of the deposited layer compared to PECVD [17].

1.5.2. State of the art dielectric losses

The research group where is thesis is part of, the Terahertz Sensing Group, has investigated potential low-loss deposited dielectric materials and identified hydrogenated amorphous silicon carbide (a-SiC:H) as a promising candidate. These films were fabricated using a PECVD system located at the Else Kooi Laboratory at TU Delft. As of their 2022 publication [18], these films demonstrated the lowest reported low-power sub-kelvin dielectric losses for microstrip resonators at both millimeter–submillimeter frequencies (tan δ of 1.2×10^{-4} at 350 GHz) and microwave frequencies (tan δ of 3×10^{-5} at 7 GHz), as shown in Figure 1.7. With these losses, the IDC-based resonator design in [19] can be replaced by an a-SiC:H PPC, reducing the KID footprint by a factor of 10—though at the cost of approximately 20 dB increased frequency noise [9].

During his PhD, Bruno Buijtendorp investigated the origin of dielectric loss in a-SiC:H [5]. He demonstrated that the absorption tail of vibrational modes located above 10 THz can account for the measured infrared loss data in the 270–455 GHz range. At cryogenic temperatures and frequencies below 200 GHz, the dominant loss mechanism is expected to transition to be dominated by TLSs. He further noted that similar vibrational features in the 10–30 THz range are also present in a-Si:H, suggesting it contains a comparable crossover in loss mechanism.

Roughly a year after these findings, a study was published reporting a dielectric material with even lower microwave losses than previously found in the literature: a loss tangent of 7×10^{-6} at 7 GHz [20]. In this study, several recipes for depositing a-Si:H, rather than a-SiC:H, were tested across various deposition systems. The recipe that achieved the lowest dielectric losses within a PPC structure was fabricated using the ICP-CVD technique.

1.6. Research goals

Although the authors of [20] demonstrated a further reduction in microwave losses within their dielectric material, they do not report how the conditions within the deposition chamber influence the resulting film properties. Consequently, they emphasize the need for future research into the dependence of dielectric losses onto the deposition parameters [20].

At the Else Kooi Laboratory, an ICP-CVD machine is available, which I have used to address this future research. In this project, I have systematically investigated how the deposition conditions affect the properties of the dielectric film. The goal was to gain a deeper understanding of the relationship between deposition parameters and material properties, in order to develop new films with specific characteristics.

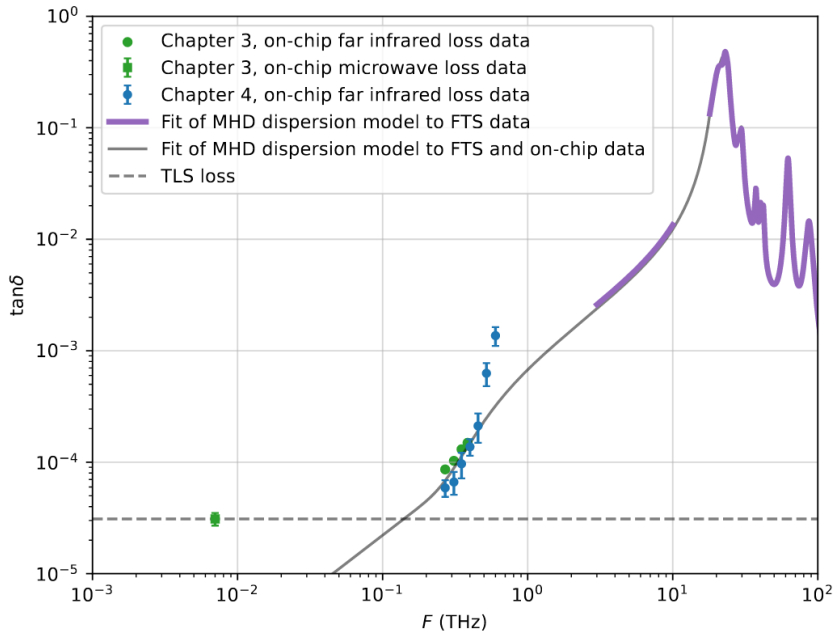

Figure 1.7: The loss tangent tan δ as a function of frequency for a-SiC:H is shown. The solid grey curve represents the tan δ obtained by fitting a Maxwell–Helmholtz–Drude (MHD) dispersion model to the vibrational modes and infrared loss data. The intersection between the solid grey curve and the horizontal dashed line indicates the crossover point between low-power cryogenic TLS loss and the loss associated with vibrational modes. Figure adapted from the dissertation of Bruno Buijtendorp [5].

Improving these dielectric properties is particularly relevant for on-chip spectrometers such as DESHIMA and TIFUUN. First, reducing losses in the microstrip filterbank would improve signal transmission to the KIDs. Second, replacing the current CPW-KIDs with PPCs that are an order of magnitude smaller could significantly increase packing density. Similarly, optical KID arrays could also benefit from compact PPC geometries, allowing for smaller designs while minimizing the increase in microwave losses [20].

This led to the following research goal:
Optimize the material properties of a-Si:H films for usage within on-chip spectrometers by adjusting the recipe of the ICP-CVD machine.

This goal can be subdivided into the following objectives:

- **Relate film properties to expected dielectric loss performance.**
- **Establish the relations between various deposition parameters and the film's properties.**
- **Assign and test the recipe with the best expected cryogenic performance.**

Directly measuring the dielectric losses of the film would require constructing a complex cryogenic setup, which is beyond the scope of this project. However, literature has proposed correlations between several material properties and dielectric losses. Chapter 4 presents these material properties and describes the methods used to compute them.

To relate the film properties of the a-Si:H dielectric to the deposition parameters of the ICP-CVD, I ran multiple deposition recipes. In total, seven deposition parameters were varied: Table Temperature, Silane Flow Rate, Gas Ratio between Silane and Argon, ICP Power, Table RF Power, Pressure, and Wafer Preparation. For the Wafer Preparation, I compared an HF dip with Argon milling. For the other six parameters, I selected at least three levels to identify possible optimal regions. Testing all combinations would require $2 \cdot 3^6 = 1458$ experiments, which is clearly impractical. Therefore, I implemented a Design of Experiments (DoE) approach, called the Taguchi method.

The orthogonal structure of the Taguchi design enables the generation of Main Effect Plots, which show how each individual parameter influences the material properties. Additionally, I performed Analysis of Variance (ANOVA), a statistical method to compute the percentage contribution of each parameter, allowing identification of the most influential deposition parameters.

Since the goal is to optimize multiple material properties simultaneously, I applied Grey Relational Analysis (GRA), which captures the performance of all properties into a single Grey Relational Grade. Performing ANOVA and generating Main Effect Plots on this combined variable allows me to identify the most influential parameters for all loss-related properties combined. The corresponding Main Effect Plot indicates which recipe has the best overall performance.

2

Theory

2.1. Operations of the ICP-CVD

Inductively Coupled Plasma Chemical Vapor Deposition (ICP-CVD) is a widely used technique for fabricating high-quality thin films. In Chemical Vapor Deposition (CVD), reactive precursor gases are mixed into a vacuum chamber, where they undergo chemical reactions on the substrate surface to form a solid film. In ICP-CVD, a plasma is generated by inductively coupling RF (radio-frequency) power into a coil placed around the top of the chamber. A key feature of the ICP-CVD system is the separation between plasma generation and substrate bias, allowing independent tuning of ion density and ion energy. This enables better control over film properties such as thickness non-uniformity and residual stress.

The ICP-CVD system used in this work, the Oxford Instruments PlasmaPro 100 ICPCVD (see Figure C.1), is equipped with a load lock to prevent contamination of the main chamber. After the wafer is loaded into the load lock, the pressure is lowered to closely match the vacuum level of the process chamber. The wafer is then transferred and placed on the substrate electrode. A schematic of the ICPCVD system is shown in Figure 2.1. The precursor gases are introduced, with adjustable flow rates, either through the top inlet or via gas rings positioned above substrate electrode. The RF coil creates an oscillating magnetic field, which induces electric fields that ionizes the precursor gasses, forming a plasma. A second RF source connected to the substrate electrode sets an independent bias on the substrate, controlling the ion bombardment energy during film growth.

Key Components of the ICP-CVD System: [21]

- **ICP RF Power System:** An RF generator operating at 13.56 MHz supplies power to the inductively coupled plasma coil, which is located at the top of the deposition chamber. The generator produces a high-frequency current that flows through the coil, generating a time-varying magnetic field. This magnetic field induces an electric field in the gases within the chamber, energizing electrons and creating a high-density plasma.
- **Substrate Electrode:** The lower electrode, on which the wafer is placed, is connected to a second 13.56 MHz RF generator that applies an independent bias to the substrate. This bias controls the energy of ions bombarding the wafer surface during deposition. The electrode is also temperature controlled and can be heated up to 400°C, allowing to control the temperature of the wafer throughout the process.
- **Auto Matching Unit (AMU):** The impedance of the RF generators is fixed, whereas the impedance of a plasma varies according to conditions of the chamber. If uncorrected, the impedance mismatch would cause poor energy transfer between the generator and the plasma. Each RF generator therefore uses an AMU to continuously minimize the reflected power. This results in improved plasma stability and consistent process performance.

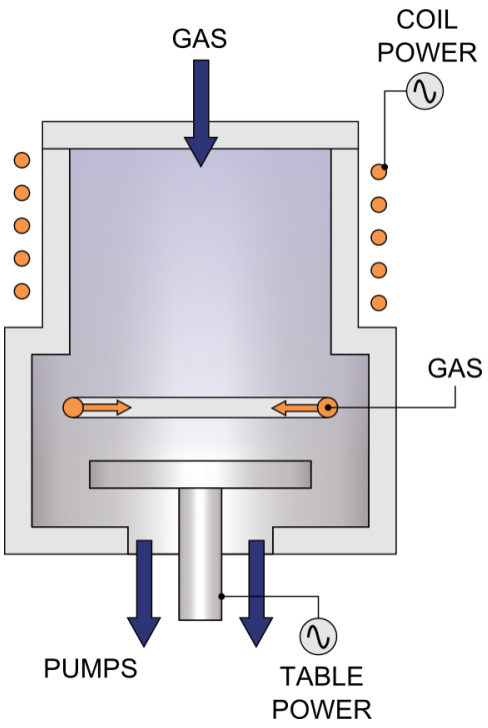

Figure 2.1: Schematic of the ICP-CVD machine, adapted from [22]. A picture of the deposition system used in this work is shown in Figure C.1. Precursor gases can enter the deposition chamber either from the top inlet or from a gas ring positioned just above the wafer stage, with adjustable flow rates. Inductively coupled RF power is applied via a coil around the top of the chamber, ionizing the gases to form a plasma. The wafer is placed below the gas ring on top of an electrode, which is connected to a second RF power source to control the ion bombardment energy. In addition, the electrode is temperature controlled.

2.2. Stressmeter

During chemical vapor deposition, stresses can build up during film growth. Such stresses are generally undesirable, as they can compromise the mechanical stability of the film. The residual stress can either be tensile or compressive. Tensile stress is considered positive and tends to pull the film apart, potentially leading to cracking or delamination. Compressive stress is considered negative and pushes inward, which may cause buckling. For a-Si films deposited using a PECVD tool on a c-Si wafer with a 200 nm silicon oxide layer, Johlin et al. [23] estimated that buckling and delamination failures occur at approximately -1200 MPa and +450 MPa, respectively. Since avoiding these failure modes is critical for my deposited films, these values provide a benchmark to assess whether the measured stress levels approach failure thresholds.

The type of stress present in a thin film depends on its microstructure, see Figure 2.2. If, during growth, the atoms are packed more closely than their equilibrium spacing, they exert outward forces on each other, resulting in compressive stress. On the other hand, if isolated islands form with missing atoms in between, attractive forces develop in the material, leading to tensile stress [24].

The total stress, σ_{tot}, present in a thin film is the combination of three components [25], [26]. First, external stress, σ_{ext}, which is due to external loading. Second, thermal stress, σ_{th}, generated by differences in the thermal expansion coefficients between the film and the substrate during temperature changes. Third, intrinsic stress, σ_i, which is related to the film's structure. This intrinsic stress is linked to factors such as the type of bonding between the film and substrate, the impact of bombardment during deposition, and the growing process itself [26].

$$\sigma = \sigma_{ext} + \sigma_{th} + \sigma_i \tag{2.1}$$

The thermal component can be estimated by [25], [26]:

$$\sigma_{\text{th}} = E_f(\alpha_f - \alpha_s)(T_d - T_m) \tag{2.2}$$

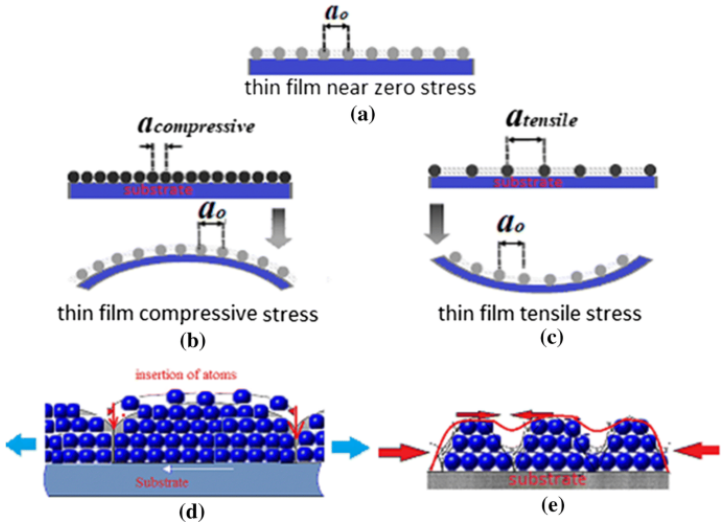

Figure 2.2: Schematic of the origin of tensile and compressive stress in thin films. Adapted from [24].

where T_d is the temperature during deposition, T_m is the temperature at which the stresses are measured, E_f is the film Young's modulus, while α_f and α_s represent the thermal expansion coefficients of the film and substrate, respectively.

When no external load is applied, the residual stress in the film can be considered the sum of the σ_{th} and σ_i [25], [26]:

$$\sigma_r = \sigma_{th} + \sigma_i \tag{2.3}$$

To compute the residual stress on the wafer, I have used the Stoney equation adapted from [25], [26],

$$\sigma_r = \frac{E_s}{6(1-\nu_s)} \cdot \frac{t_s^2}{t_f} \left(\frac{1}{R_f} - \frac{1}{R_0} \right) \tag{2.4}$$

where E_s is the Young's modulus, υ_s the Poisson's ratio, t_s the thickness of the substrate, t_f the thickness of the film, R_0 and R_f the curvature radii of the substrate before and after the deposition.

2.3. Ellipsometry

Ellipsometry is a technique used to characterize thin films by measuring the change in polarization of light due to reflection from a sample surface. A schematic of this principle is shown in Figure 2.3, where linearly polarized light is reflected off a sample and becomes elliptically polarized (hence the name 'ellipsometry'). The incoming beam is composed of two orthogonal components: p-polarized light (parallel to the plane of incidence) and s-polarized light (perpendicular to the plane of incidence). When this polarized light reflects off a sample surface, the relative amplitude and phase of these two components change depending on the optical properties and thickness of the sample layers. This change is described by the complex reflectance ratio [27]:

$$\frac{r_p}{r_s} = \tan(\Psi), e^{i\Delta} \tag{2.5}$$

where r_p and r_s are the complex Fresnel reflection coefficients for the p- and s-polarized components of light, respectively. The parameters Ψ and Δ are defined as [5]:

$$\psi \equiv \tan^{-1}\left(\left| \frac{r_p}{r_s} \right| \right), \qquad \Delta \equiv \text{phase}\left(-\frac{r_p}{r_s} \right) \tag{2.6}$$

where Ψ represents the amplitude ratio between the p- and s-polarized components after reflection, while Δ represents the phase shift difference between these components.

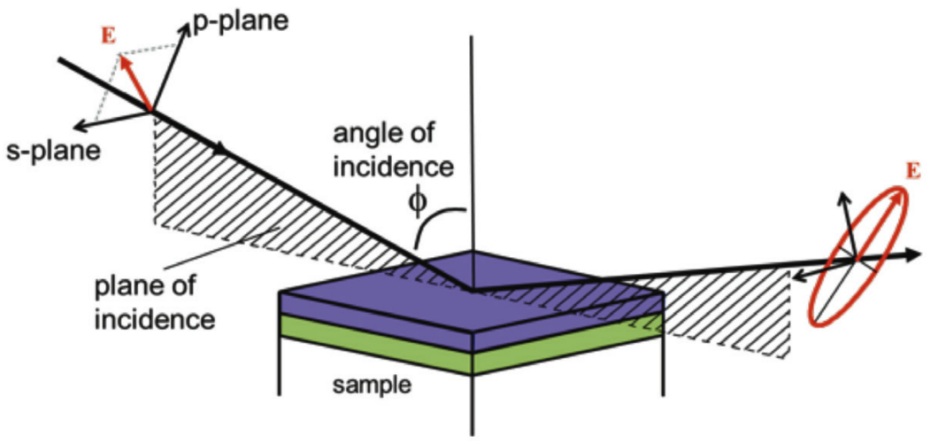

Figure 2.3: Schematic of an ellipsometry measurement, adapted from [27]. Incoming light is polarized and reflected off a sample at an angle ϕ. The polarization state of the light changes due to interactions with the sample's optical properties.

These two parameters Ψ and Δ make up the data of a ellipsometry measurement and are functions of wavelength and angle of incidence. This is why variable angle spectroscopic ellipsometry (VASE) is commonly used, where the angle of incidence and the wavelength are varied to obtain more detailed information about the sample.

In Figure 2.4, typical Φ and Δ spectra from a semi-absorbing film are shown. These spectra exhibit interference features in the transparent region. Since a-Si:H is also a semi-transparent material, the measured data display similar interference patterns.

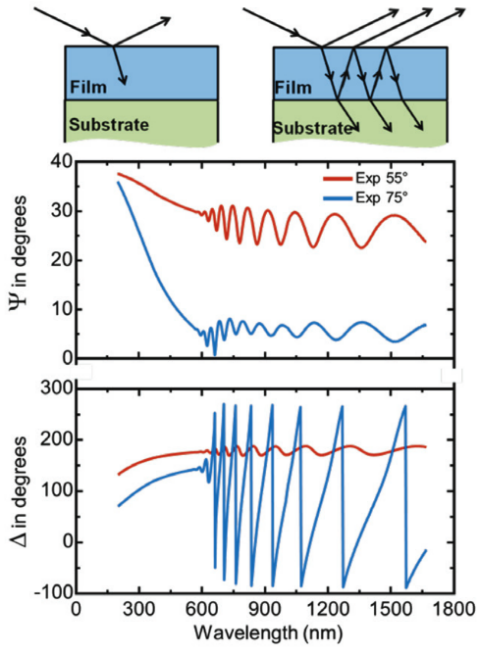

Figure 2.4: Φ and Δ spectra of a semi-absorbing film, showing interference features in the transparent region of the spectrum. Adapted from [27].

The Ellipsometer directs a beam of known polarization onto the sample at a known angle of incidence ϕ and then measures the polarization state of the reflected light. From the measured values of Ψ and Δ over a range of wavelengths, one can compute the sample's optical constants, such as refractive index n, extinction coefficient k and layer thicknesses.

To achieve this, a model of the sample is fitted to the data [27]. First, the user creates a model of the sample's structure, which includes the substrate and the thin films stacked on top. Next, the theoretical Ψ and Δ values of this model are calculated using the Fresnel equations. Finally, the model parameters, such as layer thicknesses and optical constants, are adjusted to minimize the mean squared error (MSE) between the measured and simulated data.

2.3.1. General oscillators: Cauchy, B-spline, Tauc-Lorentz and Cody-Lorentz

Cauchy:
The wavelength dependence of the refractive index for transparent films can be described using the Cauchy dispersion relation [28]:

$$n(\lambda) = A + \frac{B}{\lambda^2} + \frac{C}{\lambda^4} \tag{2.7}$$

This empirical model applies to materials with negligible absorption in the visible to near-infrared range. The parameter A sets the approximate refractive index level, while B and C define the curvature of the dispersion. The model captures the typical increase in refractive index toward shorter wavelengths observed in transparent dielectrics.

B-spline:
The B-spline model is a non-physical, but highly flexible technique to describe the complex refractive index across the full spectral range, including both transparent and absorbing regions. It consists of a series of connected splines defined at fixed wavelength intervals (knots) and fits the measured data without assuming any specific physical model. It enforces Kramers-Kronig consistency (explained in Section 2.4.2) and includes a roughness penalty to avoid overfitting. The B-spline model is particularly useful for guiding the construction of physical models, like the Tauc- or Cody-Lorentz.

Tauc-Lorentz:
The Tauc-Lorentz model, introduced by Jellison and Modine[29], provides a dispersion relation that only absorbs light above the material's band gap. It is a typically used to model amorphous materials like a-Si:H [30]. The absorption from the Tauc-Lorentz is separated into two regions[30]:

$$\varepsilon_2(E) = \frac{AE_0C(E-E_g)^2}{(E^2-E_0^2)^2 + C^2E^2} \cdot \frac{1}{E} \qquad E > E_g \tag{2.8}$$

$$\varepsilon_2(E) = 0 \qquad E \leq E_g \tag{2.9}$$

where A is the amplitude, E_0 is the peak energy, C is the broadening term, E_g is the band gap and E is the photon energy. As the model is Kramer-Kronig consistent, the real part of the dielectric function $\varepsilon_1(E)$ can be computed from $\varepsilon_2(E)$. The Tauc-Lorentz model contains five fitting parameters in total, which is an important consideration for assessing the risk of overfitting.

Cody-Lorentz:
The Cody-Lorentz model, developed by Ferlauto et al. [31], is designed to describe amorphous materials, similar as the Tauc-Lorentz model. It too includes a Lorentzian absorption with parameters A, E_0, and C, and band gap energy E_g. The main difference is in how the absorption starts just above E_g. Additionally, it can contain an Urbach tail to describe weak absorption below the band gap. The absorption from the Cody-Lorentz is separated into two regions[30]:

$$\varepsilon_2(E) = \frac{E_1}{E}\exp\left(\frac{E-E_t}{E_u}\right) \quad \text{for } 0 < E \leq E_t \tag{2.10}$$

$$\varepsilon_2(E) = G(E)L(E) = \left[\frac{(E-E_g)^2}{(E-E_g)^2 + E_p^2}\right]\left[\frac{AE_0CE}{(E^2-E_0^2)^2 + C^2E^2}\right] \quad \text{for } E > E_t \tag{2.11}$$

where $E_1 = E_tG(E_t)L(E_t)$, E_t is the offset from the band gap energy, E_p defines energy where the function transitions from Cody-type to Lorentzian absorption, and E_u defines the exponential rate of decay of the Urbach tail.

The Cody-Lorentz model is also Kramers-Kronig consistent and contains either 6 or 8 fitting parameters, depending on whether the Urbach tail is included [30]. As a result, fitting this model to the data is more complex than for the Tauc-Lorentz model, particularly when the Urbach tail is considered.

2.3.2. Effective Medium Approximation: Bruggeman Model

The Bruggeman Effective Medium Approximation (EMA) is used to model the optical properties of materials that consist of a mixture of two or more components [32]. Instead of treating each component separately, the EMA assumes that the mixture behaves as a single, homogeneous medium with effective optical properties.

For a two-component system, typically a solid material and void, the model assigns volume fractions f (void) and $1 - f$ (material), which together make up the total medium. The effective dielectric function is calculated by combining the contributions of each component, assuming that both are mixed evenly throughout the material. This method is commonly used in ellipsometry to account for surface roughness or porosity, where the structure is approximated as a mixture of a dense material and air.

2.4. Fourier Transform Infrared Spectroscopy

Fourier Transform Infrared (FTIR) spectroscopy is a technique used to characterize the optical and vibrational properties of materials. It measures the wavelength-dependent transmission of infrared light, which contains information about the material's chemical bonds.

A schematic of a typical FTIR setup is shown in Figure 2.5. Light from a infrared source is directed toward a beam splitter, which divides the beam into two paths. One part reflects off a fixed mirror, the other off a moving mirror. The two beams recombine at the beam splitter, creating an interference pattern that depends on the path length difference. This interference signal, known as an interferogram, is recorded as the moving mirror scans.

The recombined beam then passes through the sample. Specific wavelengths are absorbed by the material if they match the energy of vibrational modes, such as bond stretching or bending. These features are used to identify material composition and its chemical bonds. The remaining light reaches the detector. A Fourier transform is applied to the interferogram to reconstruct the transmitted spectrum as a function of wavelength. From the measured transmission spectra, the complex infrared refractive

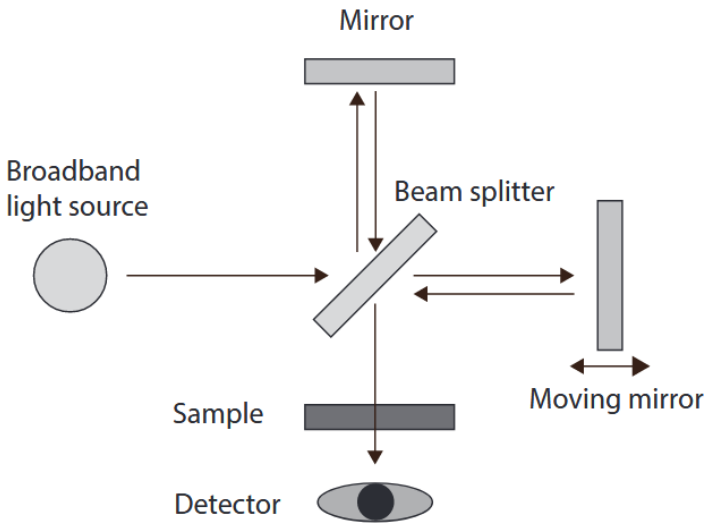

Figure 2.5: Schematic of an the setup of a Fourier Transform Infrared Spectrometer (FTIR), adapted from [5]. Light from a broadband source is split into two beams by a beam splitter. These beams reflect off a fixed mirror and a moving mirror, then recombine and pass through the sample.

index $\hat{n}$ of the a-Si:H can be computed[5]:

$$\hat{n} = n + ik \tag{2.12}$$

where the real part n is the refractive index and the imaginary part k is the extinction coefficient. From the extinction coefficient k, the absorption coefficient α can be computed:

$$\alpha = \frac{4\pi k}{\lambda} \tag{2.13}$$

where λ is the wavelength. Both n and α are wavelength dependent, which allows for identifying vibrational modes present in the film.

2.4.1. Transfer-Matrix Method

In FTIR analysis of thin films, interference from internal reflections must be taken into account. The Transfer Matrix Method (TMM) is a widely used technique to model the optical response of a sample consisting of multiple layers.

Each layer is defined by a complex refractive index $\hat{n} = n + ik$ and thickness d. For normal incidence, the optical behavior of a layer is described by a characteristic matrix that captures both propagation through the layer and boundary conditions at the interfaces. By multiplying the matrices of all layers, the total response of the stack is obtained.

Figure 2.6 shows a TMM model representing the measured samples, with forward ($a_{f,i}$) and backward ($a_{b,i}$) wave amplitudes defined at each interface. The incident wave in layer 0 has amplitude $a_{f,0} = 1$, while the reflected and transmitted waves are $a_{b,0} = r$ and $a_{f,3} = t$, respectively. The light which is transmitted through the sample is not reflected back, so $a_{b,3} = 0$. From the total matrix, the reflectance

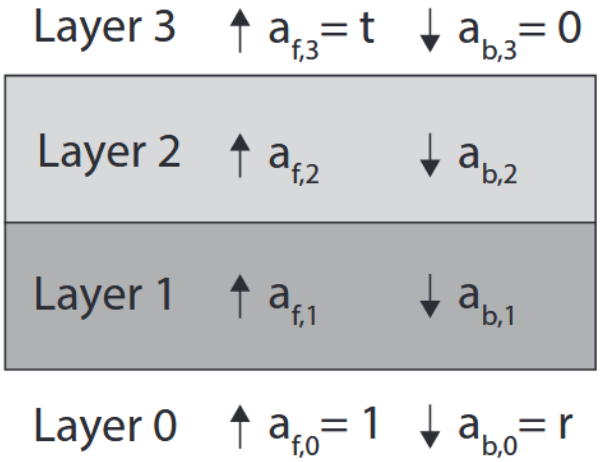

Figure 2.6: Schematic of the TMM model used to compute the infrared refractive index and absorption coefficient of the a-Si:H, adapted from [5]. Layers 0 and 3 are represent air in the chamber, and are assumed semi-infinite in the model. Layer 1 and 2 represent a-Si:H and c-Si, respectively. The light is incident on layer 0.

and transmittance spectra can be calculated. This method is applied to model FTIR transmission through a-Si:H films on c-Si substrates. By fitting the simulated transmission to the measured spectrum, the complex refractive index of the a-Si:H layer is extracted as a function of wavelength.

2.4.2. Kramers-Kronig relations

The real and imaginary parts of a material's complex refractive index $\hat{n}$ are correlated through the Kramers-Kronig relations [5]. For the complex susceptibility $\hat{\chi}$, this relation is written as:

$$\hat{\chi}(\omega) \equiv \chi'(\omega) + i\chi''(\omega) \tag{2.14}$$

The real part χ' describes dispersion, while the imaginary part χ'' corresponds to absorption. These components are related through a Hilbert transform:

$$\chi'(\omega) = \frac{1}{\pi}\,\text{p.v.}\int_{-\infty}^{\infty}\frac{\chi''(\omega')}{\omega'-\omega}\,d\omega' \tag{2.15}$$

$$\chi''(\omega) = -\frac{1}{\pi}\,\text{p.v.}\int_{-\infty}^{\infty}\frac{\chi'(\omega')}{\omega'-\omega}\,d\omega' \tag{2.16}$$

The n and k are correlated to the $\hat{\chi}$ from the relations: $\hat{\chi} = \hat{\epsilon}_r - 1$ and $\hat{\epsilon}_r = (n + ik)^2$.

2.5. Origin of the dielectric losses

In the 10–100 THz frequency range, dielectric losses are typically dominated by infrared absorption caused by the excitation of vibrational modes [5], [33]. These vibrational modes are directly linked to the composition and microstructure of the dielectric film [5].

At microwave frequencies (1–10 GHz) and under sub-Kelvin temperatures, dielectric losses are primarily caused by the absorption of energy by two-level systems (TLSs) [5], [34].

In the mm–submm frequency range (0.1–1 THz), a-Si:H shows higher losses compared to the microwave regime [35], [36]. According to Buijtendorp [5], a-SiC:H exhibits a transition in loss mechanisms within this frequency range. Losses between 270–455 GHz are explained by the absorption tail of vibrational modes from frequencies above 10 THz. Therefore, the suggestion is made that above approximately 200 GHz, losses are dominated by vibrational modes, while below 200 GHz and at cryogenic temperatures and low power the TLSs are the dominant loss mechanism.

Furthermore, [5] notes that strong vibrational modes in the 10–30 THz range are not only present in a-SiC:H, but are also reported in other deposited dielectrics such as a-Si:H [8], [37]. Additionally, the reported TLS loss tangent (tan δ_{TLS}) for a-Si:H at microwave frequencies at cryogenic temperatures and low electric field strengths (˜10^{-5}) [35], [36], [38], supports the authors idea that a similar transition in dominant loss mechanism from TLSs to vibrational modes also occurs in a-Si:H as frequency increases within the mm–submm range.

2.5.1. Origin of Two-Level Systems

According to Gao et al. [39], TLSs can couple to the electric field of the resonator through their electric dipole moment, thereby modifying the material's dielectric constant, giving a TLS contributing to it ϵ_{TLS}. The real part of ϵ_{TLS} causes a shift in the resonant frequency, while the imaginary part leads to increased microwave loss. Additionally, the TLSs can switch states randomly, resulting in time fluctuations in the dielectric constant. This, in turn, causes the resonator's resonant frequency to fluctuate over time, contributing to frequency noise [9].

According to Buijtendorp [5], although the microscopic origin of TLSs is not fully understood [40], their behavior is well described by the standard tunneling model (STM) [34]. Additionally, multiple correlations between TLSs and material properties have been reported in literature.

A correlation between TLS density and atomic silicon density in electron-beam evaporated a-Si has been reported [41]. Additionally, nanovoids have been identified as the structural defects responsible for reduced atomic density in this material [42], further suggesting that TLSs may be linked to voids in the deposited dielectric. Remarkably, another study on electron-beam evaporated a-Si [43] report that instead of dielectric losses, mechanical losses are correlated with atomic density. These mechanical losses, attributed to internal friction caused by TLSs and are associated with nanovoids. The study proposes that TLSs responsible for dielectric losses may be linked to the density of dangling bonds, ρ_{DB}, which are a natural source of electric dipole moments. While the connection to tunneling states remains unclear, they suggest that dangling bonds could influence nearby atomic arrangements, inducing fluctuating dipoles moments as atoms tunnel between energy minima.

It is argued that at microwave frequencies, where TLS loss dominates, hydrogen reduces the TLS density by passivating dangling bonds. Therefore, it remains unclear whether hydrogenated films are beneficial or detrimental for mm–submm losses [5].

2.6. The Taguchi Method

In this section, I will explain the working principle of the Taguchi Method. The step-by-step procedure is[44]–[46]:

- Define the quality characteristic to be optimized
- Define the control parameters and their levels
- Design the orthogonal array
- Conduct the experiments
- Construct Main Effect Plots to find optimal recipe
- Prediction of the optimal recipe
- Run a confirmatory test

Define the quality characteristic to be optimized: The first step in the Taguchi method is to define the quality characteristic that needs to be optimized. This characteristic is the variable that determines the product quality. For this work, these are the material properties of the a-Si:H film, described in Section 4.1.

Define the control parameters and their levels: The second step is to identify the control parameters that are believed to have a significant effect on the quality characteristic. These control parameters must be independent of one another; otherwise, the resulting array will not be orthogonal. The control parameters used in this thesis work are shown in Section 3.2.

Design the orthogonal array: The next step is to design the orthogonal array (OA). This requires defining the number of levels for each control parameter, along with their specific values. An OA is a table that spans the experimental space, where each row corresponds to an experiment. To maintain orthogonality, each column (i.e., each control parameter) contains each level an equal number of times. This ensures that all levels are tested uniformly across the full set of experiments. As a result, the influence of each control parameter can still be statistically determined, even when multiple parameters are varied simultaneously.

Although is it possible to study the interaction effects between the control parameters with an OA, most OAs are designed to only study the main effects of the control parameters. This is because studying interaction effects would require an substantial increase in the number of the experiments to conduct. In commonly used OAs the number of levels is equal for all parameters. However, OAs with a mixed number of level is also possible, this thesis work which such an OA, see Table 3.2.

The short notation of an orthogonal array is $L_N(L^P)$, where L_N is the name of the array, N the number of experiments in the array, L is the number of levels for each parameter and P is the number of parameters [47].

To show how an orthogonal array is constructed, one example is shown in Table 2.1. This OA corresponds to an experimental setup with 4 control parameters, each with 3 levels. The measured quality characteristic is listed in the results column for each repetition, along with the calculated signal-to-noise ratio (SNR). Parameter levels are coded as numbers: low (1), medium (2), and high (3). By using this OA, the experimenter only needs to perform 9 experiments instead of all possible $3^4 = 81$ combinations.

Conduct the experiments: Once the Taguchi array is defined, the next step is to conduct the experiments and record the results. It is recommended to perform as many repetitions per experiment as time and budget allow. From these repetitions, the signal-to-noise ratio (SNR) is calculated, as explained in the next step. The SNR provides a measure of how robust the process is against variability.

Construct Main Effect Plots to find optimal recipe: The Main Effects Plot (MEP) is the key visualization tool in the Taguchi method. It shows how each control parameter influences the output across its levels. By analyzing these trends, one can identify which level of each parameter contributes most effectively to the desired outcome. In the Taguchi approach, MEPs are typically generated using the SNR instead of the average of the results.

Experiment	P_1	P_2	P_3	P_4	Results	SNR
1	1	1	1	1	$R_{1,1}, .., R_{1,N}$	SNR_1
2	1	2	2	2	$R_{2,1}, .., R_{2,N}$	SNR_2
3	1	3	3	3	$R_{3,1}, .., R_{3,N}$	SNR_3
4	2	1	2	3	$R_{4,1}, .., R_{4,N}$	SNR_4
5	2	2	3	1	$R_{5,1}, .., R_{5,N}$	SNR_5
6	2	3	1	2	$R_{6,1}, .., R_{6,N}$	SNR_6
7	3	1	3	2	$R_{7,1}, .., R_{7,N}$	SNR_7
8	3	2	1	3	$R_{8,1}, .., R_{8,N}$	SNR_8
9	3	3	2	1	$R_{9,1}, .., R_{9,N}$	SNR_9

Table 2.1: The $L_9(3^4)$ orthogonal array as an example, adapted from [46]. It contains the parameter level, the results for each of the repetitions and the SNR.

Using the SNR offers several advantages [44]. First, it provides a method to select the optimal level based on the smallest variation around the target. Second, it enables objective comparison between different sets of experiments with respect to variability. Third, because the SNR uses a logarithmic transformation, nonlinear behavior in the system is linearized. This supports the assumption of linearity when predicting the performance of the optimal combination of control parameters, which we refer to as optimal recipe.

There are three standard SNR formulas, depending on the objective of the quality characteristic: larger-the-better, smaller-the-better, or target-is-best [44], [46]

$$SNR_{larger-is-better}(i) = -10\log_{10}\left[\frac{1}{N}\sum_{n=1}^{N}\frac{1}{R_{i,n}^2}\right] \tag{2.17}$$

$$SNR_{smaller-is-better}(i) = -10\log_{10}\left[\frac{1}{N}\sum_{n=1}^{N}R_{i,n}^2\right] \tag{2.18}$$

$$SNR_{target-is-best}(i) = -10\log_{10}\left[\frac{1}{N}\sum_{n=1}^{N}(R_{i,n}-T)^2\right] \tag{2.19}$$

where i is the experiment number, N is the number of repetitions of the same experiment (so n = 1,2,..., N), $R_{i,n}$ is the measured quality characteristic of the ith experiment at the nth repetition and T is the desired target value of the quality characteristic.

When multiple repetitions of the same experiment are performed, the SNR separates fluctuations caused by noise in the experimental setup from those caused by varying the control parameter levels. The same SNR formulas can also be applied when only one measurement per experiment is available. In that case, the SNR serves as a loss function that quantifies the deviation from the target value [48]. The logarithmic term in the equation amplifies differences near the target, effectively rewarding responses that are closer to the desired outcome. This use of the SNR as a loss function for single measurements has also been demonstrated in [49].

As the Main Effect Plots show how the SNR changes with different factor levels, the first step is to compute the average SNR for each level of each parameter. This can be done using the following formula [46]:

$$\text{SNR}_{f,l} = \frac{1}{Q}\sum_{q=1}^{Q}\text{SNR}_{f,l} \tag{2.20}$$

where f refers to the control parameter, l to the level, and Q is the number of times level l appears in the orthogonal array. These average values are used to construct the Main Effect Plots (MEPs), which show how the SNR varies across the different levels of each parameter.

An example of Main Effect Plots is shown in Figure 2.7, which is based on the orthogonal array in Table 2.1. For each control parameter, a plot is generated showing the average SNR at each level. In

this example, each point in the plots represents the average of three measurements. By observing the trends, we see that for parameter 4, the SNR increases with decreasing level. For parameter 3, the SNR is identical at levels 1 and 2, but increases at level 3.

In these MEPs, the level with the highest SNR corresponds to the quality characteristic closest to the desired target. Hence, to determine the optimal recipe, the parameter levels with the highest SNR should be selected. For this example, the optimal levels are: P_1 — level 2, P_2 — level 1, P_3 — level 3, and P_4 — level 1.

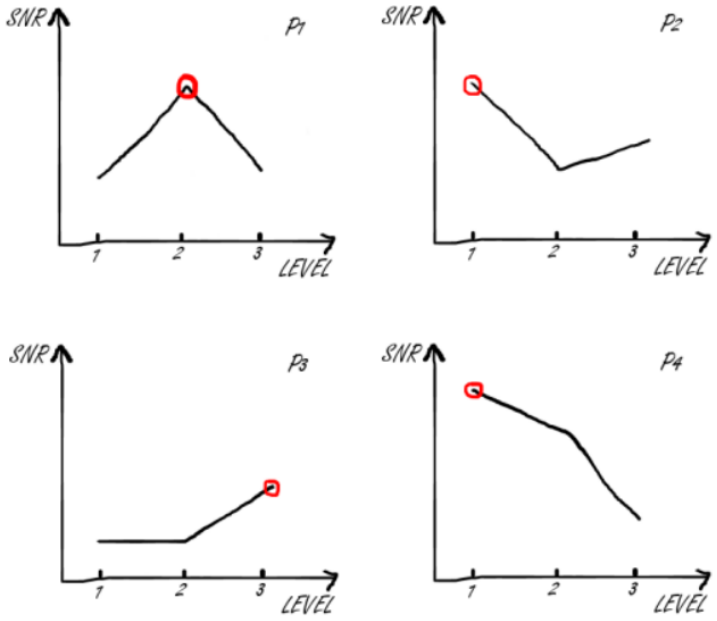

Figure 2.7: Example of main effect plots based on the orthogonal array shown in Table 2.1, adapted from [46].

Prediction of the optimal recipe: When the optimal recipe is chosen based on the Main Effect Plots, we can predict the SNR of the quality characteristic with the following formula [44], [46], [50]:

$$\mathrm{SNR}_{\mathrm{optimal}} = \overline{\mathrm{SNR}} + \sum_{f=1}^{F} \left[\frac{1}{Q} \sum_{q=1}^{Q} (\mathrm{SNR}_{f,l_{optimal}} - \overline{\mathrm{SNR}}) \right] \tag{2.21}$$

where $\overline{\mathrm{SNR}}$ is the average SNR of all experiments, $\mathrm{SNR}_{f,l_{optimal}}$ is the SNR for the experiments where the control parameter is at the optimal level.

With this $\mathrm{SNR}_{\mathrm{optimal}}$ you get an indication how significant the optimal recipe improves relative to the conducted experiments. However, SNR is not what we will directly measure when conducting an experiment. Therefore, we can calculate back the predicted 'raw measurement data' from the $\mathrm{SNR}_{\mathrm{optimal}}$, using the following formula [46]:

$$R_{\mathrm{optimal}} = 10^{\mathrm{SNR}_{\mathrm{optimal}}/20}. \tag{2.22}$$

This procedure of predicting the value at a certain recipe is general, so can be used to predict the outcome of every combination of levels.

Run a confirmatory test: The final step of the Taguchi method is to run the predicted optimal recipe. This step is important to verify whether the prediction based on the Taguchi analysis is accurate. The Main Effect Plots used to determine the optimal recipe only take into account the main effects of the control parameters, without considering possible interaction effects between the parameters. Therefore, testing the predicted recipe provides insight into how well the system can be described by main effects alone.

2.7. Analysis of Variance: ANOVA

To assess how strongly each control parameter influences the quality characteristic, it is common to implement an Analysis of Variance (ANOVA) within the Taguchi method, as explained in detail in [44]. ANOVA separates the total variation in the measured results across all experiments into contributions from each control parameter. For each parameter, the percentage contribution is calculated, indicating which parameters have the greatest influence on the outcome. This helps identify the most important parameters for optimization.

Additionally, ANOVA also provides statistical confidence by testing the significance of the observed effects. This is done using the F-value, which compares the variance caused by changing a specific parameter to the variance caused by random error. A higher F-value indicates a stronger and statistically significant effect on the response. The corresponding p-value is used to evaluate the significance level. A low p-value suggests that the observed effect is unlikely to be caused by random variation.

2.7.1. Regression model

To perform the ANOVA using a Python script, I have fitted the measured results using a regression model, following the approach described in [49]. In this model, all numeric control parameters are included as both linear and squared terms to capture potential curvature effects. The categorical parameter, Wafer Preparation, is included using dummy variables. Therefore, the regression model implemented in this thesis, has the following form:

$$R = \beta_0 + \sum_i \beta_{1,i} X_i + \sum_i \beta_{2,i} X_i^2 + \sum_j \gamma_j \cdot D_j + \varepsilon, \tag{2.23}$$

where R is the quality characteristic, X_i the numeric control parameters, X_i^2: the their squared terms (to capture curvature), D_j the dummy variables representing the categorical parameter, β and γ regression coefficients, and ε the residual error.

The model is fitted using the Ordinary Least Squares (OLS) method from the `statsmodels` python package. The resulting regression model serves as the basis for the ANOVA, where the total variation is divided into contributions from the linear terms, the curvature terms, the categorical parameter, and the residual error. The residual error captures the unexplained variation in the model and gives an indication of how well the selected variables account for the measured results. It is important to note that the regression model used in this thesis does not include interaction effects, as the orthogonal array used is designed for main effects only.

Contour plots:
Another application of the regression model is to predict the values of the quality characteristic for every possible combination of control parameter levels within the entire parameter space, instead of only at the discrete levels defined in the Taguchi design. This is possible because the regression model has quantified how the quality characteristic changes with respect to variations in the control parameters. Using this approach, contour plots can be generated that visualize how the predicted quality characteristic varies across the entire spanned parameter space.

However, it is important to note that the accuracy of these predictions depends on the variation in the measured film properties and how well the regression model is fitted to this variation. Predictions based on a model with a large residual error may be unreliable, as the unexplained variation could lead to deviations between the predicted and actual values.

2.8. Grey Relational Analysis

So far, the optimization methods have focused on experiments with only one quality characteristic. However, in this thesis the goal is to optimize the deposition recipe for multiple material properties. To convert this multi-objective optimization problem into a single-objective one, Grey Relational Analysis (GRA) is applied [48]–[51].

In Grey Relational Analysis, the measured results for each quality characteristic are first normalized between zero and one. From this normalized data, the Grey Relational Coefficient is computed, which

expresses how closely each measured value matches the desired target. The Grey Relational Grade (GRG) is then calculated by taking a weighted average of the Grey Relational Coefficients across all quality characteristics. In this way, multiple material properties can be evaluated simultaneously by optimizing the Grey Relational Grade. The optimal recipe has the highest Grey Relational Grade.

Step 1: Grey Relational Normalization
The first step is to normalize the measured results to values between zero and one, where the measurement closest to the desired value is assigned a one, and the measurement farthest from the desired value a value of zero. Depending on the optimization goal, there are three options for normalization: larger-the-better, smaller-the-better, and target-the-best. The corresponding formulas are [48]–[51]:

$$x_i(k) = \frac{y_i(k) - \min y_i(k)}{\max y_i(k) - \min y_i(k)} \tag{2.24}$$

$$x_i(k) = \frac{\max y_i(k) - y_i(k)}{\max y_i(k) - \min y_i(k)} \tag{2.25}$$

$$x_i(k) = 1 - \frac{|y_i(k) - T|}{\max\left(\max y_i(k) - T,\ T - \min y_i(k)\right)}, \tag{2.26}$$

where $x_i(k)$ is the normalized value for recipe i, $y_i(k)$ the quality characteristic for recipe i, $\min y_i(k)$ is the smallest value of $y_i(k)$ for the kth response , and $\max y_i(k)$ is the largest value of $y_i(k)$ for the kth response. For the target-the-best normalization, T represents the desired target value of the quality characteristic.

Step 2: Grey Relational Coefficient [48]–[51]:
The second step is to compute the Grey Relational Coefficients, which expresses the relationship between the desired and the actual normalized experimental results. The Grey Relational Coefficient $\xi_i(k)$ can be calculated as:

$$\xi_i(k) = \frac{\Delta_{\min} + \zeta\Delta_{\max}}{\Delta_{0i}(k) + \zeta\Delta_{\max}}, \quad 0 < \xi_i(k) \leq 1 \tag{2.27}$$

where $\Delta_{0i}(k) = |x_0(k) - x_i(k)|$ is the deviation sequence of reference sequence $x_0(k)$ and the comparability sequence $x_i(k)$. The terms $\Delta_{\min}$ and $\Delta_{\max}$ are the minimum and maximum values of all deviation sequences across all recipes and quality characteristics:

$$\Delta_{\min} = \min_{j\in i}\min_{k}\left\|x_0(k) - x_j(k)\right\|, \Delta_{\max} = \max_{j\in i}\max_{k}\left\|x_0(k) - x_j(k)\right\|. \tag{2.28}$$

The distinguishing coefficient ζ controls the resolution of the Grey Relational Coefficient and typically ranges between 0 and 1. In this work, ζ is set to 0.5, as commonly applied in literature [48], [49].

Step 3: Grey Relational Grade
The Grey Relational Grade shows how well each recipe performs when considering multiple quality characteristics, which in this work means multiple material properties. It is calculated by taking a weighted average over all quality characteristics of interest:

$$\gamma_i = \frac{\sum_{k=1}^{n} w_k, \xi_i(k)}{\sum_{k=1}^{n} w_k}, \tag{2.29}$$

where γ_i is the Grey Relational Grade for the ith recipe, $\xi_i(k)$ is the Grey Relational Coefficient for the kth quality characteristic, w_k is the weighting factor for that characteristic, and n is the number of characteristics being optimized. A higher Grey Relational Grade correspond to a recipe which is better to optimize all quality characteristics simultaneously.

Now that the Grey Relational Grade is calculated for each experiment, the same analysis tools from the Taguchi method can be applied to identify the optimal recipe. The Main Effect Plots can be constructed without using the SNR, as the relation between the desired value and the actual measurement is an intrinsic property of the Grey Relational Analysis. Similarly, the predicted optimal Grey Relational Grade can be calculated using the same approach as in Equation 2.21, by replacing the SNR with the Grey Relational Grade. With this prediction, the final step is to conduct the predicted recipe, to verify if the analysis has successfully find an improvement on the experiments.

3

Methodology: Film deposition

3.1. Investigation of the parameter space of the ICP-CVD

For the deposition of a-Si:H thin films in this project, I used the Oxford Instruments PlasmaPro 100 ICPCVD, whose operating principle is explained in Section 2.1. The goal of this project is to optimize the film properties by adjusting the deposition recipe of the ICP-CVD machine. To systematically investigate this, I first examined all possible parameters available in the PlasmaPro system. From this extensive list, I selected six parameters that are expected to have the most significant influence (as explained in the next section) on the deposition process: substrate table temperature, silane (SiH_4) flow rate, gas ratio between silane and argon, ICP power, table RF power, and chamber pressure.

In addition to these six process parameters, which will determine the conditions within the deposition chamber, I will add a substrate-related parameter: the method of oxide-layer removal prior to deposition. As previous studies have shown that TLSs affecting resonator performance mainly originate from oxide layers at interfaces [9], [20].

3.1.1. Relevance of the selected deposition parameters

Below I describe how each of the selected parameters affects the deposition process and material properties that effect the dielectric losses. The relevance of these material properties is further discussed in Section 4.1.

- **Table Temperature:** As shown in [5], [8], who varied the table temperature for three depositions using a similar PECVD technique, the table temperature strongly influences the structural properties of the films. Increasing the temperature resulted in films with lower hydrogen content, reduced void fraction, a smaller microstructure parameter, and a higher refractive index—an indicator of increased film density. Additionally, it is observed that for ICP-CVD processes, film density increases with deposition temperature [52].
- **Flow rate of Silane:** The authors of [20] varied the silane gas flow while testing many different recipes for a-Si:H, indicating its importance as a control parameter. An increase in silane flow rate is correlated with a decrease in the refractive index, and thus a reduction in the density of the deposited a-Si:H films [53].
- **Gas ratio between Silane and Argon:** This ratio is interesting because argon helps stabilize the plasma by enhancing ionization efficiency. It also affects the ion bombardment of the substrate, which influences material properties like residual stress.
- **ICP Power:** ICP power is the main parameter controlling the ion density of the plasma, as shown by [54]. The same paper also shows that ICP power influences the DC bias within the deposition chamber (if the Table RF power is non-zero). This bias controls the energy of ions bombarding the substrate, which affects material properties like film density and stress [54]. Another study also found a strong correlation between ICP power and the refractive index of the film [55].

- **Table RF Power:** Together with the ICP power, the table RF power controls the DC bias in the deposition chamber. This bias affects the ion flux and energy reaching the substrate [54], which in turn influences the intrinsic stress of the film due to changes in its microstructure..
- **Pressure:** The pressure inside the deposition chamber influences the stress in the a-Si:H film, as shown by [55], and is also linked to the refractive index of the deposited film [54].
- **Method for oxide-layer removal:** Previous studies have shown that TLS affecting resonator performance mainly originate from oxide layers at interfaces [9], [20]. Therefore, it is important to remove any native oxide before deposition. In literature mainly two methods are used for this removal; performing a short dip into diluted HF or argon milling. During a HF dip, the native oxide layer is etched away. Argon milling is done within the ICP-CVD chamber, where the top layer of the wafer gets etched away by bombarding it with argon ions. By alternating between these two surface preparation methods, I hope to assess their influence on the material properties.

3.2. Parameter levels

The seven parameters listed above are used to define the parameter space, which will determine the different ICP-CVD recipes executed during this project. Keeping in mind that I want to optimize the properties of the a-Si:H, I have selected the recipe reported to yield the lowest a-Si:H dielectric losses in literature [20] as the central point of this parameter space. It should be noted that [20] used a slightly different ICP-CVD system—the Oxford Plasmalab System 100 ICP 380—whereas the system used in this work is the Oxford PlasmaPro 100 ICPCVD. Therefore, I do not expect identical material properties when using their recipe directly. Nonetheless, I believe their process provides a well-motivated starting point for my study.

I decided to keep three levels for each of the six ICP-CVD parameters, as this allows me to identify whether there is an optimal value between the low and high levels. Wherever possible, the middle level corresponds to the recipe from [20]. This is the case for the table temperature (350°C), silane flow rate (30 sccm), and chamber pressure (10 mTorr). For the gas ratio, [20] used 100% silane, so I have chosen this as the maximum level for that parameter.

For the ICP power, I initially intended to use the 300 W value from [20] as the middle level. However, during preliminary testing—when I evaluated whether the ICP-CVD system could sustain stable plasma across all parameter combinations—I found that it failed to ignite plasma at powers below 300 W for certain conditions. Therefore, I selected 300 W as the lowest level for this parameter.

During the same testing, I found that a table RF power of 50 W produced a sufficiently high DC bias in the chamber. Concerned that increasing the table RF power beyond this level might lead to extreme ion energies, causing heavy bombardment and increased intrinsic stress, I set 50 W as the maximum level for this parameter.

The next step was to select specific values for the parameter levels. For the table temperature, I chose to test the upper end of the possible range, as [5] has indicated that higher table temperatures improve material properties. Therefore, I set the upper level just below the ICP-CVD system's limit, at 390°C instead of the 400°C maximum, to avoid potential overheating shutdowns.

For the gas ratio between silane and argon, literature shows considerable variation, ranging from 29% in [17] to 100% in [20] and [56]. I am interested to see how the presence of argon affects the deposition process, so I selected a broad range from 50% to 100%.

For the remaining parameters, I followed a similar approach. The difference between low and the high level are substantial, which is set on purpose. I expect that this wide range will be sufficient to reveal the influence of each parameter on the material properties. An overview of the chosen parameter values is given in Table 3.1.

3.3. Recipe optimization by Design of Experiments

In total, I want to optimize for seven parameters: six with three levels and one with two levels. Testing every possible combination would require $2 \times 3^6 = 1458$ experiments, which is clearly impractical. To address this, I applied a Design of Experiments (DoE) approach, which enables an enormous reduction

Numerical parameters:	Level		
	Low	Medium	High
Table Temperature	300°C	350°C	390°C
Gas ratio (SiH_4/SiH_4+Ar)	50%	75%	100%
Flow rate SiH_4	15 sccm	30 sccm	45 sccm
ICP power	300 W	500 W	700 W
Table RF	0 W	25 W	50 W
Pressure	5 mTorr	10 mTorr	15 mTorr

Categorical parameter:	Levels
Wafer Preparation	HF Dip / Argon Milling

Table 3.1: Parameters that define the parameter space, with values per level.

in the number of experiments while preserving the ability to analyze trends in the data effectively.

The DoE is a structured approach to plan, perform and analyze experiments. It allows the investigation of how multiple parameters influence a process by selecting a limited number of strategically chosen experiments, instead of testing all possible combinations. This reduces time and resource, while still given important information. DoE is particularly useful for complex systems with many variables, because it helps identify the most influential parameters, possible interactions, and optimal process conditions in an efficient way.

3.3.1. Comparison between DoE Techniques

Several methods exist within DoE, each based on a different strategy for planning experiments. In the following, I compare these methods to justify the selection of the most appropriate approach for this project.

Response Surface Methodology (RSM) is particularly useful for studying nonlinear interactions between parameters. It fits polynomial models to the experimental data, which can then be used to predict optimal parameter settings. RSM includes methods such as Central Composite Design (CCD) and Box-Behnken. CCD places experiments around a central point and includes additional "star points" to explore the edges of the design space. In contrast, Box-Behnken avoids extreme values and concentrates more experiments near the center of the design space [57]. I-optimal and D-optimal designs are also part of RSM and aim to further reduce the number of experiments by optimizing the experiment layout. I-optimal designs minimize prediction error and are better suited for identifying optimal operating conditions, whereas D-optimal designs reduce statistical uncertainty and are more useful for estimating the effects of control parameters on the measured material properties [57].

Another method used in DoE is the Fractional Factorial Design (FFD). It estimates the effect of control parameters by testing only a fraction of all possible combinations, based on the assumption that higher-order interactions are negligible. The fraction of the design space used is expressed as $\frac{1}{2^k}$, where k indicates the degree of reduction. FFD designs are categorized by their resolution, which indicates the level of aliases between effects. A higher resolution results in better separation between main effects and interactions. This makes FFD a very efficient method for reducing the number of experiments, at the trade-off of possible aliases especially in lower resolution designs [57].

The last method that was considered is the Taguchi method. It is based on an orthogonal array, which makes sure that each parameter is varied independently. This allows the effect of each factor to be evaluated individually. A key feature of the Taguchi method is the use of the Signal-to-Noise Ratio (SNR), instead of just the raw measurement data. The SNR is particularly useful for processes where results can vary significantly for the exact same parameters, as it quantifies the robustness of the process. This makes the method useful for improving process reliability. Another advantage is its straightforward approach for selecting the optimal parameter levels [44]. However, similar to FFD, the Taguchi method is less effective when strong interaction effects are present, since its orthogonal arrays are primarily designed to isolate main effects efficiently.

To make a choice between each of these methods, it is important to compare the number of experiments

required for each method. To do this, I used JMP software, which can generate experimental designs based on the different DoE methods. In JMP, only continuous parameters can be included in RSM designs, which all of the parameters are except for the wafer preparation method, which is named a categorical parameter. For the RSM method, using Central Composite Design (CCD) with six continuous parameters, the most efficient design required 46 experiments. The D-optimal and I-optimal methods could include all seven parameters and generated designs with 40 experiments each. The Fractional Factorial Design and the Taguchi method require only 16 and 18 experiments, respectively, but are limited to estimating main effects.

Based on the available information, I have selected the most suitable DoE method for this project. Both the Fractional Factorial Design (FFD) and the Taguchi method require a similar number of experiments. In principle, FFD has the advantage of estimating interaction effects between parameters. However, with only 16 experiments, the degree of reduction is so large that possibly the design can no longer estimate these interaction effects. Therefore, the more robust design of the Taguchi method is preferred over FFD.

When comparing the Taguchi method to the RSM methods, the number of experiments plays an important role. Although RSM methods offer advantages in modeling interaction effects and predicting optimal conditions across the full parameter space, I chose the Taguchi method for practical reasons. Running more than twice the number of experiments would be challenging within the limited time for the project, especially since each recipe must be deposited on two different wafers; one for ellipsometry and one for FTIR measurements (see Section 4 for more details).

Despite this trade-off, the Taguchi method still provided valuable insights. It allowed me to evaluate the individual effect of each parameter on the material properties, and to compare the relative importance of the parameters. Furthermore, I was able to predict the optimal parameter settings and the expected outcome at that setting. However, it is important to note that the Taguchi design does not capture interaction effects, which are therefore not studied in this work. The working principle of the Taguchi method is explained in detail in Section 2.6.

3.3.2. Orthogonal array used in this thesis

For the design of the orthogonal array, I have used the JMP software. Based on the seven control parameters, the software generated an orthogonal array consisting of 18 experiments, as shown in Table 3.2.

The orthogonality of the array is only preserved when all planned experiments can be successfully executed, which in this project means sustaining a stable plasma during deposition. Therefore, before performing any actual measurements, I tested each recipe to ensure plasma ignition and stability. After confirming that all 18 recipes resulted in stable plasma conditions, I verified that the orthogonal array was suitable for this project.

3.4. Procedure running deposition recipe

3.4.1. Number of depositions

The optimal wafer type differs for the Ellipsometer and the Fourier Transform Infrared Spectrometer (FTIR). For ellipsometry, a Single Side Polished (SSP) wafer with a thermal oxide layer is preferred, as it increases the reflected signal from the a-Si:H film. However, this wafer type is unsuitable for FTIR measurements, since the Transfer-Matrix Method (TMM) model used to analyze FTIR data does not support a thermal oxide layer. Instead, a Double Side Polished (DSP) wafer is required to maximize transmission. Consequently, each deposition recipe was performed twice, once on each wafer type. Additional details on the wafers used for ellipsometry and FTIR are provided in Sections 4.3 and 4.4, respectively.

In the Taguchi method, it is recommended to run each recipe multiple times if time allows. Repeating the same recipe helps distinguish the noise effects from the parameter effect, testing the robustness of the recipe. However, it is not necessary to repeat recipes to gain useful insights. Due to time limitations, and the need to deposit each recipe on two different wafers, I have measured each material property once for every experiment.

Rec. nr.	Table T (°C)	Flow rate SiH_4 (sccm)	ICP Power (W)	Table RF (W)	Pressure (mTorr)	Gas ratio $SiH_4/(SiH_4+Ar)$	Wafer Preparation
1	300	15	700	50	10	75	HF Dip
2	300	30	300	0	15	100	HF Dip
3	300	45	500	25	5	50	HF Dip
4	350	15	500	50	5	100	HF Dip
5	350	30	700	0	10	50	HF Dip
6	350	45	300	25	15	75	HF Dip
7	390	15	700	25	15	50	HF Dip
8	390	30	300	50	5	75	HF Dip
9	390	45	500	0	10	100	HF Dip
10	300	15	300	0	5	50	Argon Milling
11	300	30	500	25	10	75	Argon Milling
12	300	45	700	50	15	100	Argon Milling
13	350	15	300	25	10	100	Argon Milling
14	350	30	500	50	15	50	Argon Milling
15	350	45	700	0	5	75	Argon Milling
16	390	15	500	0	15	75	Argon Milling
17	390	30	700	25	5	100	Argon Milling
18	390	45	300	50	10	50	Argon Milling

Table 3.2: Orthogonal array used for the thesis, containing the levels of the factors for each recipe. Generated with the JMP software.

3.4.2. Wafer preparation

In this section I explain how I have applied the two methods of native oxide removal; HF dip and Argon milling.

HF dip

To perform the oxide removal, a HF Marangoni bath located at the Else Kooi Laboratory was used. A photo of this setup is included in the Appendix (Figure C.7). The system consist of of a bath filled with a 0.55% HF solution, an IPA vapor release system just above the liquid level and a wafer holder that holds 6 wafers simultaneously. The wafers are immersed into the solution of 4 minutes, followed by a 5-minute rinse with DI water. While the wafers are lifted, they are passed through the IPA vapor, which enabled Marangoni drying and passivates the wafers for 72 hours. Without this drying step, the passivation typically lasts only 20 minutes. I processed six wafers at a time, and made sure that the depositions were performed on the same day. For the details about the operation of the Marangoni Bath, see the flowchart at the end of this thesis.

Argon milling

The Argon milling technique was performed in-situ using the same ICP-CVD machine used for the depositions. Unlike the HF dip, Argon milling does not passivate the wafer surface, hence re-oxidation can occur if not performed immediately before the deposition. Argon milling works by inserting pure argon gas into the deposition chamber, which is then ionized by the RF power of the ICP coil. The generated plasma ions are accelerated toward the wafer due to the DC bias that is controlled by the

second RF source connected to the substrate electrode. The surface layer of the wafer is etched away by this ion bombardment.

At the beginning of the project, no argon milling recipe was available from the cleanroom staff. Using the argon milling recipe in [58] as a starting point, I developed a working recipe that could sustain a stable plasma. This recipe is shown in Table 3.3.

To determine the etch rate of thermal oxide, I performed ellipsometry measurements on a SSP wafer with a thermal oxide layer, see Section 5.1 for the etching uniformity over the wafer. A 3-minute etch removed approximately 5.0–5.5 nm of thermal oxide, as shown in Figure 5.1. Since the native oxide layer is typically 1–2 nm thick, I set 3 minutes as the standard etch time. The small overetch is to ensure complete removal of the native oxide. For all experiments containing Argon milling, this recipe was executed right before the deposition within the same run.

Parameter	Pump	Heat-up	Gas stab	Strike	Argon milling	Flush	Purge	Pump
Time	1m	2m	20s	10s	2m 50s	30s	30s	30s
Pressure	0 mTorr	10 mTorr	Unchanged	Unchanged	Unchanged	Unchanged	0 mTorr	Unchanged
Table RF	Off	Unchanged	Unchanged	50 W	Unchanged	Off	Unchanged	Unchanged
Table AMU	Off	Unchanged	C1: 42.0%, C2: 47.5%	Auto Park	Unchanged	Off	Unchanged	Unchanged
ICP RF	Off	Unchanged	Unchanged	300 W	Unchanged	Off	Unchanged	Unchanged
ICP AMU	Unchanged	Unchanged	C1: 47.0%, C2: 66.0%	Auto Park	Unchanged	Off	Unchanged	Unchanged
Ar (Gasring)	Off	Unchanged	Unchanged	Unchanged	Unchanged	25 sccm	Off	Unchanged
Ar	Off	20 sccm	Unchanged	Unchanged	Unchanged	50 sccm	Unchanged	Off
SiH_4 (Gasring)	Off	Off	Off	Off	Off	Off	Off	Off
Table Heater	300°C	Unchanged	Unchanged	Unchanged	Unchanged	Unchanged	Unchanged	Unchanged
Chamber Heater	60°C	Unchanged	Unchanged	Unchanged	Unchanged	Unchanged	Unchanged	Unchanged

Table 3.3: Argon milling recipe used to remove surface oxide in-situ with 300 W ICP and 50 W RF power. Auto Park setting enables automatic changing C1 & C2, to minimize reflected power. Chamber heater is set to avoid condensation.

3.4.3. Running deposition recipes

Before running the first deposition recipe of the day, I preconditioned the chamber using a dedicated precondition recipe. This step coats the chamber walls with a thin layer of a-Si:H, which improves consistency between depositions by stabilizing surface conditions inside the chamber.

Each deposition recipe consists of the same sequence of phases. As an example, the precondition recipe is shown in Table 3.4. During the first phase a high vacuum is created in the chamber. Next, the process gases are introduced into the chamber, which allows the wafer to match with the temperature of the table. In the following gas stabilization phase, the gas flowrates are adjusted to match the recipe values. Plasma ignition occurs during the strike phase by turning on the ICP power, which is executed with fixed settings for all recipes: 500 W ICP power, 10 mTorr pressure, and 0 W Table RF. These conditions are chosen to ensure reliable and stable plasma ignition. In the deposition phase that follows, all parameter levels are set to their recipe-specific value to deposit the a-Si:H film. The final three phases involve flushing the chamber with argon and pumping down to high vacuum.

As the deposition rates for the recipes were unknown beforehand, the suitable deposition time could not be computed. I aimed for a film thickness between 300 nm and 500 nm, which is ideal for ellipsometry measurements and the application thickness in parallel-plate capacitors [9]. Predicting the correct deposition time was an iterative process, making educated-guesses from the deposition rate observed from earlier runs. This resulted in a thickness range of 202 to 927 nm for the SSP wafers. For the DSP wafers, the deposition rate from the SSP runs could be used to set a more accurate deposition time, resulting in values closer to the target level of 500 nm.

Parameter	Pump	Heat-up	Gas stab	Strike	a-Si dep	Flush	Purge	Pump
Time	1m	1m	20s	10s	3m 50s	30s	30s	30s
Pressure	0 mTorr	30 mTorr	10 mTorr	10 mTorr	15 mTorr	Unchanged	0 mTorr	Unchanged
Table RF	Off	Unchanged	Unchanged	Unchanged	Unchanged	Unchanged	Unchanged	Unchanged
Table AMU	Off	Unchanged	Unchanged	Unchanged	Unchanged	Unchanged	Unchanged	Unchanged
ICP RF	Off	Unchanged	Unchanged	500 W	700 W	Unchanged	Unchanged	Unchanged
ICP AMU	Unchanged	Unchanged	C1: 48%, C2: 44%	Auto Park	Unchanged	Off	Unchanged	Unchanged
Ar (Gasring)	Off	Off	Off	Unchanged	Unchanged	25 sccm	Off	Unchanged
Ar	Off	Unchanged	Unchanged	Unchanged	Unchanged	50 sccm	Unchanged	Off
SiH_4 (Gasring)	Off	40 sccm	30 sccm	Unchanged	Unchanged	Unchanged	Unchanged	Off
Table Heater	300°C	Unchanged	Unchanged	Unchanged	Unchanged	Unchanged	Unchanged	Unchanged
Chamber Heater	60.0°C	Unchanged	Unchanged	Unchanged	Unchanged	Unchanged	Unchanged	Unchanged
GasRing Heater	60.0°C	Unchanged	Unchanged	Unchanged	Unchanged	Unchanged	Unchanged	Unchanged

Table 3.4: Deposition recipe parameters for the precondition step, used the cover the chamber wall with an initial thin a-Si:H layer. Each column represents a recipe phase with corresponding settings for pressure, gas flows, RF powers, initial AMU configuration and heater temperatures. The chamber heater and Gasring heater are both set to 60°C to prevent condensation.

4

Methodology: Characterizing a-Si:H thin film properties

4.1. Material properties of interest

This chapter explains which material properties I have measured and why these are relevant in the context of dielectric losses. Additionally, I will describe how each property was measured, including the tools used and the corresponding data analysis.

Directly measuring the cryogenic, mm-submm dielectric losses of the deposited films is beyond the scope of this project. However, as described in Section 2.5, literature proposes several correlations between dielectric losses and material properties. In the mm–submm frequency range (0.1–1 THz), two main loss mechanisms are identified: the absorption tail of vibrational modes originating from infrared absorption above 10 THz, and absorption due to two-level systems (TLSs). These TLSs have been linked to both nanovoids in the dielectric as well as the density of dangling bonds.

During this project, I was not able to directly measure the amount of nanovoids or the dangling bond density in the deposited films. However, based on literature research, I evaluated proposed correlations between these microscopic features and measurable material properties. By optimizing the material properties according to these correlations, it may be possible to predict which deposition recipe results in the lowest dielectric losses.

The material properties measured in this project are: thickness non-uniformity, void volume fraction (f_v), hydrogen content (C_H), microstructure parameter (R^*), optical refractive index (n), infrared refractive index (n_{ir}), band gap, and residual stress.

What makes these material properties interesting?

- **Thickness non-uniformity:** Uniform layer thickness is crucial in parallel-plate capacitors, particularly for large-area arrays such as those fabricated with TIFUUN. Thickness variations across the wafer can lead to significant frequency scatter between different PPCKIDs, since their resonance frequency is thickness-dependent [9].
- **Void-volume fraction (f_v):** A correlation between increasing TLS density and increasing void density in the dielectric has been proposed [41]. Therefore, measuring f_v serves as an indirect indicator of TLS-related dielectric loss.
- **Hydrogen content (C_H):** The C_H is directly calculated from the absorption dip around 640 cm^{-1} in the FTIR spectrum, which is a vibrational model of the SiH bond. A reduction in the strength of this dip is expected to reduce the corresponding infrared vibrational absorption tail extending into the mm-submm range [5]. On the other hand, hydrogen atoms are known to passivate dangling bonds, which are associated with TLSs [43]. Therefore, an increasing C_H could potentially reduce the TLS-related loss.

- **Microstructure parameter (R^*):** The R^* represents the ratio between SiH and SiH_2 bonds and reflects the microstructure of the film. This is an indication for the amount of voids in the film because SiH_2 bonds are occurring mostly on the surface of voids [33], [59], making R^* a useful indicator of void-related TLS density.
- **Optical refractive index (n):** The n is correlated with the defect density of a deposited a-Si:H film [60], where an increasing refractive index corresponds to a lower defect density. Therefore, n is related to other material properties like, f_v and R^* [5]. Measuring the n is suggested as an iterative optimization of the dielectric material properties, as is is relatively straightforward to measure [5].
- **Infrared refractive index (n_{ir}):** The n_{ir} refers to the refractive index measured using FTIR, at a region free of absorption modes (2800 cm^{-1}). Like the optical refractive index, the n_{ir} is correlated with the defect density of the film and therefore also linked to f_v and R^* [5].
- **Band gap:** The band gap of a-Si:H has been correlated with both refractive index and void fraction [53]. A lower band gap corresponds to a higher refractive index and lower void content, suggesting that the band gap is indirectly linked to dielectric loss.
- **Residual stress:** While not directly correlated with dielectric loss, the residual stress affects the mechanical stability of the film. High stress levels can lead to buckling or delamination, which is undesirable [23].

Residual stress was measured using a stressmeter. The hydrogen content, infrared refractive index, and microstructure parameter were obtained via Fourier Transform Infrared Spectroscopy (FTIR). The optical refractive index, band gap, void volume fraction, and thickness non-uniformity were measured using ellipsometry.

4.2. Residual stress

During this work, the FLX-2320-S stressmeter was used to determine the residual stress in the deposited films, by measuring the wafer curvature before and after deposition. A picture of the stressmeter, taken in the cleanroom, is shown in Appendix C. To perform a measurement, the wafer is placed at the center of the stage, resting on three support pins to minimize contact. A positioning ring with 24 notches is used to set the wafer's orientation, allowing scans at multiple angles. A laser scans along the diameter of the wafer, and a detector measures the deflection of the reflected beam. From this deflection, the system calculates the wafer bow. By comparing the bow before and after deposition, and using the film thickness measured by ellipsometry, the residual stress is computed using the Stoney equation 2.4), as explained in Section 2.2.

Stress measurements were performed along two orientations of the wafer, as depicted in Figure 4.1. The total stress of the recipe was set as the average value of these two measurement, as their difference was minimal.

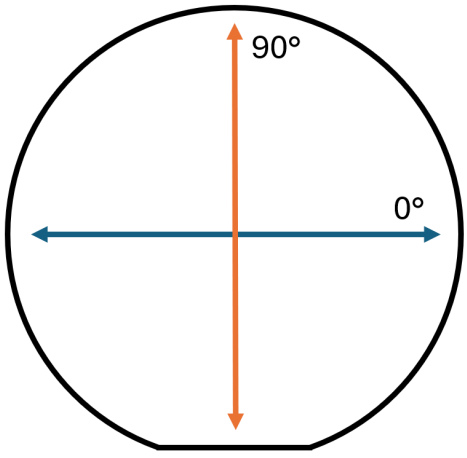

Figure 4.1: Stress measurement orientations.

4.3. Ellipsometry

For the ellipsometry measurements, I used the Woollam Spectroscopic Ellipsometer system, shown in Appendix C. This is a variable-angle spectroscopic ellipsometer (VASE) with a wavelength range of 210 to 1690 nm and a spectral resolution of 2 nm. The working principle of ellipsometry is explained in Section 2.3. Ellipsometry is used to measure both thickness and optical constants of stacked thin-film sample.

For the ellipsometry measurements, the a-Si:H films were deposited on 525 μm thick n-type (phosphor) single-side polished (SSP) c-Si wafers with a resistivity of ρ 1-20 kΩ cm and (100) orientation. To increase the reflected signal through the a-Si:H layer, a thermal oxide layer of ~123 nm was grown on the wafers prior to deposition.

I performed measurements with angles close to the Brewster angle of a-Si:H (~74°), as it maximizes the sensitivity to changes in the optical properties of the sample [61]. Therefore, for each point of the wafer I have measured with 3 angles; 65°, 70° and 75°.

4.3.1. Building an optical model

The measured change in polarization was fitted to an optical model consisting of the c-Si substrate, thermal oxide layer, a-Si:H film, and native oxide layer. The data from all three measurement angles were fitted simultaneously using the CompleteEASE software developed by J.A. Woollam Co. [28].

Thermal oxide measurement

This software contains predefined models for the c-Si substrate, thermal oxide, and native oxide, where only the their layer thicknesses are used as fitting parameters. Since the number of fitting parameters should be minimized to increase accuracy, I measured the thickness of the thermal oxide layer prior to the a-Si:H deposition. This allowed me to fix its value in the model, thereby removing it as a free parameter. For each wafer, I measured the thermal oxide thickness at 29 points, see Figure 4.3, and used the average thickness in the optical model.

From Cauchy to Tauc-Lorentz

For the a-Si:H layer, as its composition is dependent on the deposition recipe, no suitable predefined layer is available. Therefore, I have constructed the optical model in multiple steps, as recommended in [28].

The first step is fitting only the transparent region of the spectrum, where absorption is negligible. In this region, a Cauchy dispersion model was used, as it provides a good approximation of the refractive index and layer thickness. See Section 2.3.1 for more details on the Cauchy model.

Next, the Cauchy layer was replaced with a B-spline model by fitting it to the Cauchy layer. The B-spline offers greater flexibility to describe both the real and imaginary parts of the refractive index across the full spectral range. At this stage, the spectral fitting range was extended to include the absorbing region, which cannot be accurately described using the Cauchy model. For more details on the B-spline approach, see Section 2.3.1.

Finally, the B-spline was replaced with a Tauc-Lorentz oscillator model by fitting it to the B-spline. The Tauc-Lorentz provides a more physically meaningful description of the optical properties of amorphous materials such as a-Si:H. This model captures both the absorption near the band gap and the broader absorption at higher energies [30]. For details about the Tauc-Lorentz model, see Section 2.3.1.

This step-by-step procedure makes sure the fit is stable and physically meaningful, as the Tauc-Lorentz has five fitting parameters which are more likely to fit into a local minimum without making use of the Cauchy and B-Spline.

4.3.2. Fitting Tauc-Lorentz to obtain thickness, refractive index and band gap

Now that the optical model of the sample is complete, the Tauc-Lorentz model and the layer thicknesses of both the a-Si:H and native oxide are fitted to the measured ellipsometry data. As a final step to improve the Mean Squared Error (MSE) of the fit, two fitting parameters available in the CompleteEASE software are introduced: surface roughness and thickness non-uniformity. These parameters are commonly used to see if the fitting can slightly be improved.

The Tauc–Lorentz model, which is Kramers–Kronig consistent [30], allows the refractive index and absorption coefficient to be constructed over the fitted wavelength range using the Kramers–Kronig relations, as described in Section 2.4.2. To make an easy comparison between the optical refractive index of the different recipes, I have compared the refractive indexes at a fixed wavelength of 1200 nm, which follows the approach of Buijtendorp et al. [18]. Additionally, the band gap is extracted directly from the model, as it is one of the Tauc-Lorentz fitting parameters.

An example of the fitted optical model is shown in Figure 4.2. In the long-wavelength region (above ~600nm), the film is transparent and interference fringes are presents that are due to internal reflections. Towards shorter wavelengths, absorption becomes significant, which suppresses the interference features. In general, the number of visible fringes correlates with the film thickness. Due to the shape of the Tauc-Lorentz it describes both the absorbing and transparent region.

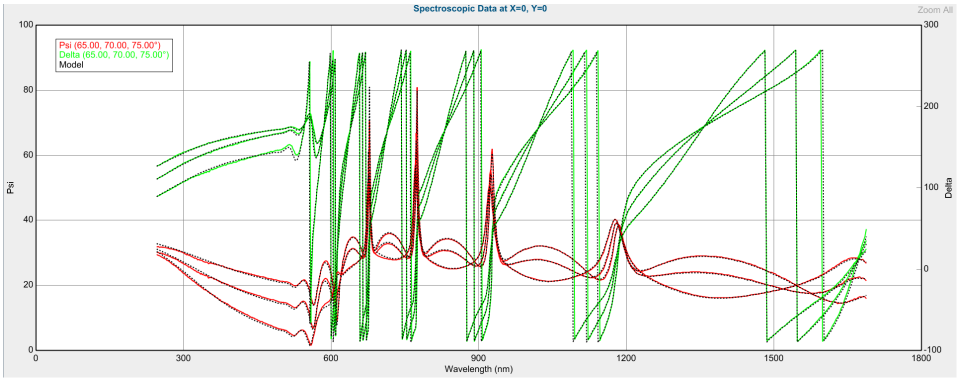

Figure 4.2: The optical model fitted to the data from SSP wafer 8 is shown as an example. The data contains measurements of Δ (green curve) and Ψ (red curve) at three different angles. The dashed black line represents the reconstructed data based on the model's calculation.

4.3.3. Thickness non-uniformity:

To measured the thickness non-uniformity of the deposited film, I measured 29 points distributed across each wafer, as shown in Figure 4.3. This distribution is chosen to effectively capture the radial non-uniformity. A 7mm border was chosen at the edge, as this area is not used to develop chips. Each of the 29 points was measured at three angles (65°, 70°, and 75°), resulting in a total of 87 measurements per wafer.

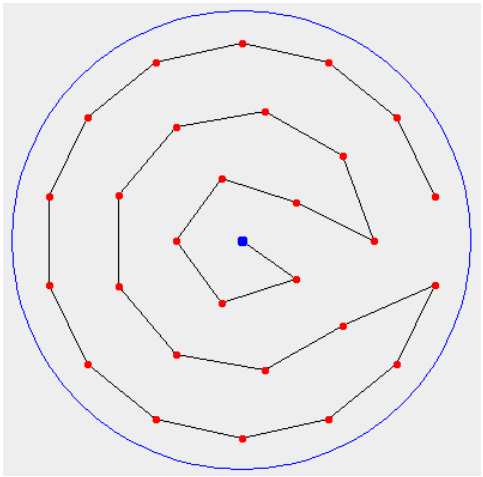

Figure 4.3: Ellipsometer measurement path showing 29 points distributed in a spiral pattern across the wafer. The blue dot marks the starting point. Each point is measured at three angles.

At each of the 29 measurement points, the a-Si:H thickness is computed, from which two types of non-uniformity plots were generated, shown in Appendix A. The first plot, similar to Figure 4.3, shows

the thickness distribution across the front-side of the wafer. The second, shown in Figure A.2, presents the thickness as a function of the radial distance from the wafer center. Since the measurement points are arranged in rings, this plot shows the average thickness for points at equal radial distances.

The measured thickness values were normalized to the radial average across all points, defined as the average of thickness values grouped by radial distance from the center. To express the thickness non-uniformity as a single number, I used the following definition:

$$\text{non-uniformity (\%)} = \frac{\text{Max} - \text{Min}}{\mu} \cdot 100\%, \tag{4.1}$$

where Max and Min are the highest and lowest average thickness values among the radial rings, respectively, and μ is the radial average thickness.

4.3.4. Void-volume fraction

To compute the void-volume fraction of the film, I used the optical model described in the previous section as the starting point. All fitting parameters were fixed at the values obtained from the Tauc-Lorentz fit. Next, I followed the procedure described by [8], in which the Tauc-Lorentz layer is replaced by a Bruggeman Effective Medium Approximation (BEMA) model. This model approximates the a-Si:H film as a composite material consisting of amorphous silicon and spherical voids, as explained in more detail in Section 2.3.2. The host material was set to the predefined 'a-Si parameterized' layer in CompleteEASE, which is described by a Cody-Lorentz oscillator and does not include an Urbach tail.

To minimize the risk of overfitting, the void fraction was the only free parameter in the BEMA model and was fitted, for wavelengths above 850 nm. To ensure the validity of this approach, only data from the wafer center were used. This choice was driven by the decision to keep all other parameters fixed, including the layer thickness. Due to the non-uniform thickness across the wafer, adding additional measurement points would have required fitting the thickness as well, something I avoided to maintain a single-parameter fit. As a result, the void-volume fraction f_v was determined from the center point of the wafer.

4.3.5. Thickness indication double-side polished sample

To obtain a first-order approximation of the a-Si:H film thickness—required for the FTIR data analysis described in the next section—measurements were also performed on double-side polished (DSP) wafers. These measurements were not intended to validate the SSP data, as the signal quality from DSP wafers is lower due to the absence of the thermal oxide layer, which enhances reflectance.

To obtain a first-order approximation of the aSiH film thickness, which is required for the FTIR data analysis described in the next section, we also measured double-side polished (DSP) wafers using the FTIR. The data from the DSP wafers was not used to validate the SSP measurements, as the signal quality is lower due to the absence of the thermal oxide layer, which increases the reflected signal. Additionally, the polished backside of the wafer causes reflections that interfere with the signal through a-Si:H, thereby reducing the measurement quality.

To model these DSP wafers in the CompleteEASE software, I started from the optical model fitted to the corresponding SSP wafer deposited with the same recipe. In this model, I removed the thermal oxide layer, and added a fitting parameter that accounts for the number of backside reflections caused by the polished backside. By using the SSP-based model, I expected the most accurate estimate of the thickness, this same procedure is applied in [62].

Additionally, as an extra independent estimation of the film thickness, scanning electron microscope (SEM) images of the cross sections of selected films were taken, which are presented in Appendix D.

4.4. Fourier Transform Infrared Spectroscopy

I used the Thermo Fisher Nicolet FTIR system to perform the transmission measurements of the a-Si:H samples in the wavenumber range 400–4000 cm^{-1}, with a spectral resolution of 4 cm^{-1}. A picture of the setup is shown in Appendix C. The working principle of the FTIR system is explained in Section 2.4.

For these measurements, the a-Si:H films were deposited on 500 μm thick p-type (boron) double-side

polished (DSP) c-Si wafers with a resistivity of $\rho > 1$ kΩ cm and (100) orientation. DSP high-resistivity wafers were selected to maximize the transmission through the substrate, thereby improving the signal quality. I have cleaved each wafer into quarter wafers to fit within the measurement slot of the instrument.

All deposited samples were measured as well as a reference sample, which was a bare DSP wafer. The measurement chamber was continuously purged with nitrogen for at least 15 minutes prior to and during the measurements to remove absorption due to water vapor.

To interpret the transmission data, I followed the procedure described in [5], by modeling the spectra using the Transfer-Matrix Method (TMM), which is explained in Section 2.4.1. The TMM model includes the deposited a-Si:H layer and the c-Si substrate, surrounded by air on both sides, as shown in Figure 2.6. From this model, the complex refractive index $\hat{n} = n + ik$ of the dielectric film was extracted, where the real part n is the refractive index and the imaginary part k is the extinction coefficient.

4.4.1. Fitting Transfer-Matrix Method to transmission data

Complex refractive index substrate: Baseline correction

To separate the signal of the a-Si:H film from that of the substrate, the complex refractive index $\hat{n}$ of the c-Si substrate was first determined using the measurement of the bare c-Si wafer. This analysis was performed using a Python script provided by the author of [5], which assumes a frequency-independent refractive index of $n = 3.42$ for c-Si [37].

A constant refractive index should result in a flat transmission baseline. However, as shown in Figure 4.4, the measured transmission of the bare substrate decreased with increasing wavenumber. This deviation could not be explained by the TMM model. Therefore, a baseline adjustment was applied by fitting a linear slope to the measured data within the range indicated by the vertical dashed lines. The resulting correction factor was then applied to all sample measurements containing a-Si:H. Additionally, for wavenumbers above 2800cm^{-1}, the measured data starts to deviate from the TMM model. The origin of this artifact is not clear, but fortunately the a-Si:H absorption dips of interest lie outside this region.

To compute the extinction coefficient k of the c-Si substrate as function of wavenumber, the TMM model was point-by-point fitted to the baseline-corrected spectra. For more details about the baseline correction procedure, I refer to [5].

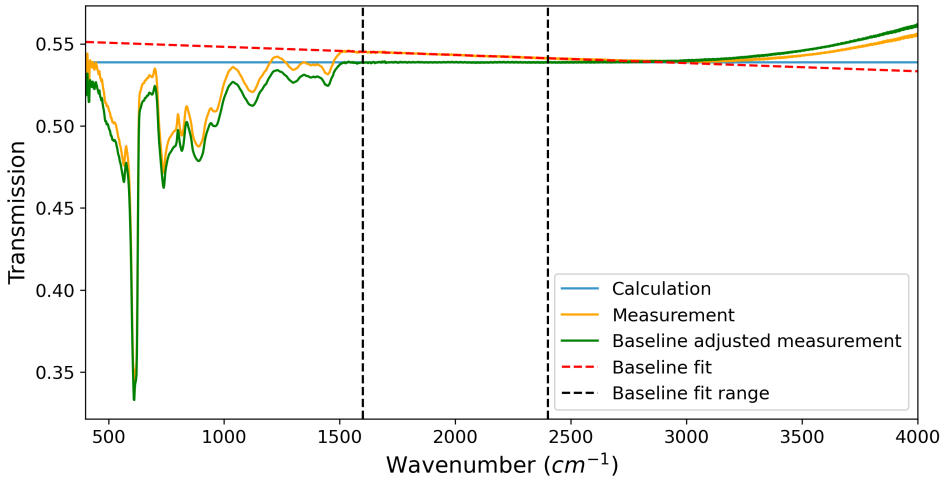

Figure 4.4: Baseline correction on c-Si transmission spectrum. It accounts for the optical effects not included in the TMM model (calculation). The transmission data was shifted by a linear slope fitted within the vertical dashed lines.

Kramers-Kronig consistent: Iterative fitting

Now that the $\hat{n}$ of the substrate is known, I modeled the data of the samples including the dielectric film. Therefore, it needs to be taken into account that the n and k of a material is correlated to each other. They are linked through the Kramers-Kronig relations, as explained in Section 2.4.2. These relations

describe that the refractive index is frequency-dependent, in contrast to the constant n assumed for the c-Si substrate. However, as argued by [5], this assumption is valid for c-Si, because its extinction coefficient is much smaller than that of a-Si:H.

The Kramers-Kronig consistency between the n and k was enforced using an iterative fitting approach, in which the thickness, n and k were fitted. The initial guess for the thickness was from the ellipsometry measurement described in Section 4.3.5. The first step was assuming a constant refractive index n_0, after which the extinction coefficient $k_0(\omega)$ was obtained through point-by-point fitting of a TMM model to the measured FTIR transmission. From $k_0(\omega)$, a frequency-dependent refractive index $n_1(\omega)$ was calculated using the Kramers-Kronig relations. A new fit was then performed to extract $k_1(\omega)$, and this process was repeated until convergence of both $n(\omega)$ and $k(\omega)$ was achieved.

Unfortunately, for some wafers the resulting model did not fit the data well. Figure 4.5 shows the fit for recipe 17, where a noticeable deviation between the data and the model occurs around 1700 cm^{-1}. This mismatch leads to a rising baseline in the extracted $k(\omega)$, as shown in Figure 4.6. This is problematic because the absorption features are expected to follow Gaussian-like profiles, and the artificial baseline interferes with accurate modeling. A possible explanation for the deviation is surface roughness of the deposited film; as demonstrated in [63], increased surface roughness reduces transmittance at higher wavenumbers. This behavior aligns with the deviation observed in Figure 4.5. However, since the main objective of this project was to analyze the dip height, investigating the origin of this deviation falls outside the project scope. Therefore, a spline-fit baseline correction was applied to the affected spectral region prior to modeling, as described in the next section.

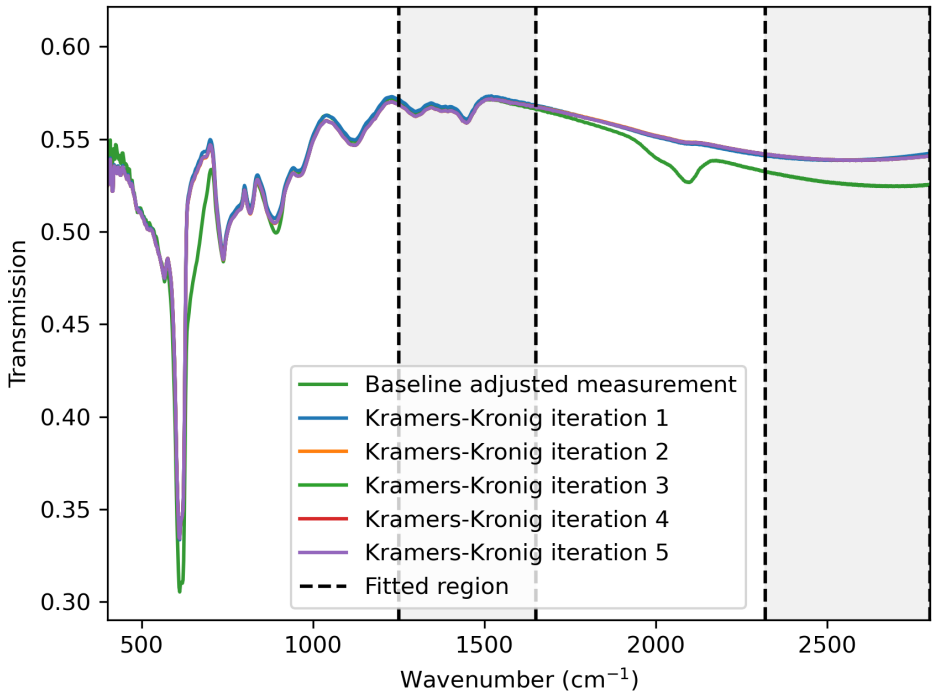

Figure 4.5: Enforcing Kramers-Kronig (KK) consistency between n and k by iterative fitting. The KK-consistent model deviates from the baseline-corrected data of recipe 17, for wavenumbers higher than 1700 cm^{-1}. This is problematic because this results in a plateau for the fitted $k(\omega)$, as shown in Figure 4.6

Spline correction: Remove deviation between data and TMM model

As mentioned in the previous section, for some samples the fit and the measured data did not overlap properly at higher wavenumbers. To correct this, a vertical translation of the baseline-corrected data was performed to match the TMM calculation. This corrected dataset was then used as the input for the Kramers-Kronig iterative fitting procedure described in the previous Section.

The first step was to fit the TMM model to the spectral region that does not exhibit baseline deviations or absorption features. For the sample deposited with recipe 17, this corresponded to the range

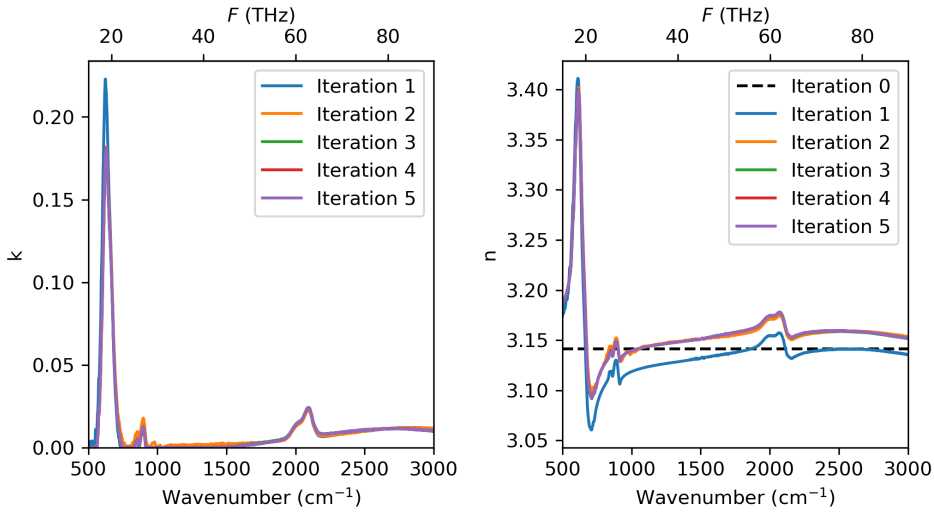

Figure 4.6: The Kramers-Kronig consistent $k(\omega)$ and $n(\omega)$ of recipe 17. The plateau the rises from 1700 cm^{-1} prevents an accurate gaussian fit of the absorption dip.

between 1000 and 1800 cm^{-1}, as shown in Figure 4.7. Within this range, both the film thickness and a frequency-independent refractive index n were fitted. The next step is to extract the baseline from the

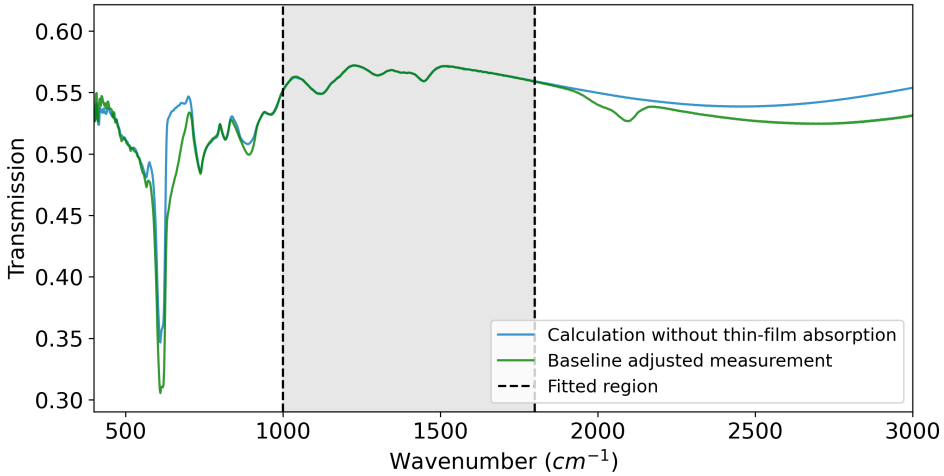

Figure 4.7: The TMM fitted to the transmission data of sample 17, where film thickness and frequency-independent n are fitted.

previously baseline-adjusted measurement. A spline was fitted to the data within the fitting ranges indicated by the dashed black lines in Figure 4.8. The difference between this spline baseline and the TMM model obtained in the previous step was then computed. This difference was added to the data to construct the 'Spline-corrected Data'. The correction was only applied for wavenumbers greater than the left boundary of the fitting region (1550 cm^{-1} for the example shown in Figure 4.8), since only in this region the transmission data deviated from the TMM model.

4.4.2. Infrared refractive index and absorption modes

When the Kramers-Kronig consistent TMM model is fitted to the 'Spline-corrected Data', the agreement between the model and the measurement is significantly improved, as shown in Figure 4.9. The corresponding extinction coefficient $k(\omega)$ and refractive index $n(\omega)$ are presented in Figure 4.10, where no rising plateau is observed in the $k(\omega)$ spectrum.

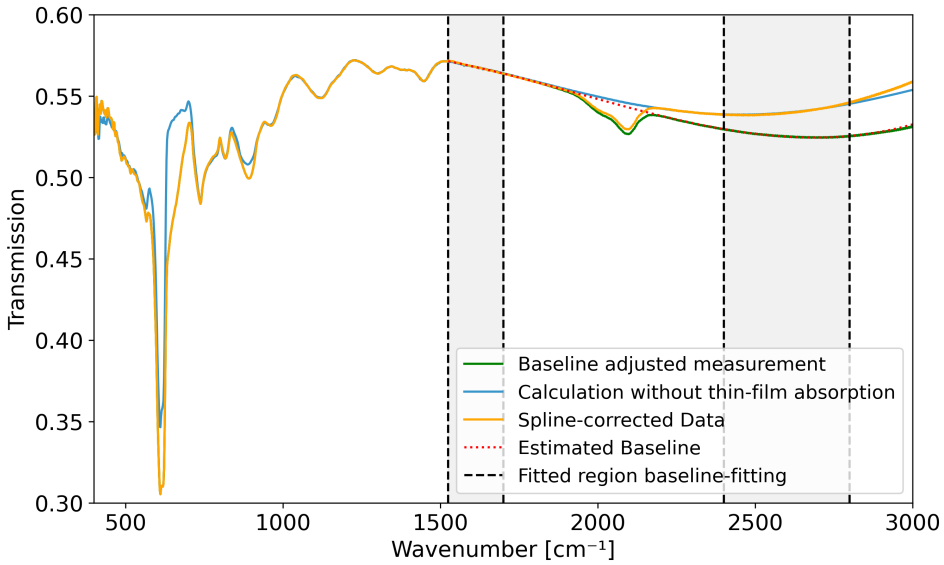

Figure 4.8: Baseline correction to let the baseline of the data of recipe 17 (green) match with that of the TMM calculation (blue). A spline is fitted that represents the baseline of the measurement, The baseline of the measurement is fitted with a spline and shifted to match the TMM calculation.

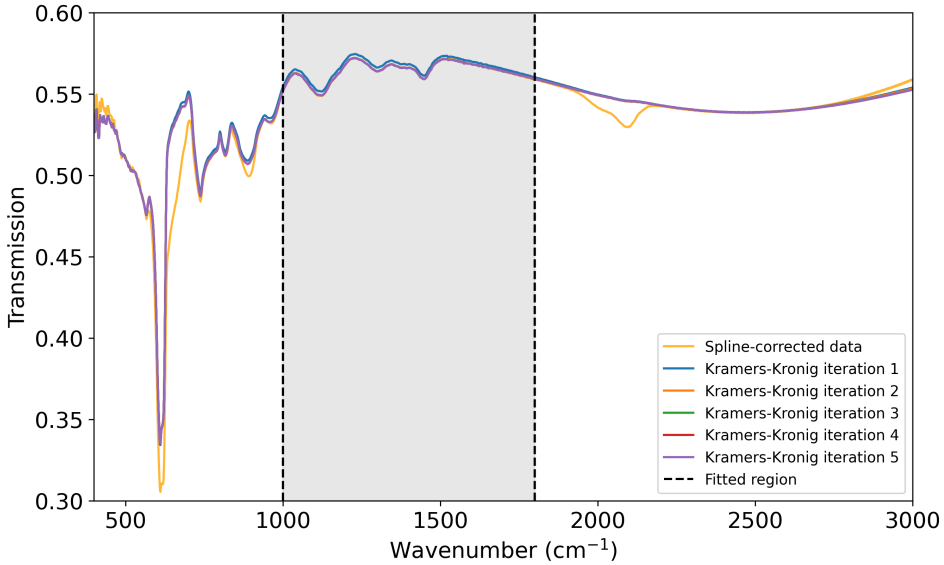

Figure 4.9: Enforcing Kramers-Kronig (KK) consistency between n and k, for the Spline-corrected data of recipe 17.

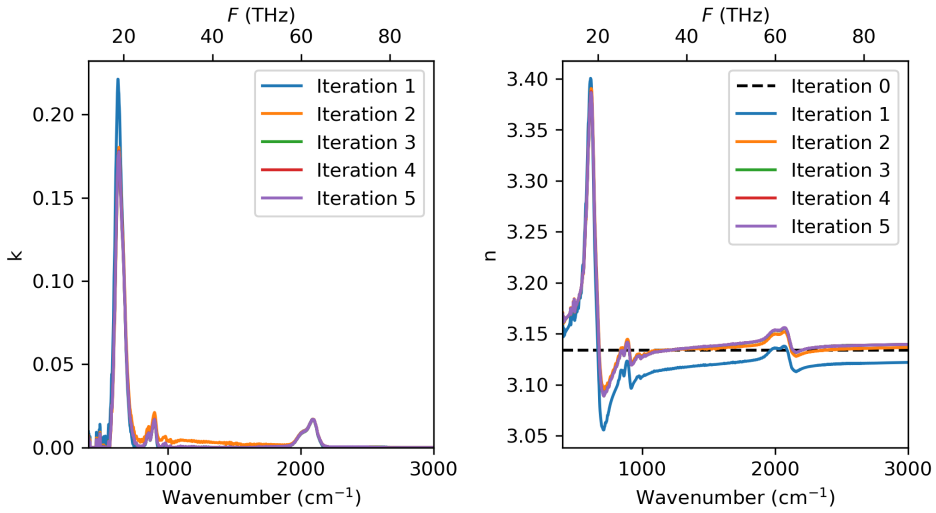

Figure 4.10: The Kramers-Kronig consistent $k(\omega)$ and $n(\omega)$ of recipe 17, for the Spline-corrected data.

Infrared refractive index

In Figure 4.10, the result of the iterative fitting procedure for $n(\omega)$ is shown. It can clearly be seen that the infrared refractive index is influenced by the extinction coefficient $k(\omega)$, as expected from the Kramers-Kronig relation. In order to compare the infrared refractive index between the different recipes, I have extracted the value of n at a fixed wavenumber of 2800 cm^{-1}. This wavenumber was chosen because the $n(\omega)$ spectrum is relatively flat in this region.

Absorption modes

From the $k(\omega)$ data shown in Figure 4.10, I have computed the absorption coefficient using $\alpha(\omega) = 4\pi k(\omega)/\lambda$, where λ is the wavelength. The resulting absorption spectrum is presented in Figure 4.11, together with Gaussian fits to the absorption features. The spectrum reveals several vibrational modes: a Si-H$_x$ wagging mode near 640 cm^{-1}[33], [37], [59], [64], two Si-H$_2$ bending modes around 850 and 890cm^{-1}[33], [37], [64], a Si-H stretching mode near 2000cm^{-1}[33], [37], [59], [64], and a Si-H$_2$ stretching mode around 2100cm^{-1} [33], [37], [59], [64]. From these absorption modes, the hydrogen content C_H and the microstructure parameter R^* can be computed. To do this, the integrated absorption I_x of each relevant mode is numerically calculated [5], [37]:

$$I_x = \int \frac{\alpha_x(\omega)}{\omega} d\omega, \tag{4.2}$$

where α is the absorption coefficient, ω is the wavenumber in cm^{-2} and x represents the center wavenumber of the Gaussian absorption peak.

4.4.3. Hydrogen content

Every hydrogen atom bonded to a silicon atom contributes to the wagging mode near 640 cm^{-1}[59]. Therefore, this vibrational mode can be used to compute the hydrogen content in a-Si:H films [33], [37], [59].

The hydrogen atom density N_H, can be computed by the relation; $N_H = A_{640} I_{640}$ [33], [37], [59], where I_{640} is the integrated absorption of the 640 cm^{-1} wagging mode and $A_{640} = 2.1 \cdot 10^{19}$ cm^{-3} is the proportionality constant [37].

To compute the hydrogen content in percentages we can rewrite the equation to the following [5]:

$$C_H = \frac{A_{640} I_{640}}{A_{640} I_{640} + N_{\text{Si}}} \cdot 100\%, \tag{4.3}$$

where N_{Si}, the atomic density of silicon, is $5 \cdot 10^{22}$ cm^{-3} [37].

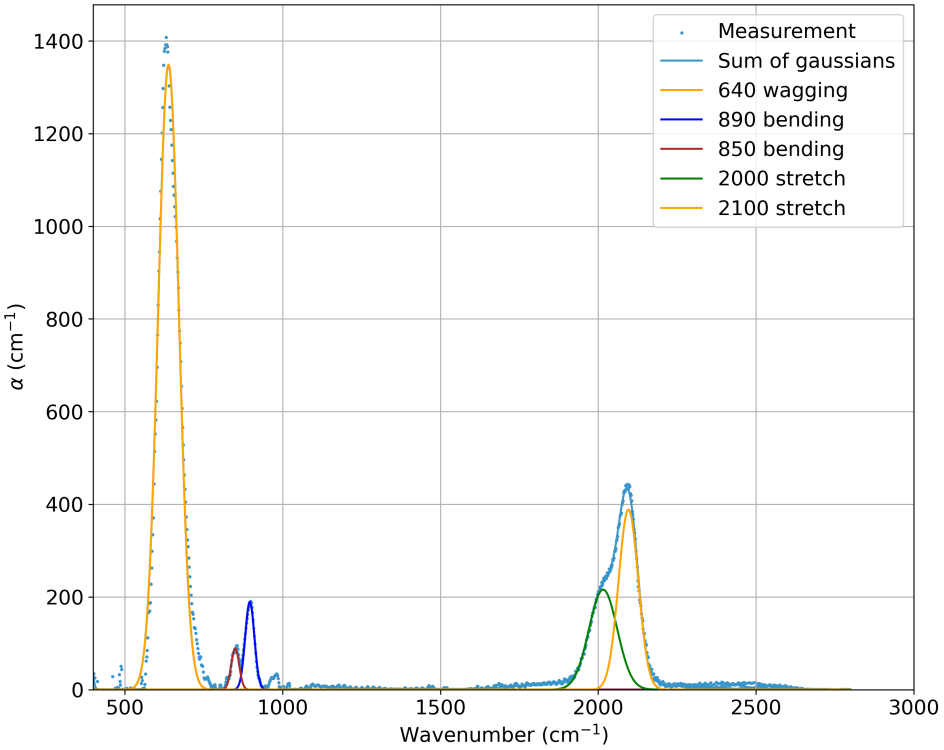

Figure 4.11: The absorption coefficient $\alpha(\omega)$ calculated from the $k(\omega)$-graph of Figure 4.10, together with the Gaussian fits of the absorption modes.

4.4.4. Microstructure parameter

The microstructure parameter R^* is defined as [33]:

$$R^* \equiv \frac{I_{2100}}{I_{2100} + I_{2000}}. \tag{4.4}$$

where I_{2000} and I_{2100} are the integrated absorptions of the 2000 and 2100 cm^{-1} stretching modes, respectively.

5

Results

This chapter presents the results of the Argon milling recipe developed during the project. It then discusses the identified relationships between the deposition parameters and the resulting material properties, supported by Main Effect Plots of the raw data as introduced in Section 2.6. The influence of each parameter is further quantified through ANOVA, described in Section 2.7. Optimal recipes for individual material properties are determined using S/N ratio-based Main Effect Plots. Subsequently, the results of the Grey Relational Analysis (GRA), outlined in Section 2.8, are presented to identify the recipe that simultaneously optimizes all material properties. The chapter concludes with the results of the verification experiment for the optimal recipes.

5.1. Non-uniformity of argon milling recipe

As described in Section 3.4.2, I established an ICP-CVD recipe during the project that performs argon milling on the wafer surface. Figure 5.1 shows the non-uniformity results of the argon milling process for two separate tests. These results were obtained by measuring the thickness of the thermal oxide layer using ellipsometry at 47 points, both before and after the milling step. In both tests, the etched thickness was approximately 5–5.5 nm, with a maximum variation within a wafer of less than 1 nm. Since the native oxide layer typically has a thickness of 1–2 nm, an etching duration of 3 minutes was chosen as the standard. This results in a slight overetch of 3–4 nm, ensuring complete removal of the native oxide.

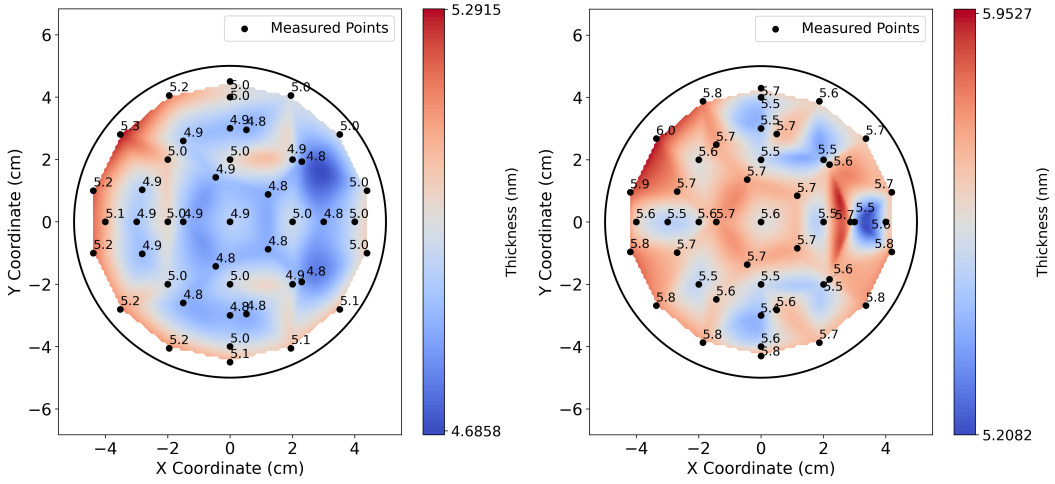

(a) First test of the non-uniformity of the argon milling recipe with a duration of 3 minutes. Maximum difference is 0.6 nm.

(b) Second test of the non-uniformity of the argon milling recipe with a duration of 3 minutes. Maximum difference is 0.75 nm.

Figure 5.1: Comparison of etch non-uniformity of argon milling recipe by running the same recipe twice.

5.1.1. Argon milling recipe recorded by ICP-CVD

Figure 5.2 shows the recorded process parameters during a test of the argon milling recipe with the ICP-CVD. Prior to plasma ignition at 200 seconds, the system stabilizes the chamber pressure and argon flow. At the moment of ignition, both the ICP RF and Table RF sources are turned on.

The reflected powers for both RF sources are minimized by the system's automatic matching unit (AMU), as visible in the sharp decrease after ignition. Simultaneously, a DC bias is established on the substrate, initially spiking when the reflected power of the Table RF is minimized, and then gradually decreases and stabilizes over time. Because the DC Bias induces an accelerating force on the argon ions, the incoming kinetic energies of the ions will have a similar shape.

This same DC bias behavior is consistently observed during every deposition recipe that includes a prior argon milling step. The recorded data of each argon milling phase show similar behavior across all runs, including the DC bias. This indicates that the recipe yields stable and repeatable chamber conditions.

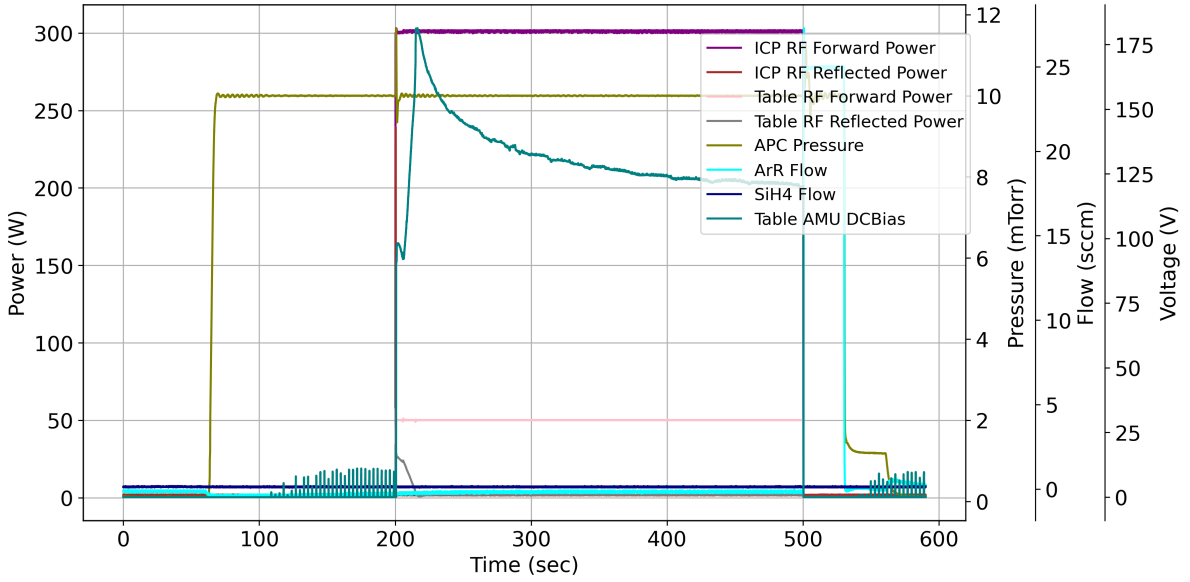

Figure 5.2: Chamber condition recorded during a 5-minute test of the argon milling recipe in the ICP-CVD system. Plasma ignition occurs at 200 seconds, after which the ICP RF and Table RF powers are applied. The corresponding reflected powers are shown, along with pressure, argon flow rate, and the resulting DC bias voltage on the substrate.

5.2. Establish relation between deposition conditions and material properties

In this section, I will discuss the observed relationships between the deposition parameters and the material properties. For each property, the Main Effect Plots (MEPs) of the raw data are presented to show the experimental trends. Next, the fitted regression model is introduced, which serves as the basis for the ANOVA analysis, which is explained in Section 2.7.1. From this model, the relative influence of each deposition parameter is quantified using the percentage contributions derived from the ANOVA. Finally, a comparison between the measured data and the predicted values from the regression model is presented. This comparison also includes recipes 19 and 20, which were conducted after the Grey Relational Analysis and are further discussed in Section 5.5.

5.2.1. Deposition rate

The deposition rate of the recipe is not a material property and therefore not a parameter which I have tried to optimize during the project. However, can tell very much about the conditions in the deposition chamber and therefore I have still investigated the influence of the deposition parameters onto the deposition rate.

The Main Effect Plots of the deposition rate, shown in Figure5.3, reveal several clear trends. Increasing

the SiH_4 flow rate lead to a significant rise in deposition rate, consistent with observations reported in [53]. A similar increasing trend is observed for ICP power, and the table RF power. In contrast, the deposition rate shows minimal dependence on substrate temperature and pressure, with only slight variations across their levels. The gas ratio exhibits a decreasing trend. Wafer preparation also has a effect, with Argon milling leading to higher deposition rates compared to HF dip.

Additionally, a regression model is fitted to the recipes, which is shown below:

$$\begin{aligned}\hat{y}_{\text{depo-rate}} = &-61.535 - 2.660 \cdot D_{\text{HF}} + 0.355 \cdot T - 0.001 \cdot T^2 + 0.866 \cdot F - 0.004 \cdot F^2 + 0.086 \cdot I \\ &- 0.000 \cdot I^2 + 0.157 \cdot R - 0.002 \cdot R^2 - 0.241 \cdot P + 0.003 \cdot P^2 - 0.350 \cdot G + 0.001 \cdot G^2\end{aligned}$$

where T is the table temperature (°C), F is the SiH_4 flow rate (sccm), I is the ICP power (W), R is the table RF power (W), P is the pressure (mTorr), and G is the gas ratio (%) The variable D_{HF} is a binary dummy variable that equals 1 if HF dip wafer preparation was used, and 0 if Argon milling was used.

From this regression model the ANOVA is performed, shown in Figure 5.4. It reveals that the ICP power is the most influential parameter overall, contributing a combined 29.0% (23.3% linear + 5.7% squared) to the total variance. This is followed by the SiH_4 flowrate, with a total contribution of 22.2%, and wafer preparation, which accounts for 15.9% as a categorical factor.

The table RF power also plays a noticeable role, contributing 9.7%, while the gas ratio contributes 5.4%. Table temperature has a smaller overall effect at 4.4%. In contrast, pressure contributes negligibly to the model, with a combined influence of just 0.2%.

The measured versus predicted deposition rates are shown in Figure 5.5. The regression model accurately captures the overall trends in deposition rate across the 18 Taguchi recipes, which corresponds with a modest residual error of 13.2%, indicating a good model fit. The measured deposition rate varied between 11.6 and 47.7 nm/min.

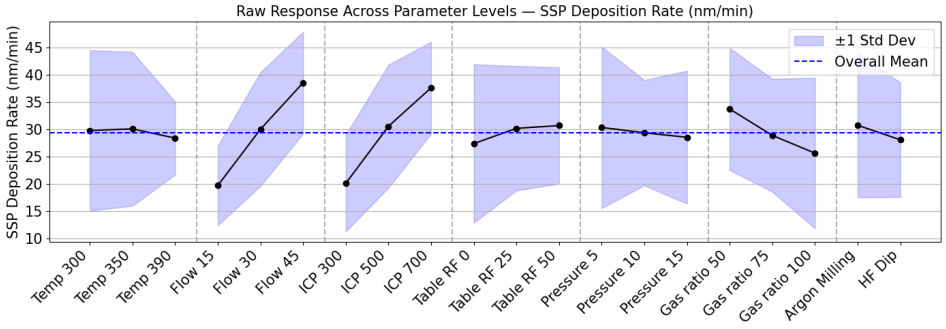

Figure 5.3: Main Effect Plots of the deposition rate across all levels of the seven deposition parameters. Each black point represents the average deposition rate measured at a given parameter level, while the blue-shaded region indicates the ±1 standard deviation range. The dashed horizontal line denotes the overall main deposition rate across all experiments.

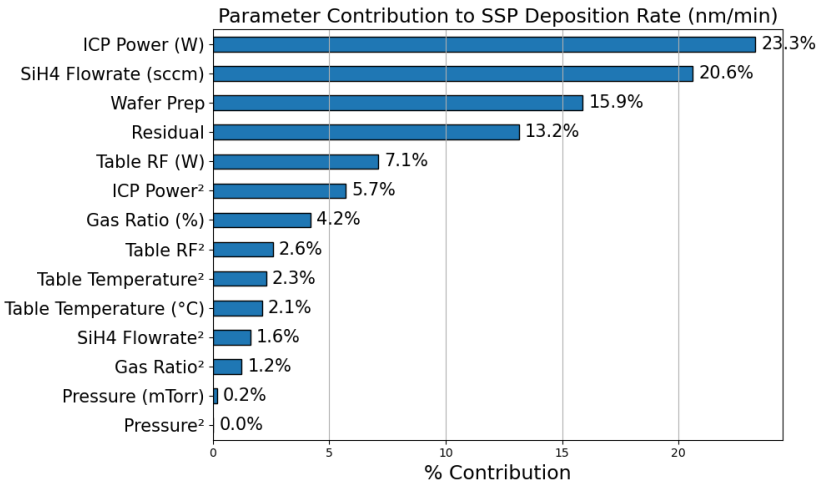

Figure 5.4: Percentage contribution of each deposition parameter to the deposition rate, based on the regression model. Each numerical factor is represented by a linear term and a squared term to account for potential non-linear effects. The bar lengths indicate the relative importance of each term in explaining the variance in the data.

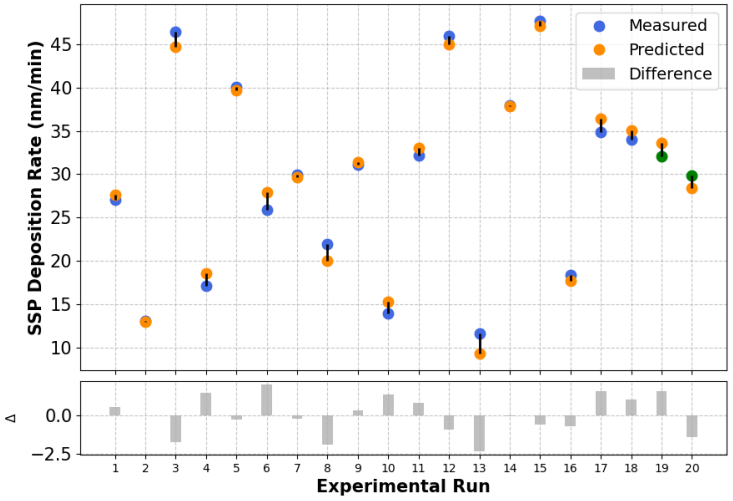

Figure 5.5: Comparison between measured and regression model–predicted deposition rate values across all experimental runs. The alignment indicates the model's ability to capture the variation in the data, while larger deviations correspond to higher residual variance as observed in the ANOVA. Recipes 19 and 20 were conducted after the Grey Relational Analysis (see Section 5.5).

5.2.2. Residual stress

In this section, I present the results of the residual stress measurements for both single-side polished (SSP) and double-side polished (DSP) wafers.

From the Main Effect Plots shown in Figure 5.6, it is clear that both SSP and DSP wafers exhibit very similar trends across all deposition parameters. This indicates that the substrate type (thermal oxide vs. bare silicon) has minimal influence on the stress in the deposited film.

Among all deposition parameters, the Table RF power has by far the strongest effect on the stress. A Table RF power of 0 W results in an average tensile stress of approximately 80 MPa, while activating the Table RF at 25 or 50 W induces a strong compressive stress, with the highest compressive value observed at 25 W.

This trend is consistent with the interpretation from [23], which suggests that intrinsic stress in a-Si:H arises from a balance between two competing mechanisms: tensile stress from the collapse of nanovoids during film growth, and compressive stress due to lattice expansion from ion implantation into previously deposited layers. A schematic of these two mechanisms is shown in Figure 2.2. With non-zero Table RF power, the increased ion momentum leads to a higher rate of ion implantation, resulting in a strong compressive stress in the film.

Furthermore, the standard deviation in stress values for the Table RF parameter is significantly smaller than for other parameters. The large difference in average stress values between RF levels, combined with this low standard deviation, indicates that Table RF is the dominant factor controlling film stress.

The regression models and the corresponding ANOVA results shown in Figure 5.7 support this conclusion, where the linear and squared terms of the Table RF contribute 97.4% and 97.9% to the observed stress variation for SSP and DSP wafers, respectively.

The fitted regression models for stress are given below:

$$\begin{aligned}\hat{y}_{\text{SSP-stress}} = &-537.363 + 25.175 \cdot D_{\text{HF}} + 2.648 \cdot T - 0.003 \cdot T^2 - 5.549 \cdot F + 0.101 \cdot F^2 + 1.201 \cdot I \\ &- 0.001 \cdot I^2 - 49.452 \cdot R + 0.724 \cdot R^2 + 25.566 \cdot P - 1.021 \cdot P^2 - 8.301 \cdot G + 0.051 \cdot G^2\end{aligned}$$

$$\begin{aligned}\hat{y}_{\text{DSP-stress}} = &\ 692.124 - 24.593 \cdot D_{\text{HF}} - 4.446 \cdot T + 0.007 \cdot T^2 + 8.124 \cdot F - 0.086 \cdot F^2 - 0.212 \cdot I \\ &+ 0.000 \cdot I^2 - 50.366 \cdot R + 0.714 \cdot R^2 + 12.852 \cdot P - 0.267 \cdot P^2 - 5.100 \cdot G + 0.031 \cdot G^2\end{aligned}$$

where T is the table temperature (°C), F is the SiH_4 flow rate (sccm), I is the ICP power (W), R is the table RF power (W), P is the pressure (mTorr), and G is the gas ratio (%) The variable D_{HF} is a binary dummy variable that equals 1 if HF dip wafer preparation was used, and 0 if Argon milling was used.

Although the orthogonal design allows us to inspect trends from the other parameters, their contribution to the total variation is below 1%. These trends should therefore be interpreted with caution, as they are susceptible to interaction effects or minor uncertainties in the Table RF power.

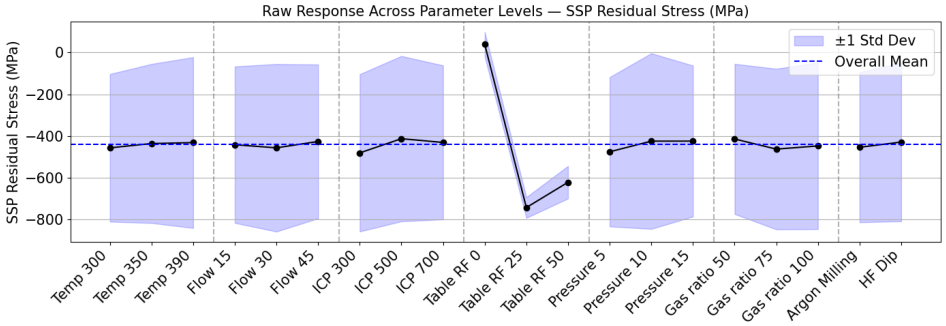

(a) SSP residual stress. Each black point represents the average residual stress at a given parameter level; the blue-shaded region shows the ±1 standard deviation. The dashed line denotes the overall main.

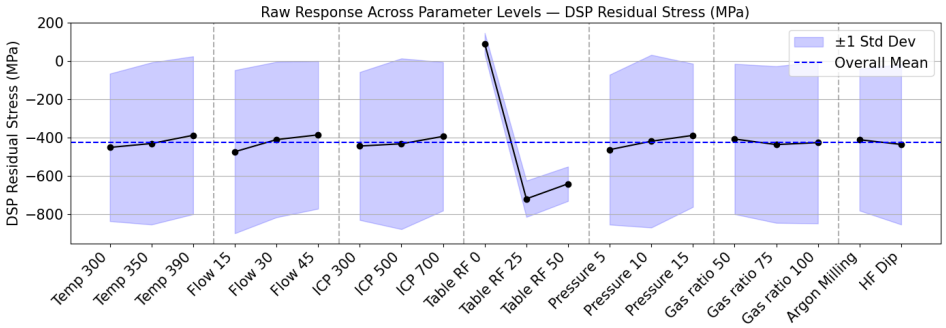

(b) DSP residual stress with same format as (a).

Figure 5.6: Main effect plots of the raw residual stress measurements for both SSP and DSP films across all levels of the seven deposition parameters.

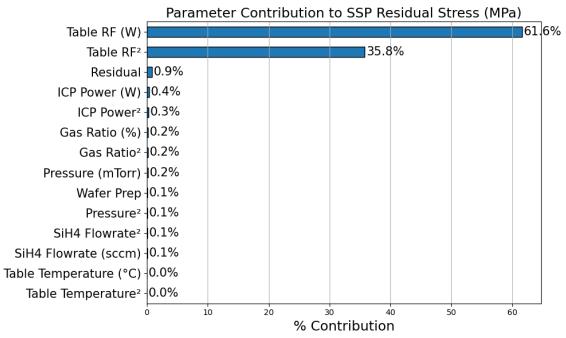

(a) SSP residual stress. Each bar represents the percentage contribution of a parameter (linear and squared terms) to the total variance, based on a regression model.

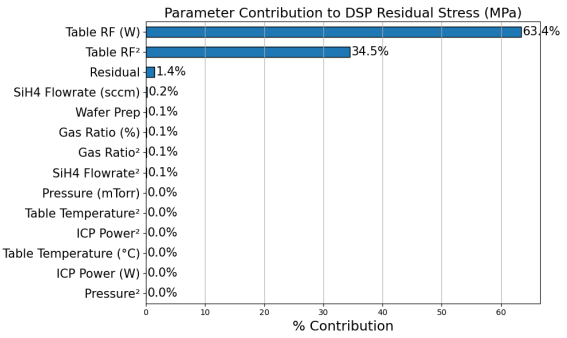

(b) DSP residual stress with same format as (a).

Figure 5.7: Percentage contribution of each deposition parameter to the SSP and DSP residual stress, as determined from regression analysis. Each numerical parameter includes a linear and squared term to capture non-linear effects.

For both SSP and DSP stress values, the contribution of the residual error is approximately 1%, indicating that the fitted regression model captures the variation in stress across all 18 recipes with high precision. This is also visible in Figure 5.8, where the measured stress values are compared to those predicted by the regression model for each corresponding recipe. The agreement between the measured and predicted values is strong.

Furthermore, the same distinct plateaus observed in the Main Effect Plot (MEP) of the Table RF parameter are clearly observed in the measured data points. While the high compressive stresses for non-zero table RF power can pose a risk to mechanical stability—particularly by increasing the likelihood of buckling—it remains well below the failure threshold of -1200 MPa reported by Johlin et al. [23]. As described in Section 2.7, the regression model was also used to generate the contour plots shown in Appendix B, which visualize the predicted residual stress across the entire parameter space for all combinations of parameter levels.

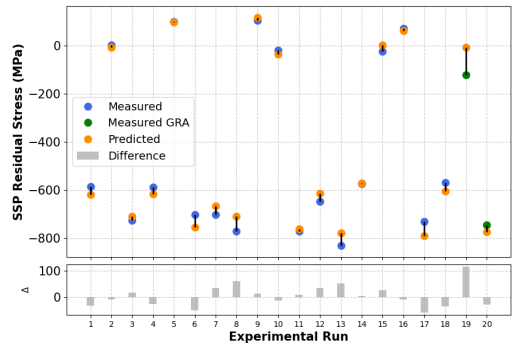

(a) SSP residual stress. The model closely follows the measured values, with only small deviations.

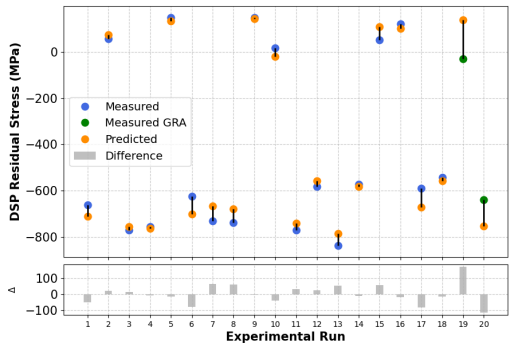

(b) DSP residual stress. Similar comparison between measured and predicted values, showing the accuracy of the fitted model.

Figure 5.8: Comparison between measured and regression model–predicted residual stress values for both SSP and DSP films. Recipes 19 and 20 were conducted after the Grey Relational Analysis (see Section 5.5).

5.2.3. Thickness non-uniformity

The Main Effect Plots of the thickness non-uniformity, as defined in Section 4.3.3, show that non-uniformity increases with increasing levels of SiH_4 flow rate and chamber pressure. In contrast, higher levels of table temperature, ICP power, Table RF power, and the gas ratio generally reduce the non-uniformity.

Additionally, a regression model is fitted to the recipes, which is shown below:

$$\hat{y}_{\text{non-uniform}} = 6.833 - 0.276 \cdot D_{\text{HF}} - 0.008 \cdot T + 0.000 \cdot T^2 + 0.068 \cdot F - 0.001 \cdot F^2 - 0.003 \cdot I + 0.000 \cdot I^2 - 0.075 \cdot R + 0.001 \cdot R^2 - 0.050 \cdot P + 0.011 \cdot P^2 + 0.037 \cdot G - 0.000 \cdot G^2$$

where T is the table temperature (°C), F is the SiH_4 flow rate (sccm), I is the ICP power (W), R is the table RF power (W), P is the pressure (mTorr), and G is the gas ratio (%) The variable D_{HF} is a binary dummy variable that equals 1 if HF dip wafer preparation was used, and 0 if Argon milling was used.

The ANOVA results, shown in Figure 5.10, indicate that Table RF power is the most dominant parameter, contributing 69.9% to the observed variation. While still the leading factor, its contribution is notably lower than its influence on residual stress, where it dominated with more than 97% contribution.

Other parameters contribute mildly to the variation in thickness non-uniformity, including Wafer Preparation (4.7%), SiH_4 flow rate (4.7%), and chamber pressure (4.1%). The residual contribution is 11.2%, indicating that the fitted deposition parameters can explain the variation in thickness non-uniformity across the experiments reasonably well. This is also observed in Figure 5.11, where the predicted values from the regression model align closely with the measured data across all 18 recipes. The measured thickness uniformity varied between 3.5% and 7.5% within a 4.3-cm radius. The corresponding contour plots are presented in Appendix B.

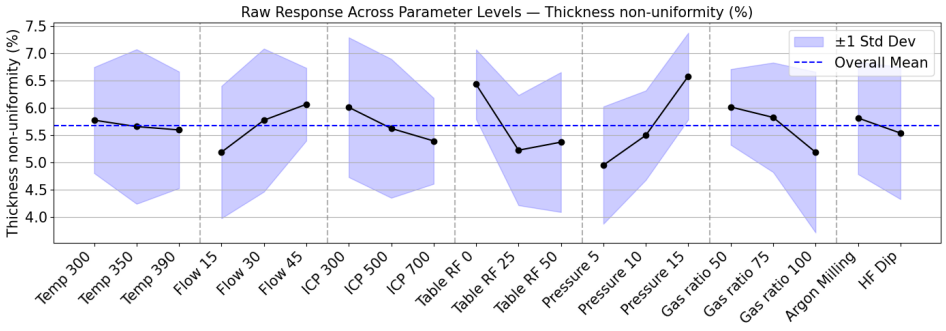

Figure 5.9: Main Effect Plots of the thickness non-uniformity measurement across all levels of the seven deposition parameters. Each black point represents the average thickness non-uniformity measured at a given parameter level, while the blue-shaded region indicates the ±1 standard deviation range. The dashed horizontal line denotes the overall mean thickness non-uniformity across all experiments.

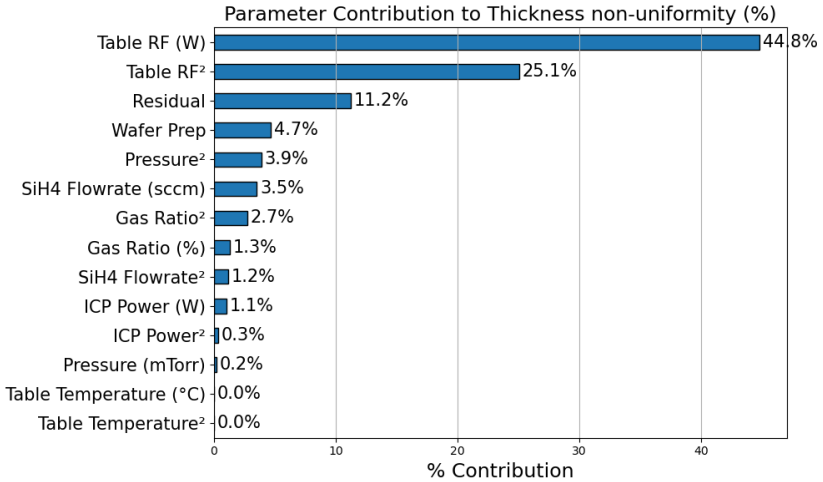

Figure 5.10: Percentage contribution of each deposition parameter to the thickness non-uniformity, based on a regression model. Each numerical factor is represented by a linear term and a squared term to account for potential non-linear effects. The bar lengths indicate the relative importance of each term in explaining the variance in the data.

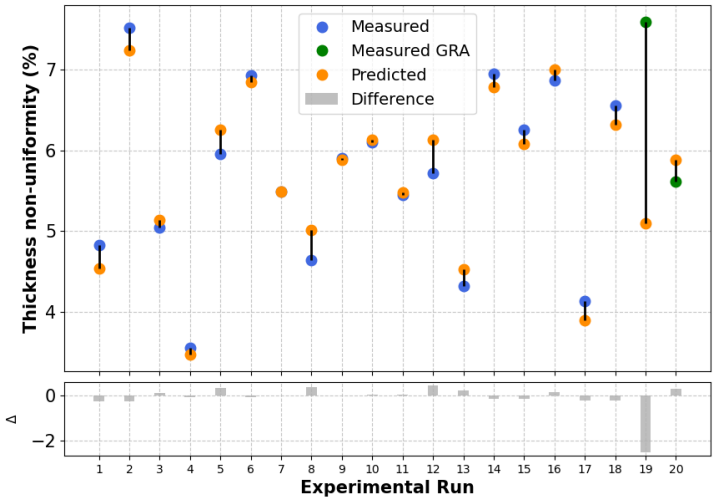

Figure 5.11: Comparison between measured and regression model–predicted thickness non-uniformity values across all experimental runs. The alignment indicates the model's ability to capture the variation in the data, while larger deviations correspond to higher residual variance as observed in the ANOVA. Recipes 19 and 20 were conducted after the Grey Relational Analysis (see Section 5.5).

5.2.4. Refractive index: Optical and infrared

In this Section, the results for both the optical and infrared refractive indexes are discussed. The optical refractive index was measured using the ellipsometer, while the infrared refractive index was obtained from FTIR measurements, as described in Sections 4.3 and 4.4, respectively.

The Main Effect Plots for both refractive indexes, shown in Figure 5.12, exhibit similar trends across all deposition parameters. This consistency between the two independently obtained datasets indicates agreement between the ellipsometry and FTIR measurements. This is expected, as both analyses rely on the same Transfer-Matrix Method, explained in Section 2.4.1.

For both refractive indexes, the trends for table temperature and pressure show a peak at the intermediate level. Wafer preparation using argon milling results in a higher refractive index compared to HF dip. For SiH_4 flow rate and table RF power, the refractive index increases with increasing parameter level. Conversely, for ICP Power and Gas Ratio, a decreasing trend is observed.

The observed peak at the intermediate table temperature agrees with the findings of [5], who report a monotonic increase for a table temperature between 100°C and 300°C. The increasing trend with SiH_4 flow rate contradicts [53], which reports a decrease.

Additionally, a regression model is fitted to the recipes, which is shown below:

$$\begin{aligned}\hat{y}_{\text{opt.}n} = {} & 0.567 - 0.020 \cdot D_{\text{HF}} + 0.017 \cdot T - 0.000 \cdot T^2 - 0.002 \cdot F + 0.000 \cdot F^2 - 0.001 \cdot I \\ & + 0.000 \cdot I^2 + 0.006 \cdot R - 0.000 \cdot R^2 + 0.022 \cdot P - 0.001 \cdot P^2 - 0.001 \cdot G + 0.000 \cdot G^2\end{aligned}$$

$$\begin{aligned}\hat{y}_{\text{inf.}n} = {} & 1.081 - 0.026 \cdot D_{\text{HF}} + 0.012 \cdot T - 0.000 \cdot T^2 - 0.005 \cdot F + 0.000 \cdot F^2 - 0.000 \cdot I \\ & + 0.000 \cdot I^2 + 0.003 \cdot R - 0.000 \cdot R^2 + 0.028 \cdot P - 0.001 \cdot P^2 + 0.004 \cdot G - 0.000 \cdot G^2\end{aligned}$$

where T is the table temperature (°C), F is the SiH_4 flow rate (sccm), I is the ICP power (W), R is the table RF power (W), P is the pressure (mTorr), and G is the gas ratio (%) The variable D_{HF} is a binary dummy variable that equals 1 if HF dip wafer preparation was used, and 0 if Argon milling was used.

The ANOVA results shown in Figure 5.13 indicate residual contributions of 42.8% and 48.0% for the optical and infrared refractive indexes, respectively. These relatively high residuals suggest that the variation in refractive index cannot be fully explained by individual parameter effects alone. This points

to the likely presence of interaction effects between deposition parameters. Among the main effects, Table RF Power is the most influential for the optical refractive index, while APC Pressure is most significant for the infrared refractive index. Table Temperature also contributes significantly to both measurements.

(a) Optical refractive index at (1200 nm), measured by ellipsometry. Black points show the mean per parameter level; the shaded region denotes ±1 standard deviation.

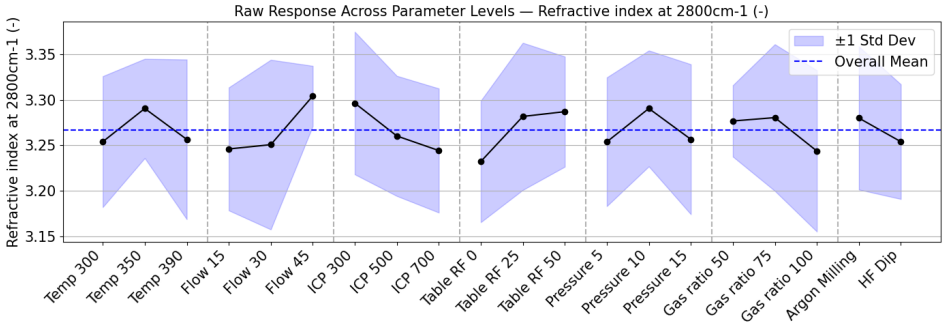

(b) Infrared refractive index at (2800 cm^{-1}), measured with FTIR. Same format as (a).

Figure 5.12: Main effect plots of refractive index at two frequencies across all levels of the seven deposition parameters.

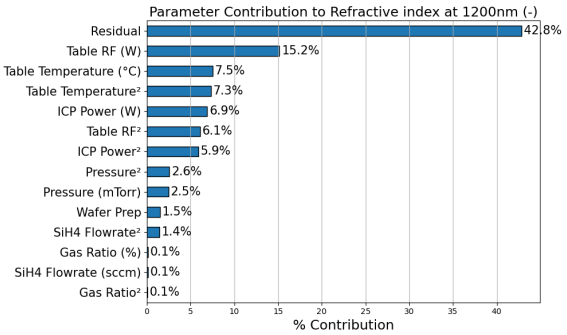

(a) Optical refractive index at (1200 nm), measured by ellipsometry. Each bar shows the contribution of a parameter (linear and squared) to the variance in a regression model.

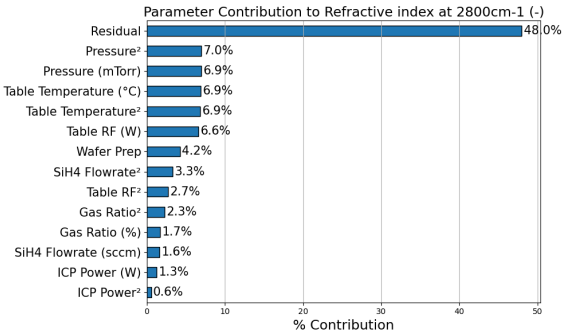

(b) Infrared refractive index at (2800 cm^{-1}), measured with FTIR. Same format as (a).

Figure 5.13: Percentage contribution of each deposition parameter to the optical and infrared refractive index, based on regression modeling. Non-linear effects are captured through squared terms.

The relatively high contribution of the residual indicates that the fitted parameters have limitations in explaining the observed variation. This is further supported by Figure 5.14, which shows significant deviations between the measured and predicted refractive index values. For the optical and infrared refractive indexes, the measured values ranged between 3.02–3.40 and 3.14–3.35, respectively. The corresponding contour plots, showing the predicted refractive index values across the full parameter space, are provided in Appendix B.

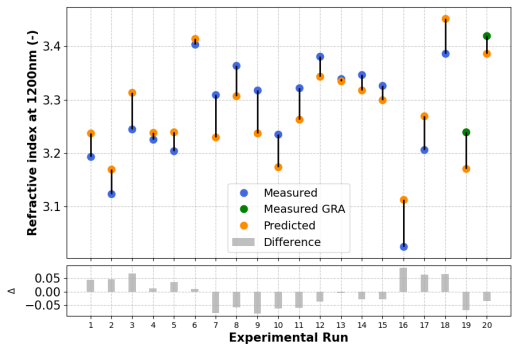

(a) Optical refractive index at (1200 nm), measured by ellipsometry. Deviations between the measured and predicted values reflect residual variance.

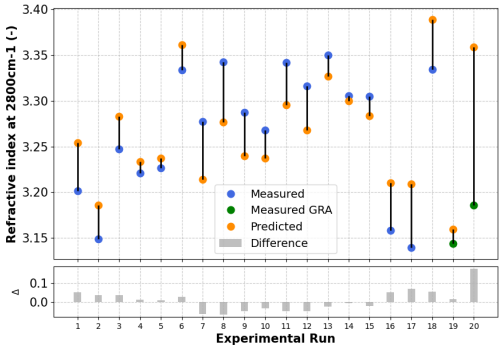

(b) Infrared refractive index at (2800 cm^{-1}), measured with FTIR. Same format as (a), illustrating model accuracy across experiments.

Figure 5.14: Comparison between measured and regression model–predicted refractive index values for optical and infrared frequencies. Recipes 19 and 20 were conducted after the Grey Relational Analysis (see Section 5.5).

5.2.5. Band gap

The Main Effect Plots of the band gap show a decreasing trend with increasing parameter levels for table temperature, silane flow rate, ICP power, Table RF power, and gas ratio, although the trends for the latter two are less pronounced. The parameter that stands out most clearly is Wafer Preparation, where performing an HF dip results in a significantly higher band gap.

The band gap was obtained from the fitted Tauc–Lorentz dispersion models to the ellipsometry data, where it is included as a fitting parameter. An observed decrease in band gap with increasing SiH_4 flow rate contrasts with the findings of Singh et al. [53], who reported an increasing trend.

Additionally, a regression model is fitted to the recipes, which is shown below:

$$\begin{aligned}\hat{y}_{\text{band gap}} = {} & 1.384 + 0.051 \cdot D_{\text{HF}} + 0.004 \cdot T - 0.000 \cdot T^2 - 0.008 \cdot F + 0.000 \cdot F^2 + 0.000 \cdot I \\ & - 0.000 \cdot I^2 - 0.001 \cdot R + 0.000 \cdot R^2 - 0.000 \cdot P + 0.000 \cdot P^2 - 0.001 \cdot G + 0.000 \cdot G^2\end{aligned}$$

where T is the table temperature (°C), F is the SiH_4 flow rate (sccm), I is the ICP power (W), R is the table RF power (W), P is the pressure (mTorr), and G is the gas ratio (%) The variable D_{HF} is a binary dummy variable that equals 1 if HF dip wafer preparation was used, and 0 if Argon milling was used.

Despite a dominant residual contribution of 44.6%, the ANOVA results support the importance of Wafer Preparation, which accounts for 26.8% of the total variation—making it the most significant main effect. The second largest contribution comes from the silane flow rate, at 15.2%.

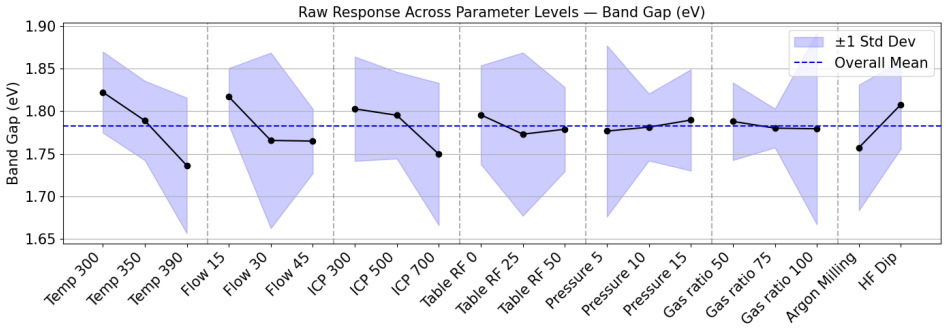

Figure 5.15: Main Effect Plots of the band gap measurement across all levels of the seven deposition parameters. Each black point represents the average band gap measured at a given parameter level, while the blue-shaded region indicates the ±1 standard deviation range. The dashed horizontal line denotes the overall mean band gap across all experiments.

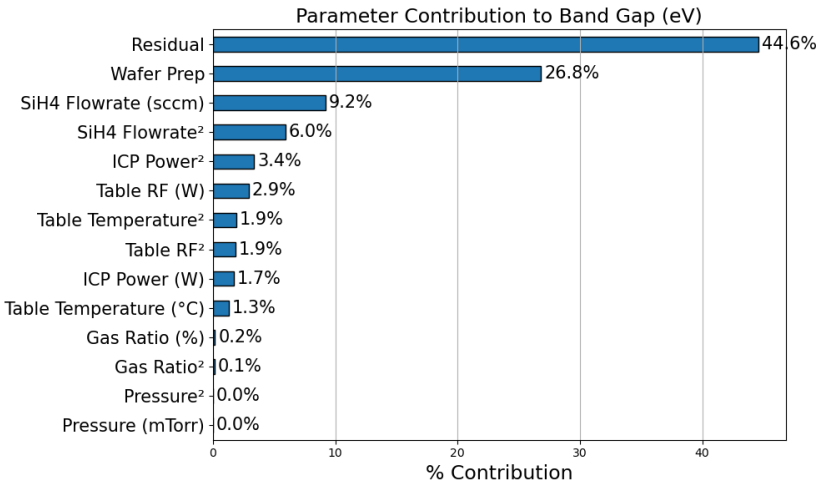

Figure 5.16: Percentage contribution of each deposition parameter to the band gap, based on a regression model. Each numerical factor is represented by a linear term and a squared term to account for potential non-linear effects. The bar lengths indicate the relative importance of each term in explaining the variance in the data.

The high residual contribution indicates limitations in the model's ability to fully explain the observed variation, which is also reflected in Figure 5.17, where notable deviations exist between the measured and predicted values. The band gap measurements ranged from 1.59 to 1.90 eV, with recipe 17 appearing as an outlier. The corresponding contour plots of the band gap are shown in Appendix B.

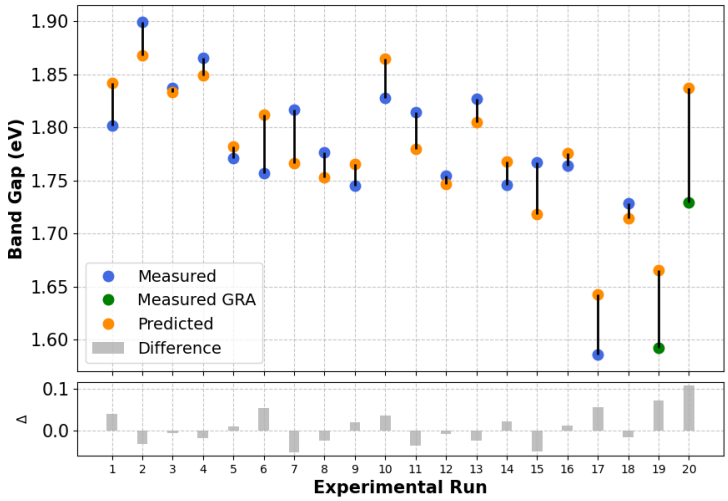

Figure 5.17: Comparison between measured and regression model–predicted band gap values across all experimental runs. The alignment indicates the model's ability to capture the variation in the data, while larger deviations correspond to higher residual variance as observed in the ANOVA. Recipes 19 and 20 were conducted after the Grey Relational Analysis (see Section 5.5).

5.2.6. Void-volume fraction

The Main Effect Plots of the void-volume fraction, shown in Figure5.18, indicate that increasing the table temperature, SiH_4 flow rate, and Table RF power results in a lower void-volume fraction, suggesting denser film growth under these conditions. In contrast, the void-volume fraction increases steadily with rising ICP power. Wafer preparation appears to have no significant effect. For pressure and gas ratio, a non-linear trend is observed, with the void fraction exhibiting a minimum and maximum at the middle level, respectively.

The decreasing void-volume fraction with increasing temperature is consistent with [5] and [52], which reports that higher deposition temperatures in low-pressure ICP-CVD increase film density.

Additionally, a regression model is fitted to the recipes, which is shown below:

$$\begin{aligned}\hat{y}_{f_v} &= 59.382 - 0.149 \cdot D_{\mathrm{HF}} - 0.248 \cdot T + 0.000 \cdot T^2 + 0.158 \cdot F - 0.006 \cdot F^2 + 0.016 \cdot I \\ &\quad - 0.000 \cdot I^2 - 0.159 \cdot R + 0.002 \cdot R^2 - 1.930 \cdot P + 0.093 \cdot P^2 + 0.196 \cdot G - 0.001 \cdot G^2\end{aligned}$$

where T is the table temperature (°C), F is the SiH_4 flow rate (sccm), I is the ICP power (W), R is the table RF power (W), P is the pressure (mTorr), and G is the gas ratio (%) The variable D_{HF} is a binary dummy variable that equals 1 if HF dip wafer preparation was used, and 0 if Argon milling was used.

The ANOVA contribution plot in Figure5.19 shows that a large portion of the variation remains unexplained, with a residual contribution of 60.5%, indicating substantial influence from unmodeled effects. Among the fitted parameters, pressure has the largest contribution (20.3%), followed by Table RF power (9.7%).

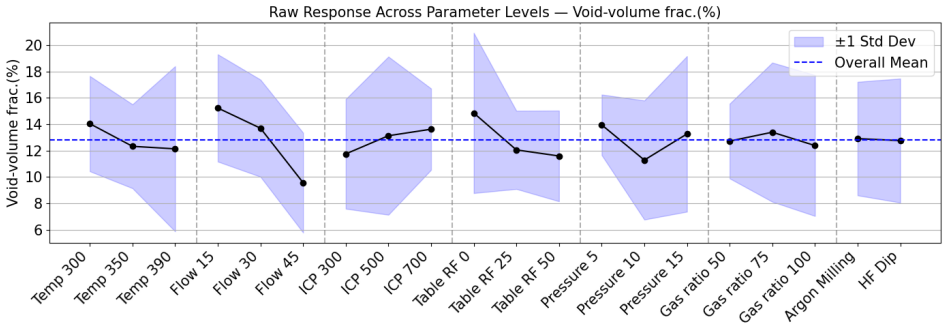

Figure 5.18: Main Effect Plots of the void-volume fraction measurement across all levels of the seven deposition parameters. Each black point represents the average void-volume fraction measured at a given parameter level, while the blue-shaded region indicates the ±1 standard deviation range. The dashed horizontal line denotes the overall mean void-volume fraction across all experiments.

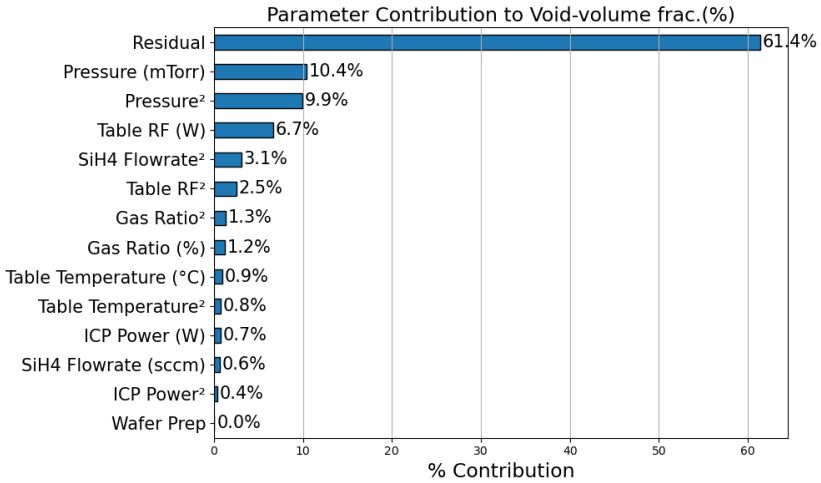

Figure 5.19: Percentage contribution of each deposition parameter to the void-volume fraction, based on a regression model. Each numerical factor is represented by a linear term and a squared term to account for potential non-linear effects. The bar lengths indicate the relative importance of each term in explaining the variance in the data.

That the regression model explains less than half of the observed variance is further supported by Figure 5.20, which shows significant deviations between the measured and predicted values. Across all experiments, the void-volume fraction ranged from 4.4% to 22.3%. Contour plots of the void-volume

fraction, presented in Appendix B, provide further insight but should be interpreted with caution due to the high residual.

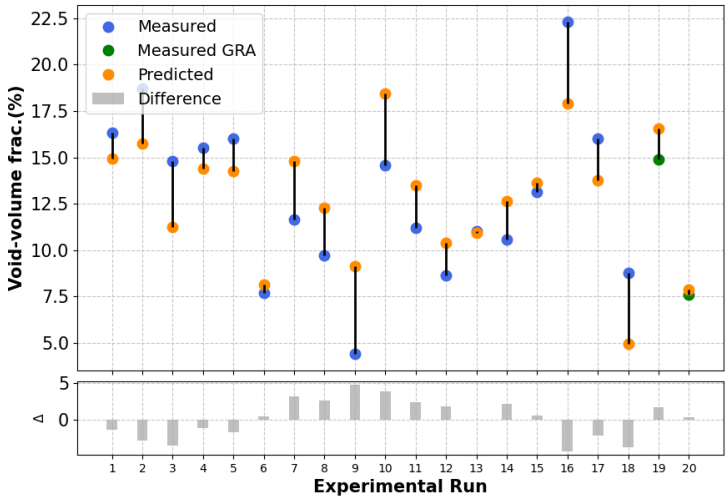

Figure 5.20: Comparison between measured and regression model–predicted void-volume fraction values across all experimental runs. The alignment indicates the model's ability to capture the variation in the data, while larger deviations correspond to higher residual variance as observed in the ANOVA. Recipes 19 and 20 were conducted after the Grey Relational Analysis (see Section 5.5).

5.2.7. Hydrogen content

The Main Effect Plots of the hydrogen content, shown in Figure 5.21, indicate that the hydrogen content decreases with increasing substrate temperature, ICP power, and gas ratio. Table RF power shows a sharp increase from the low to mid-level, after which it stabilizes. Minor increasing trends are observed for SiH_4 flow rate, chamber pressure, and wafer preparation (HF dip). The decreasing hydrogen content with increasing temperature is consistent with [5]

Additionally, a regression model is fitted to the recipes, which is shown below:

$$\begin{aligned}\hat{y}_{C_H} = &-4.969 + 1.017 \cdot D_{\mathrm{HF}} + 0.124 \cdot T - 0.000 \cdot T^2 - 0.264 \cdot F + 0.005 \cdot F^2 + 0.011 \cdot I \\ &- 0.000 \cdot I^2 + 0.238 \cdot R - 0.003 \cdot R^2 + 0.708 \cdot P - 0.025 \cdot P^2 + 0.012 \cdot G - 0.000 \cdot G^2\end{aligned}$$

where T is the table temperature (°C), F is the SiH_4 flow rate (sccm), I is the ICP power (W), R is the table RF power (W), P is the pressure (mTorr), and G is the gas ratio (%) The variable D_{HF} is a binary dummy variable that equals 1 if HF dip wafer preparation was used, and 0 if Argon milling was used.

The ANOVA contribution analysis confirms that Table RF power is the dominant factor, accounting for 47.3% of the explained variance. This aligns with the clear trend observed in the Main Effect Plot. The residual contribution is 31.7%, indicating a moderate level of unexplained variation, but suggesting that the regression model still captures the main influences reasonably well. Parameters with smaller contributions include flow rate (8.4%), pressure (4.4%), and wafer preparation (4.3%).

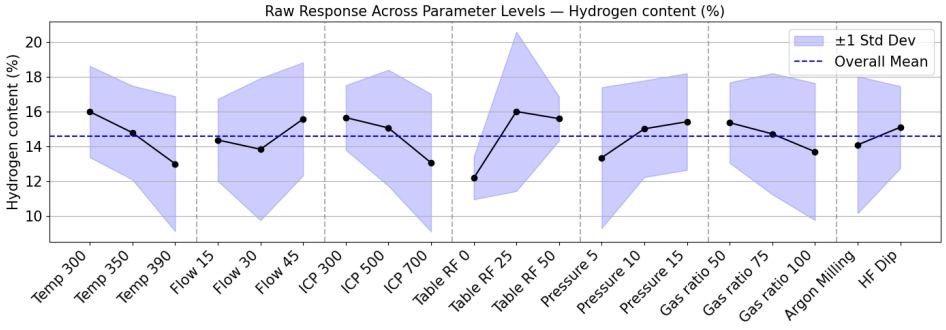

Figure 5.21: Main Effect Plots of the hydrogen content measurement across all levels of the seven deposition parameters. Each black point represents the average hydrogen content measured at a given parameter level, while the blue-shaded region indicates the ±1 standard deviation range. The dashed horizontal line denotes the overall mean hydrogen content across all experiments.

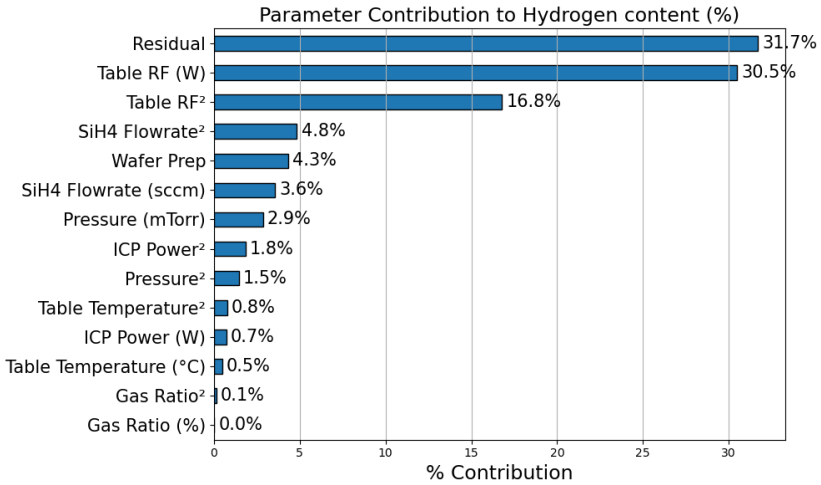

Figure 5.22: Percentage contribution of each deposition parameter to the hydrogen content, based on a regression model. Each numerical factor is represented by a linear term and a squared term to account for potential non-linear effects. The bar lengths indicate the relative importance of each term in explaining the variance in the data.

The relatively high residual contribution implies that the model has limitations in fully capturing the variation in hydrogen content. This is supported by Figure 5.23, which shows clear deviations between the measured and predicted values for several recipes. Across the experiments, the measured hydrogen content ranged from 6.8% to 18.9%, reflecting substantial variability not entirely explained by the fitted model. The corresponding contour plots are provided in Appendix B.

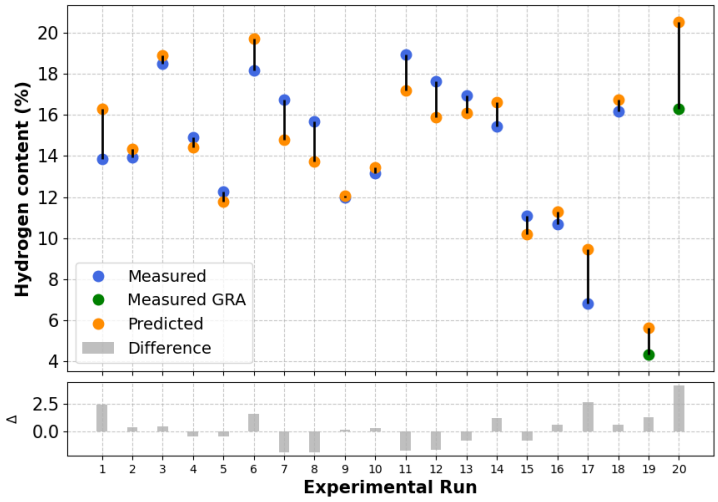

Figure 5.23: Comparison between measured and regression model–predicted hydrogen content values across all experimental runs. The alignment indicates the model's ability to capture the variation in the data, while larger deviations correspond to higher residual variance as observed in the ANOVA. Recipes 19 and 20 were conducted after the Grey Relational Analysis (see Section 5.5).

5.2.8. Microstructure parameter

The Main Effect Plot for the microstructure parameter shows several clear trends across the deposition parameters. Increasing the table temperature results in a consistent increase in the microstructure parameter. Both Table RF power and ICP power exhibit non-linear trends, with the highest values at the intermediate level. Chamber pressure shows a U-shaped trend, with the lowest value at the middle level. Flow rate and gas ratio display mild upward and downward trends, respectively. Wafer preparation using an HF dip corresponds to a lower average microstructure parameter.

The observed increase with SiH_4 flow rate agrees with the results of Singh et al. [53]. The observed increase in microstructure parameter with rising temperature contradicts the findings of Buijtendorp [5]. The physical origin of this difference is unclear. It is possible that the trend is influenced by uncertainties in the Taguchi analysis. Since the ANOVA contribution is negligible (Figure 5.25), the result may be misleading due to unmodeled interaction effects. Buijtendorp's study, in contrast, varied only the temperature and was therefore not effected by such interactions.

Additionally, a regression model is fitted to the recipes, which is shown below:

$$\hat{y}_{R^*} = 0.305 - 0.033 \cdot D_{\mathrm{HF}} - 0.002 \cdot T + 0.000 \cdot T^2 + 0.001 \cdot F - 0.000 \cdot F^2 + 0.001 \cdot I \\ - 0.000 \cdot I^2 + 0.008 \cdot R - 0.000 \cdot R^2 - 0.030 \cdot P + 0.002 \cdot P^2 + 0.003 \cdot G - 0.000 \cdot G^2$$

where T is the table temperature (°C), F is the SiH_4 flow rate (sccm), I is the ICP power (W), R is the table RF power (W), P is the pressure (mTorr), and G is the gas ratio (%) The variable D_{HF} is a binary dummy variable that equals 1 if HF dip wafer preparation was used, and 0 if Argon milling was used.

The ANOVA results, shown in Figure5.25, indicate that Table RF power is the dominant factor, contributing 49.0% when combining its linear and quadratic terms. This confirms the strong and non-linear effect observed in the Main Effect Plot. ICP power follows with a total contribution of 19.4%, while chamber pressure accounts for 9.6%. All remaining parameters contribute less than 5%. The residual variance of 17.0% suggests that the model captures the dominant trends, though a portion of the variation remains unexplained.

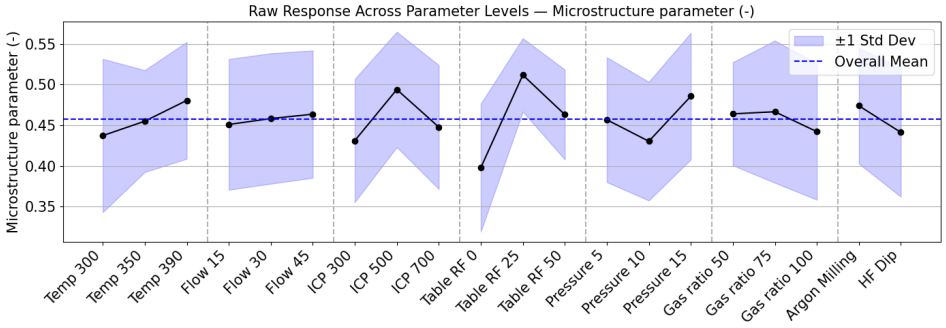

Figure 5.24: Main Effect Plots of the microstructure parameter measurement across all levels of the seven deposition parameters. Each black point represents the average microstructure parameter measured at a given parameter level, while the blue-shaded region indicates the ±1 standard deviation range. The dashed horizontal line denotes the overall mean microstructure parameter across all experiments.

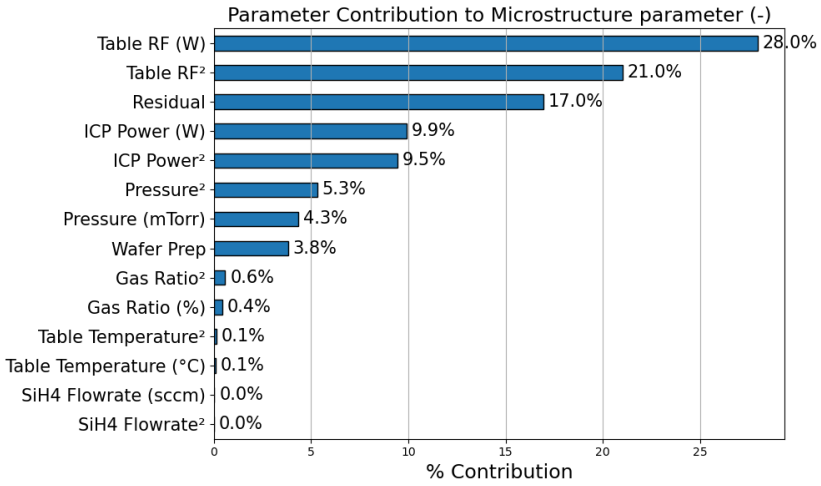

Figure 5.25: Percentage contribution of each deposition parameter to the microstructure parameter, based on a regression model. Each numerical factor is represented by a linear term and a squared term to account for potential non-linear effects. The bar lengths indicate the relative importance of each term in explaining the variance in the data.

This is further supported by Figure Figure5.26, which compares the measured and predicted values across all recipes. Across all experiments, the microstructure parameter ranged from 0.33 to 0.55. While the model captures the overall behavior, several deviations are observed, in line with the 17.0% residual contribution. The corresponding contour plots are provided in Appendix B.

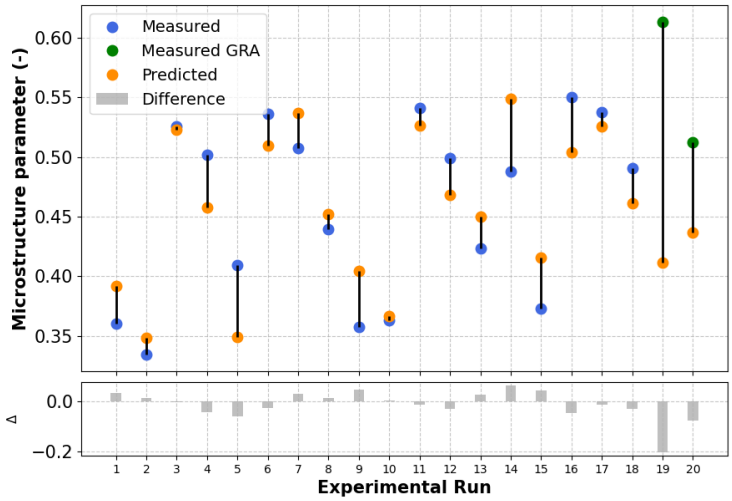

Figure 5.26: Comparison between measured and regression model–predicted microstructure parameter values across all experimental runs. The alignment indicates the model's ability to capture the variation in the data, while larger deviations correspond to higher residual variance as observed in the ANOVA. Recipes 19 and 20 were conducted after the Grey Relational Analysis (see Section 5.5).

5.3. Determine optimal recipe for individual material properties

In this section, the optimal recipes for each individual material property are discussed, based on the Main Effect Plots of the S/N ratios. The motivation for using S/N ratios to determine the optimal recipe is explained in Section 2.6. The analysis also considers the percentage contributions obtained from ANOVA.

5.3.1. Residual stress

To determine the optimal recipe for residual stress, both the single-side polished (SSP) and double-side polished (DSP) wafer results are considered. During this project, the aim was to achieve a residual stress of 0 MPa in the film. Therefore, the target-is-best S/N ratio formula (Equation 2.19) was used, with a target value of zero. The corresponding S/N ratio Main Effect Plots are shown in Figure 5.27.

For the parameters table temperature, ICP power, Table RF power, and wafer preparation, the optimal parameter levels are consistent between SSP and DSP results. However, for the flow rate, pressure, and gas ratio, the optimal levels differ slightly. These shifts result from slight changes in their trends, amplified by the logarithmic loss function in the S/N formula, as described in Section 2.6. However, the ANOVA results show that these parameters have insignificant contributions to the residual stress compared to Table RF power. Therefore, the practical difference in stress between the two optimal recipes is expected to be minimal.

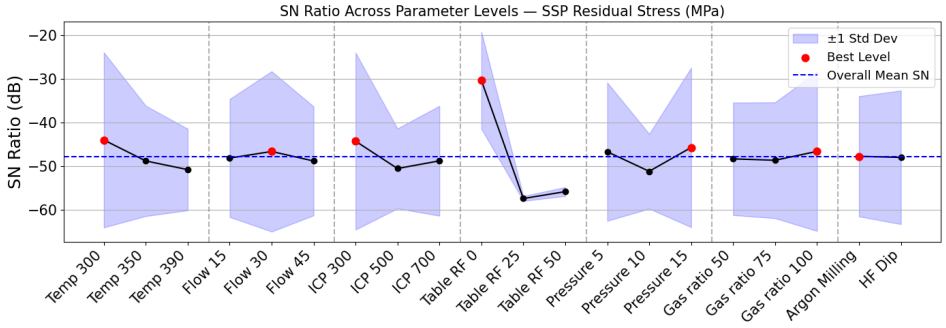

(a) SSP residual stress. Black points represent the average S/N ratio per parameter level; the blue-shaded area indicates ±1 standard deviation. Red markers indicate the optimal level, which correspond to the highest S/N ratio.

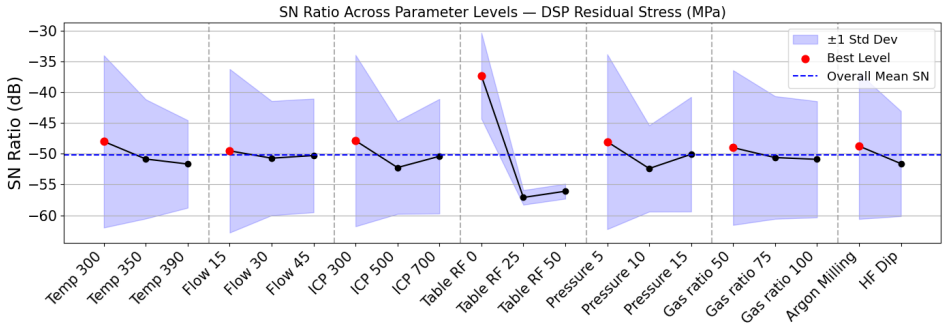

(b) DSP residual stress. Same format as (a), showing S/N ratio response across all deposition parameter levels.

Figure 5.27: S/N ratio main effect plots for SSP and DSP residual stress measurements across all deposition parameters.

5.3.2. Thickness non-uniformity

To determine the optimal recipe that minimizes thickness non-uniformity, the smaller-is-better S/N ratio formula (Equation 2.18) is applied. The resulting S/N ratio Main Effect Plots are shown in Figure 5.28, with the optimal parameter levels—those with the highest S/N ratio—highlighted in red. Based on this analysis, the optimal recipe is defined by: a table temperature of 350 °C, a SiH_4 flow rate of 15 sccm, an ICP power of 700 W, a table RF power of 25 W, a chamber pressure of 10 mTorr, a gas ratio of 100%, and wafer preparation via HF dip.

The ANOVA results in Figure 5.10 support these findings. Table RF power is by far the most dominant parameter, contributing nearly 70% to the observed variance. This strong statistical influence confirms that selecting a table RF power of 25 W is critical to minimizing thickness non-uniformity. In contrast, the contributions of flow rate (4.7%), wafer preparation (4.7%), and pressure (4.1%) are comparatively minor, indicating their effects are secondary in this optimization. Table temperature shows negligible contribution, confirming that the selected value of 350 °C has minimal impact on uniformity in this context.

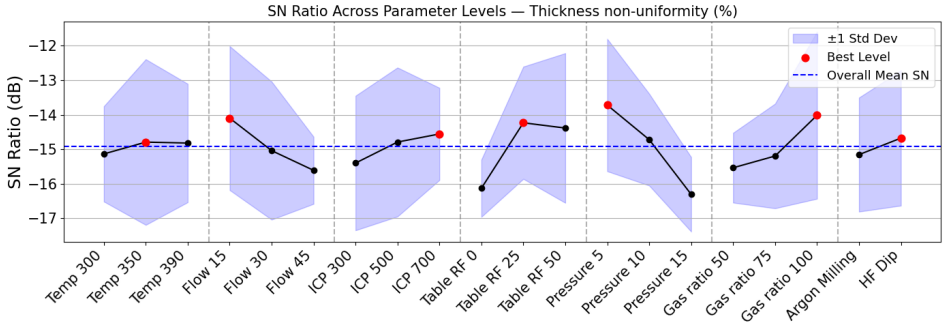

Figure 5.28: S/N ratio Main Effect Plots for thickness non-uniformity across all levels of the seven deposition parameters. Black points represent the average S/N ratio at each parameter level, with the blue-shaded area indicating the ±1 standard deviation. The dashed horizontal line shows the overall mean S/N ratio. Red markers indicate the parameter level with the highest S/N ratio.

5.3.3. Refractive index: Optical and infrared

An increasing refractive index is correlated with a lower void fraction, as explained in Section **??**. Therefore, the larger-is-better S/N ratio formula (Equation 2.17) is applied to compute the S/N ratios. The corresponding S/N ratio Main Effect Plots are shown in Figure 5.29. For both the optical refractive index at 1200 nm and the infrared refractive index at 2800 cm^{-1}, the optimal recipe is largely consistent and correspond to: a table temperature of 350 °C, a SiH_4 flow rate of 45 sccm, an ICP power of 300 W, a table RF power of 50 W, a pressure of 10 mTorr, and wafer preparation via HF dip. Only the gas ratio shows an inconsistent optimal level; 50% for the optical index and 75% for the infrared.

The ANOVA results in Figure 5.13 support the optimal settings identified from the S/N analysis. For both refractive indices, table temperature contributes significantly (14.8% for optical, 13.8% for infrared), indicating the importance of operating at 350°C. Table RF power and chamber pressure are the most influential parameters for the optical and infrared refractive index, respectively, indicating the need to optimize their levels. ICP power also plays a meaningful role in the optical index, contributing 12.8%. In contrast, the contributions of SiH_4 flow rate, gas ratio, and wafer preparation are minimal. The low contribution of gas ratio explains the difference between its optimal levels across the two measurements. Finally, the residual contributions of 42.8% for the optical and 48.0% for the infrared refractive index, indicate that unmodeled effects are likely present.

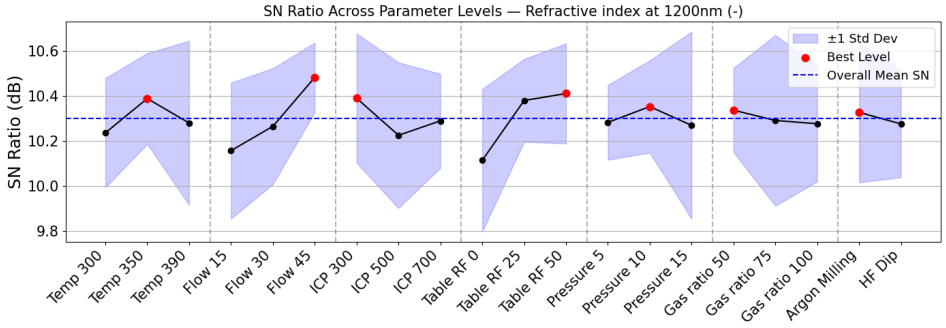

(a) S/N ratio Main Effect Plot for optical refractive index (1200 nm). Black points represent the average S/N ratio at each parameter level, with the blue-shaded area indicating the ±1 standard deviation. The dashed horizontal line shows the overall mean S/N ratio. Red markers indicate the optimal parameter level.

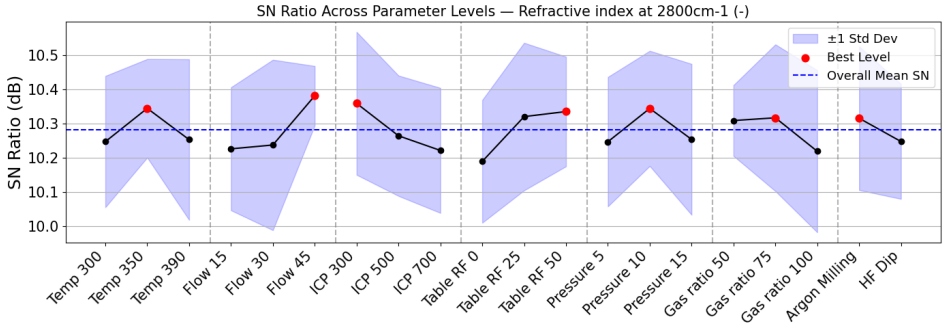

(b) S/N ratio Main Effect Plot for infrared refractive index (2800 cm^{-1}). Plot elements follow the same convention as in (a).

Figure 5.29: Comparison of S/N ratio Main Effect Plots for refractive index at 1200 nm and 2800 cm^{-1} across all deposition parameters.

5.3.4. Band gap

A decreasing band gap is associated with a lower void fraction, as explained in Section **??**. Therefore, the smaller-is-better S/N ratio formula (Equation 2.18) is used to compute the S/N ratios. The corresponding S/N ratio Main Effect Plots are shown in Figure 5.30. The optimal parameter levels correspond to: a table temperature of 390 °C, a SiH_4 flow rate of 30 sccm, an ICP power of 700 W, a table RF power of 25 W, a pressure of 5 mTorr, a gas ratio of 100%, and wafer preparation via argon milling.

The ANOVA results in Figure 5.16 indicate that wafer preparation is the dominant factor, contributing 26.8% to the observed variance. This underlines the critical role of wafer surface condition in determining the band gap. The SiH_4 flow rate also shows a significant influence (15.2%), showing its relevance in the optimization. All other parameters, including table RF power, ICP power, and temperature, contribute only minimal, suggesting that they may support fine-tuning. The substantial residual contribution of 44.6% indicates that a large portion of the variation remains unexplained by the current model, likely due to unmodeled interactions.

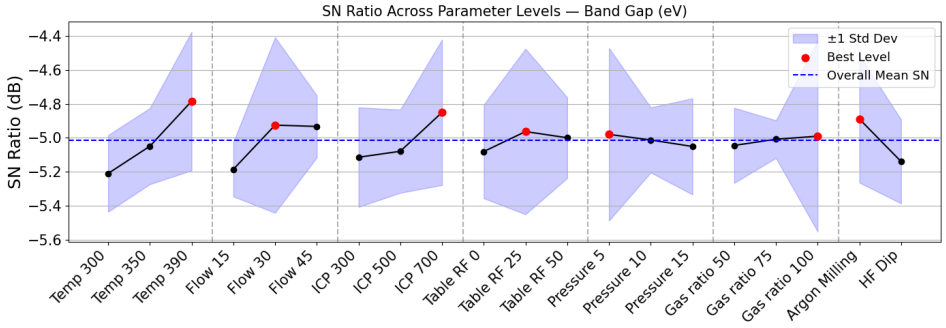

Figure 5.30: S/N ratio Main Effect Plots for band gap across all levels of the seven deposition parameters. Black points represent the average S/N ratio at each parameter level, with the blue-shaded area indicating the ±1 standard deviation. The dashed horizontal line shows the overall mean S/N ratio. Red markers indicate the parameter level with the highest S/N ratio.

5.3.5. Void-volume fraction

To minimize the void-volume fraction, the smaller-is-better S/N ratio formula (Equation 2.18) is applied. The resulting S/N ratio Main Effect Plots are shown in Figure 5.31. The optimal parameter levels, indicated by the red markers, are: a table temperature of 390 °C, a SiH_4 flow rate of 45 sccm, an ICP power of 300 W, a table RF power of 50 W, a pressure of 10 mTorr, a gas ratio of 100%, and HF dip oxidation removal.

The ANOVA results presented in Figure 5.19 confirm that the optimization is mainly driven by chamber pressure. The pressure accounts for 20.3% of the total variation, making it the most influential parameter for controlling the void-volume fraction. The table RF power follows with a contribution of 9.7%. Other parameters such as SiH_4 flow rate (4.0%) and gas ratio (2.3%) play minor roles in the optimization. Additionally, the residual variance is high (60.5%), indicating that a substantial portion of the response remains unexplained by the included parameters, which may be attributed to noise factors or interactions not captured in the model. This, can probably limit the ability to accurately predict the optimal recipe.

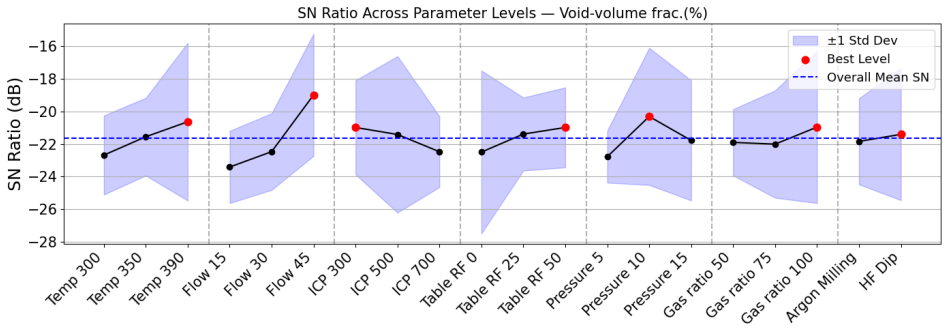

Figure 5.31: S/N ratio Main Effect Plots for void-volume fraction across all levels of the seven deposition parameters. Black points represent the average S/N ratio at each parameter level, with the blue-shaded area indicating the ±1 standard deviation. The dashed horizontal line shows the overall mean S/N ratio. Red markers indicate the parameter level with the highest S/N ratio.

5.3.6. Hydrogen content

As explained in Section **??**, the hydrogen content exhibits opposite correlations for the two dielectric loss mechanisms. An increase in hydrogen content enhances infrared vibrational absorption, an important loss mechanism in the mm–submm range, thereby increasing dielectric loss in the frequency band used by the filterbanks in TIFUUN and DESHIMA (see Figure 1.7). Consequently, minimizing the hydrogen content is desirable for the a-Si:H films used in the microstrip lines that construct the filterbanks.

Conversely, hydrogen atoms are known to passivate dangling bonds, which are associated with two-level systems (TLSs). TLS losses dominate in the 1–10 GHz range, which is the operation range of the parallel-plate capacitors. Due to these competing correlations, two optimal recipes are presented: one for minimizing and one for maximizing the hydrogen content.

To minimize hydrogen content in the films, the smaller-is-better S/N ratio formula (Equation 2.18) is applied. The corresponding Main Effect Plots are shown in Figure 5.32a, where optimal parameter levels are indicated in red. The S/N ratios indicate that hydrogen content is minimized with the following settings: a table temperature of 390 °C, a SiH_4 flow rate of 30 sccm, an ICP power of 700 W, a table RF power of 0 W, a pressure of 5 mTorr, a gas ratio of 100%, and performing argon milling prior to deposition.

To maximize hydrogen content, the larger-is-better S/N ratio formula (Equation 2.17) is used. The corresponding Main Effect Plots are shown in Figure 5.32b, with optimal levels again marked in red. The optimal settings for maximizing hydrogen content are: a table temperature of 300 °C, a SiH_4 flow rate of 45 sccm, an ICP power of 300 W, a table RF power of 50 W, a pressure of 15 mTorr, a gas ratio of 50%, and performing an HF dip prior to deposition.

The ANOVA results in Figure 5.22 confirm that table RF power is the dominant factor, contributing 47.3% to the variance. This indicates its critical role in controlling hydrogen content. Moderate contributions from SiH_4 flow rate (8.4%), pressure (4.4%), and wafer preparation (4.3%) support their importance in fine-tuning the hydrogen level. In contrast, table temperature and gas ratio show relatively minor contributions, indicating that their selected levels are less critical in this optimization.

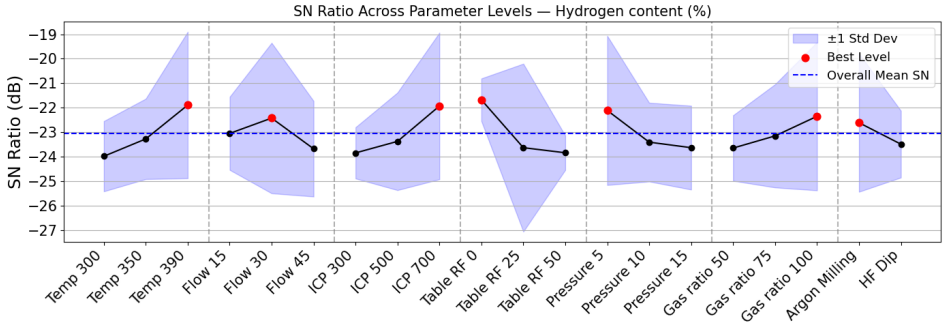

(a) S/N ratio Main Effect Plot for hydrogen content when minimization is desired. The black points represent the average S/N ratio per parameter level, with the blue-shaded area indicating ±1 standard deviation. The dashed horizontal line marks the overall mean. Red markers indicate the parameter level yielding the lowest expected hydrogen content.

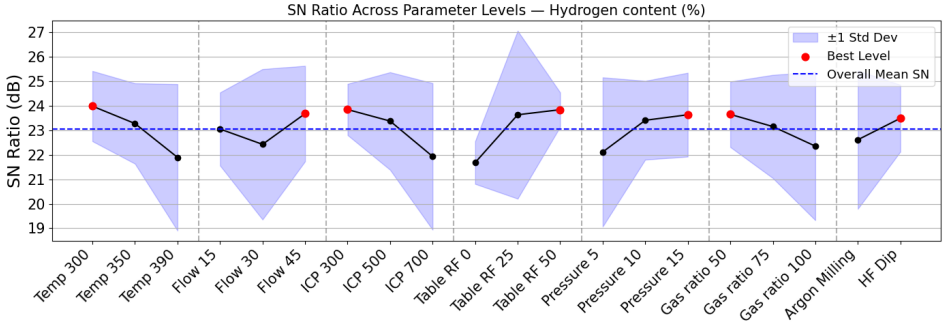

(b) S/N ratio Main Effect Plot for hydrogen content when maximization is desired. Plot elements follow the same convention as in (a), with red markers now indicating the parameter level yielding the highest expected hydrogen content.

Figure 5.32: Comparison of S/N ratio Main Effect Plots for hydrogen content under different optimization goals: (a) minimizing and (b) maximizing hydrogen content.

5.3.7. Microstructure parameter

A decreasing microstructure parameter is correlated with a lower void fraction, as discussed in Section **??**. Therefore, the smaller-is-better S/N ratio formula (Equation 2.18) is used to compute the S/N ratios. Based on the Main Effect Plots shown in Figure 5.33, the optimal recipe for minimizing the microstructure parameter corresponds to the following settings: a table temperature of 300 °C, a SiH_4 flow rate of 15 sccm, an ICP power of 300 W, a table RF power of 0 W, a pressure of 10 mTorr, a gas ratio

of 100%, and performing an HF dip.

The ANOVA results in Figure 5.25 confirm that table RF power is the most influential parameter, contributing 49.0% to the total variance. This highlights the importance of selecting 0 W table RF power for minimizing the microstructure parameter. ICP power also contributes significantly (19.4%), followed by chamber pressure with a moderate influence of 9.6%. Other parameters—including temperature, flow rate, and gas ratio—exhibit minor contributions, indicating that their selected levels play a limited role in this specific optimization.

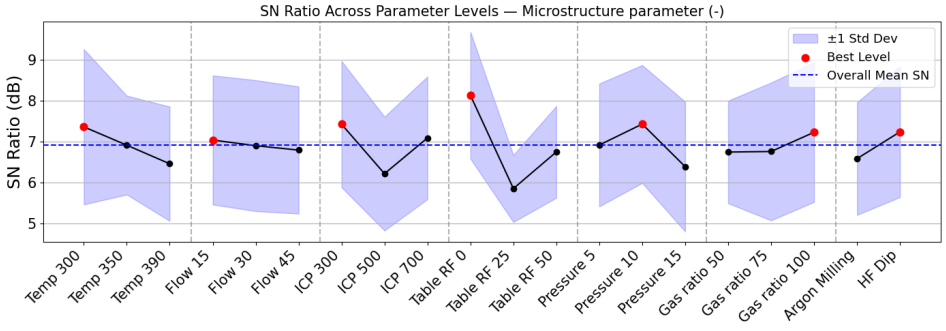

Figure 5.33: S/N ratio Main Effect Plots for microstructure parameter across all levels of the seven deposition parameters. Black points represent the average S/N ratio at each parameter level, with the blue-shaded area indicating the ±1 standard deviation. The dashed horizontal line shows the overall mean S/N ratio. Red markers indicate the parameter level with the highest S/N ratio.

5.4. Grey Relational Analysis: Determine overall optimal recipe

In this section, the results of the Grey Relational Analysis (GRA), as introduced in Section 2.8, are presented. This analysis identifies the optimal level settings of the deposition parameters that simultaneously optimize all targeted material properties. Based on these results, I will present an optimal deposition recipe designed for each of the two main applications of a-Si:H in on-chip spectrometers.

5.4.1. Relative importance properties: Weighted average

To perform the Grey Relational Analysis, it is first necessary to define which material properties are relevant and assign their relative importance. This is done by selecting appropriate weights, which determine each property's contribution to the final Grey Relational Grade (GRG).

Only material properties directly or indirectly linked to dielectric losses are included in the GRA. This includes all measured properties except for residual stress and deposition uniformity. Although excluded from the GRG calculation, the values of these two properties for the resulting optimal recipe will be evaluated.

As discussed in the Introduction, the a-Si:H film has two intended applications: as the dielectric in parallel-plate capacitors (PPCs), operating in the 1–10 GHz range, and in microstrip lines, which form the filterbank of on-chip spectrometers such as TIFUUN (operating at 90–360 GHz). The dominant loss mechanism for PPCs is expected to be two-level systems (TLSs), while for the microstrip lines, the infrared vibrational absorption tail also becomes significant.

As described in Section 2.5, the hydrogen content affects both loss mechanisms but in opposite ways. A lower hydrogen content reduces the infrared absorption tail, which is important for microstrip line applications. In contrast, a higher hydrogen content passivates dangling bonds, which are associated with TLSs, making it beneficial for PPCs. Therefore, the hydrogen content will be minimized for the microstrip application and maximized for the PPC application.

The GRA weighting was determined based on the dominant loss mechanisms for each application. In the PPC application, both void-volume fraction and hydrogen content contribute to TLS losses, as discussed in Section 2.5. For the microstrip application, total dielectric loss arises from TLS and from infrared absorption, the latter being associated with hydrogen content. Therefore, the parameters linked

to void formation, namely the optical and infrared refractive index, void-volume fraction, band gap, and microstructure parameter, are considered to be equally important as the hydrogen content.

To reflect this, the hydrogen content is given a weight of 8, and the void-related parameters are assigned equal shares summing to the same weight. This results in weights of 2 for the void-volume fraction, band gap, and microstructure parameter, and 1 each for the optical and infrared refractive index. This ensures that the total weight associated with void-related properties equals that of the hydrogen content.

In conclusion, the same weighting scheme is used for both applications, but the target direction for the hydrogen content differs: minimization for microstrip applications and maximization for PPCs.

5.4.2. Overall score of each recipe: Grey Relational Grade

The resulting Grey Relational Grades (GRGs) for both applications are presented in Figure 5.34. In both cases, the Grey Relational Analysis combines all quality indicators into a single score per recipe, allowing for direct comparison.

When hydrogen content is minimized (Figure 5.34a), recipe 17 achieves the highest GRG, indicating it offers the best overall performance across all considered material properties for the filterbank application. Conversely, when hydrogen content is maximized (Figure5.34b), recipe 11 performs best, making it the most suitable for PPC-based applications.

More importantly, the GRG distributions differ significantly between the two cases, highlighting that the optimal recipes for these applications are significantly different. This observation aligns with the differences in dominant loss mechanisms and is further discussed in the following section.

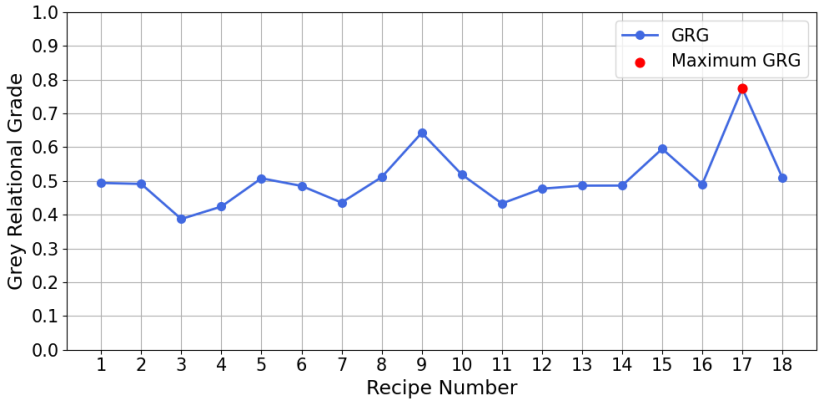

(a) Grey Relational Grade for each recipe when hydrogen content is minimized.

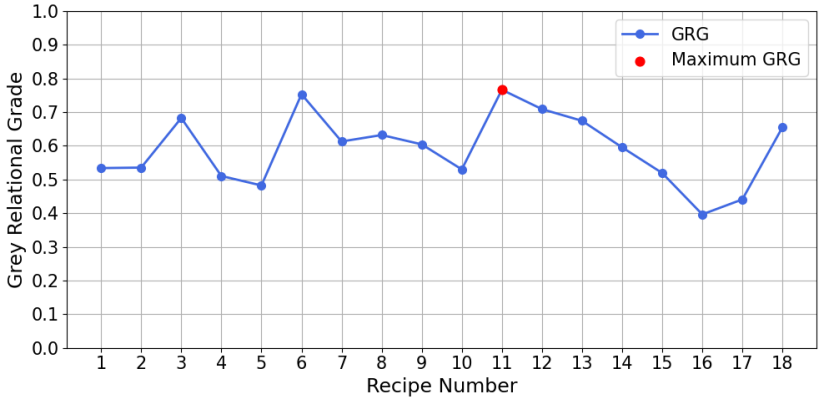

(b) Grey Relational Grade for each recipe when hydrogen content is maximized, using the same response weights.

Figure 5.34: Grey Relational Grade (GRG) for each recipe under two optimization objectives: (a) minimizing and (b) maximizing hydrogen content. The red marker indicates the recipe with the highest overall GRG in each case.

5.4.3. Optimal recipes for the two applications: PPC and filterbank

The Main Effect Plots of the GRG for both design targets are shown in Figure 5.35. For the case where hydrogen content is minimized (Figure 5.35a), the optimal parameter levels are: 390 °C table temperature, 30 sccm SiH_4 flow, 700 W ICP power, 0 W table RF, 5 mTorr pressure, 100% gas ratio, and argon milling surface preparation.

The corresponding ANOVA results (Figure 5.36a) indicate that ICP power (20.3%) and SiH_4 flow rate (17.4%) are the most influential parameters. Wafer preparation also contributes significantly with 11.0%. Interestingly, table RF power, despite its importance in other properties, contributes only 4.0% in this optimization. The high residual variance (42.2%) suggests that parameter interactions or other unmodeled effects account for a substantial portion of the GRG variation.

In the case where hydrogen content is maximized (Figure 5.35b), the optimal settings shift to: 300°C table temperature, 45 sccm SiH_4 flow, 300 W ICP power, 25 W table RF, 10 mTorr pressure, 75% gas ratio, and HF dip preparation.

Here, the ANOVA results (Figure 5.36b) show that table RF power is the dominant parameter, accounting for 62.2% of the total variance. The next highest contributor is pressure, with a relatively minor 11.5%. This dominant role of table RF power aligns with its strong influence on hydrogen content, as discussed earlier. The contour plots of the Grey Relational Grades of both optimal recipes are provided in Appendix B.

It is important to note that the film deposited using the recipe optimized for the PPC application is expected to exhibit a high compressive stress, due to the table RF setting of 25 W (see trend in Figure 5.6). In contrast, the recipe optimized for the microstrip filterbank application (i.e., minimizing hydrogen content) is expected to result in a slightly tensile or near-zero stress level.

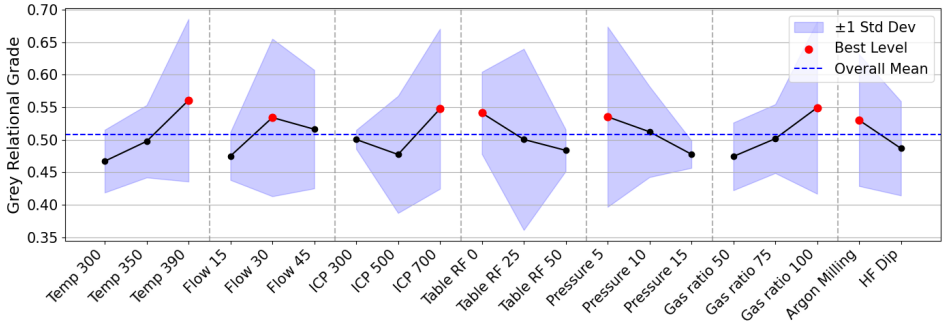

(a) Main Effect Plots of the Grey Relational Grade for the case where hydrogen content is minimized. The optimal level for each parameter is highlighted in red.

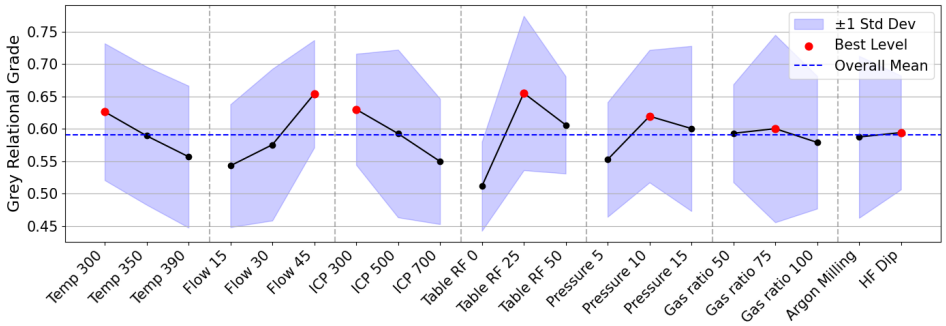

(b) Main Effect Plots of the Grey Relational Grade for the case where hydrogen content is maximized. The optimal level for each parameter is again highlighted in red.

Figure 5.35: Main Effect Plots of the Grey Relational Grade for two design targets: (a) minimizing hydrogen content and (b) maximizing hydrogen content. The plots indicate which level of each factor contributes most to improving overall multi-objective performance.

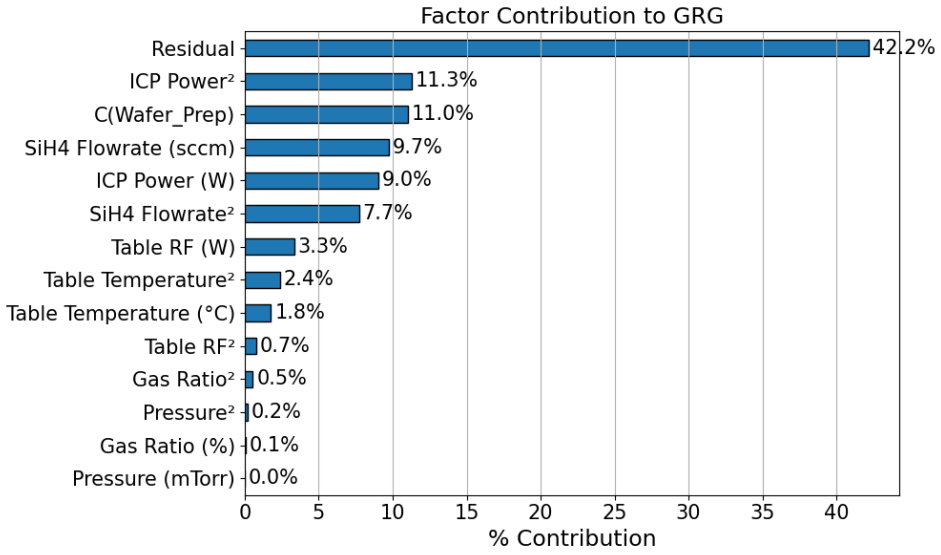

(a) The ANOVA results for the case where hydrogen content is minimized. Table RF power has limited influence, while ICP power and SiH_4 flow rate dominate.

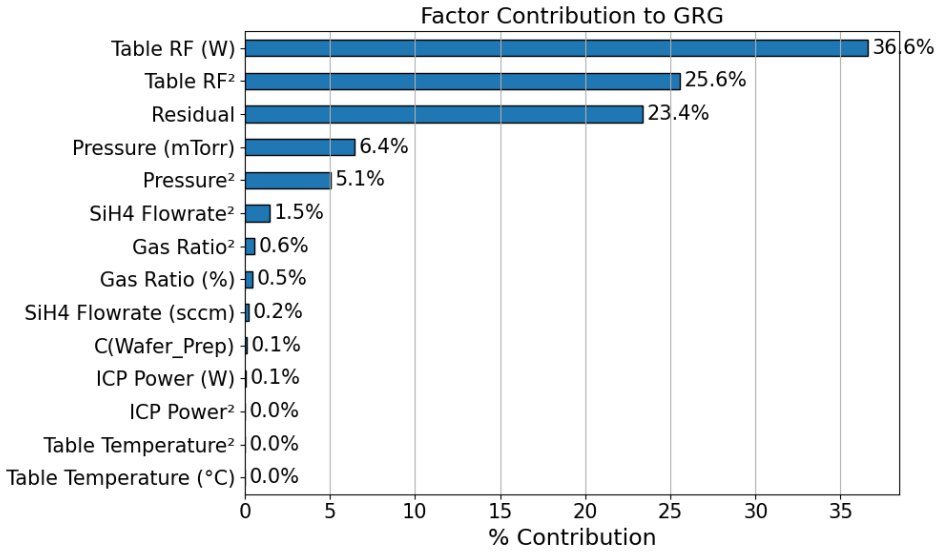

(b) The ANOVA results for the case where hydrogen content is maximized. Table RF power is by far the dominant factor.

Figure 5.36: The ANOVA results showing the parameter contributions to the Grey Relational Grade (GRG) for two optimization cases.

5.5. Verification of optimal experiments

Both recipes identified through the Grey Relational Analysis are not part of the conducted orthogonal array (see Table 2.1). This indicates that the analysis selected new combinations of parameter levels that are expected to outperform the originally tested recipes. As a final step, these predicted optimal recipes will be executed and their material properties measured to verify the prediction.

5.5.1. Fabrication and transmission spectra

To test the the accuracy of the predicted optimal recipes, each recipe was processed on the same method as done for each of the recipes in the Taguchi array. This means that we have deposited each of the optimal recipes on both a SSP and DSP wafer, for ellipsometry and FTIR, respectively. This included a running a precondition recipe to coat the chamber walls, and performing an Argon milling or HF dip for the minimizing or maximizing recipe, respectively. The average thickness of the recipe minimizing or maximizing the hydrogen content was 561nm and 537nm, measured using ellipsometry, respectively.

After depositing the films, I have measured all material properties, as explained in Section 4. The transmission spectra of both film measured with the FTIR is shown in Figure 5.37. As explained in Section 4.4.3, the hydrogen content C_H is computed from the integrated area of the SiH wagging mode near 640 cm^{-1}. In Figure 5.37, it is clearly visible that the absorption dip of the recipe which minimizes the hydrogen (blue) is significantly smaller than for the recipe that maximizes hydrogen (orange). Additionally, the stretching modes around 2000 and 2100 cm−1, which are caused by the Si-H and Si-H_2, respectively, show the same decrease, which supports the observation that there is a strong difference in the hydrogen content between the films. Although, this was predicted by the Grey Relational Analysis, it is important to observe this difference, as hydrogen is contributing strongly in the optimization design. The refractive index curves from ellipsometry, the extinction coefficient and the corresponding infrared refractive index curves measured with the FTIR, and the thickness non-uniformity plots are shown in Appendix A.

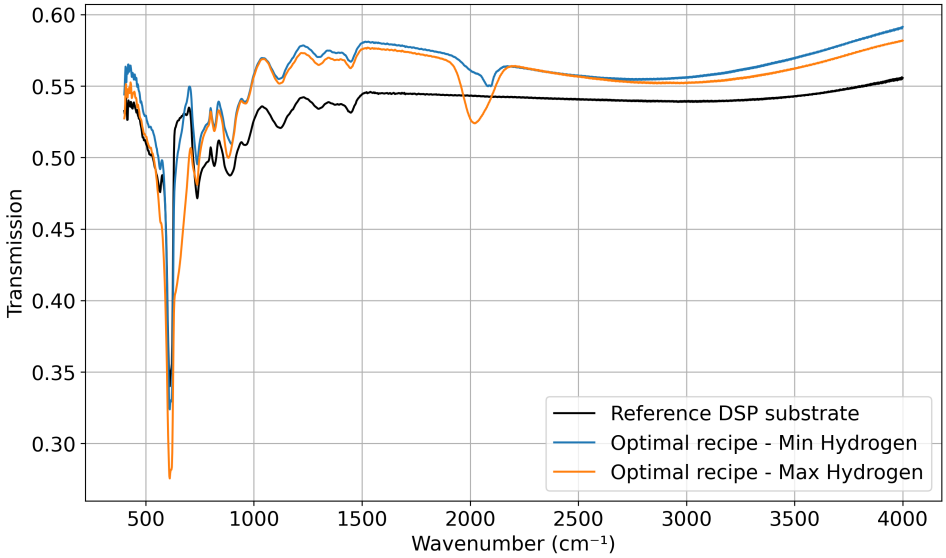

Figure 5.37: FTIR transmission spectra of the two optimal films, deposited using recipes designed to minimize (blue curve) and maximize (orange curve) the hydrogen content. The transmission spectrum of the bare DSP silicon substrate is included as a reference (black curve).

5.5.2. Optimal recipe: Minimizing hydrogen content

Prediction vs measurement

In this section, the performance of the optimal recipe which minimizes the hydrogen content will be discussed. This will be done by comparing the measured material properties with the predictions from both the method described in Section 2.6, which uses Equation 2.21, and the predictions from the regression model. An overview of the measured and predicted values is shown in Table 5.1.

The Grey Relation Grade (GRG) of this recipe is predicted to be 0.7475, calculated with Equation 2.21, as described in Section 2.8. However, the actual GRG scored higher than this prediction with a 0.774, thereby outperforming every other recipe based on the recalculated GRGs. This outperformance of the prediction is mainly driven by a lower than expected measured hydrogen content.

Overall, the measured results align reasonably well with the predicted trends, though several properties deviate significantly in magnitude. The measured deposition rate of 32.06 nm/min lies between the two predictions: 30.38 nm/min from the S/N method and 33.59 nm/min from the regression model. Residual stress values show larger discrepancies than expected, particularly given that stress had the lowest residual contribution in the ANOVA results. The measured SSP stress of –121.6 MPa is substantially more compressive than both predictions, with the strongest underestimation coming from the regression model, which gave a value of only –7.41 MPa. Similarly, the measured DSP stress of –28.5 MPa falls between the S/N prediction (–69.2 MPa) and the regression result (140.0 MPa), indicating weak predictive performance for stress-related outcomes.

The thickness non-uniformity was measured at 7.59%, exceeding both predictions, which were close to 5%. This suggests that the model underestimated the non-uniformity in film growth under the selected conditions. Optical and infrared refractive indices were well predicted by both methods, with deviations within 0.07 absolute units, where the prediction of the infrared refractive index was slightly more accurate. The band gap was slightly overestimated by both models, with measured and predicted values differing by roughly 0.07 eV. Similarly, the void-volume fraction was predicted with moderate accuracy, with a measured value of 14.9% versus predicted values of 15.7% and 16.6%.

The largest improvement over the predictions is observed in the hydrogen content, which was measured at 4.33%, below the predicted values of 6.84% (S/N model) and 5.64% (regression model). This lower hydrogen content strongly contributes to the higher than expected GRG. Finally, the microstructure parameter was also significantly underestimated by both models, with a measured value of 0.61 compared to predicted values around 0.41. This higher than expected microstructure parameter is visualized in Figure 5.37, where the area stretching mode of the Si–H_2 is relatively strong.

In summary, while some properties were predicted with reasonable accuracy, others, particularly thickness non-uniformity and the microstructure parameter, deviate significantly.

Property	Actual	Predicted via SNR	Regression model
Grey Relational Grade (-)	0.7740	0.7475	0.7475
Deposition rate (nm/min)	32.06	30.38	33.59
SSP residual stress (MPa)	-121.6	-33.1	-7.41
DSP residual stress (MPa)	-28.5	-69.2	140.0
Thickness non-uniformity (%)	7.59	4.98	5.092
Optical refractive index (-)	3.239	3.171	3.171
Infrared refractive index (-)	3.143	3.160	3.160
Band gap (eV)	1.592	1.662	1.665
Void-volume fraction (%)	14.9	15.69	16.55
Hydrogen content (at.%)	4.33	6.84	5.64
Microstructure parameter (-)	0.613	0.405	0.412

Table 5.1: Comparison of actual material properties for the optimal recipe minimizing hydrogen content, with predictions obtained using the S/N ratio-based formula (Equation 2.21) and the regression model.

Performance optimal recipe relative to other recipes

The optimal recipe for minimizing hydrogen content is now evaluated against the other experimental runs based on its measured material properties. This comparison is visualized in Section 5.2, where Recipe 19 corresponds to the optimal recipe for minimizing hydrogen content.

The deposition rate of Recipe 19 is approximately 30 nm/min, placing it near the middle of the dataset. While several recipes exhibit significantly higher rates exceeding 45 nm/min, others fall below 15 nm/min. Recipe 19 thus represents a moderate growth rate. The SSP residual stress measured for Recipe 19 is -122 MPa, which is significantly less compressive than for most other recipes. The majority of samples exhibit compressive stress values in the range of -600 MPa to -800 MPa, indicating higher internal stress levels. However, when compared with other recipes with table RF power equal to zero, it has the highest compressive stress, significantly lower than predicted. Its relatively low stress is favorable, as it reduces the risk of delamination in the final application. With a measured DSP residual stress of –29 MPa, Recipe 19 has a compressive stress that is close to zero. This is remarkable, since all other recipes with the same table RF show compressive stress, as was predicted by the regression model. However, this stress level has lower risk of delamination compared to the recipes with a non-zero table RF.

The measured non-uniformity of 7.6% in Recipe 19 is the highest observed, significantly higher than the predicted 5.1%. Most other recipes exhibit lower non-uniformity between 4% and 7%. This shows that this recipe has the least uniform film. Recipe 19 exhibits an optical refractive index near 3.24, which is around the middle of the dataset spread between 3.1 and 3.4. This indicates that the film is not among the densest films. Similar to the optical index, the infrared refractive index for Recipe 19 is relatively low (3.14), placing it between the lowest measurements. This supports the observation that the density of the film is among the lowest.

With a band gap of 1.59 eV, Recipe 19 is comparable to Recipe 17, which are both outliers as the other recipes fall in the 1.72–1.90 eV range. This lower band gap corresponds to a lower void-volume fraction and higher refractive index, which is not observed in these recipes. Additionally, both these wafers have clouded surfaces and a deviating optical refractive index curve, presented in Appendix E and A, respectively. Recipe 19 shows a void-volume fraction of 14.9%, which is around average. Most measurements are between 7.5% and 17.5%. Although the recipe was partially designed to minimize the void density of the film, the film does not outperform most of the films. One explanation could be that the high importance of the hydrogen content in the Grey Relational Analysis resulted in a recipe with a higher void density. This is supported by the relatively high predicted void-volume fraction of Recipe 19.

Recipe 19 clearly outperforms all others with the lowest measured hydrogen content, around 4.3%. The next best (Recipe 17) still exhibits >6.8%, while many others exceed 15%. This confirms Recipe 19 as the most successful in minimizing hydrogen content, which was the primary objective. Recipe 19 exhibits a microstructure parameter of approximately 0.61, the highest among all measured samples, whereas most other recipes fall within the range of 0.35 to 0.55. This elevated value is consistent with the observed low hydrogen content in the film. The low hydrogen content is in agreement with a relatively shallow Si–H wagging mode near 640 cm^{-1} and a suppressed Si–H stretching mode around 2000 cm^{-1} in the FTIR spectrum. These observations correspond to the higher microstructure parameter. However, the difference between the measured and predicted microstructure parameter for this recipe is remarkable.

5.5.3. Optimal recipe: Maximizing hydrogen content

Prediction vs Measurement

In this section, the performance of the optimal recipe which maximizes the hydrogen content will be discussed. This will be done by comparing the measured material properties with the predictions from both the method described in Section 2.6, which uses Equation 2.21, and the predictions from the regression model. An overview of the measured and predicted values is shown in Table 5.2.

The Grey Relation Grade (GRG) of this recipe is predicted to be 0.8345, calculated with Equation 2.21, as described in Section 2.8. However, the actual GRG scored significantly lower than this prediction with a 0.6397, thereby underperforming with respect to 6 other recipes based on the recalculated GRGs. This

underperformance is mainly driven by a lower than expected measured hydrogen content. Overall, the measured results for this recipe show partial agreement with the predictions, although the hydrogen content, which is the main target, falls significantly below expectations. The deposition rate of 29.85 nm/min matches both the S/N-based and regression prediction reasonably well, indicating consistent growth performance.

Residual stress values are well captured by the regression model. The SSP stress was measured at –744.9 MPa, aligning closely with the predicted –774.5 MPa. The DSP stress also shows reasonable agreement, with a measured value of –639.3 MPa compared to predictions of –693.7 MPa (S/N) and –753.3 MPa (regression). These results confirm that both models capture the stress behavior under these deposition conditions. The thickness non-uniformity was measured at 5.61%, which aligns well with both predicted values of approximately 5.9%. This agreement is remarkable given that, for the recipe minimizing hydrogen content, the measured non-uniformity deviated significantly from the prediction.

The optical refractive index of the film (3.42) matches closely with the predicted values, differing by only 0.03. In contrast, the infrared refractive index shows a strong deviation, with a measured value of 3.19 compared to the predicted 3.36. The measured optical band gap of the film is 1.73 eV, approximately 0.1 eV lower than both predicted values. Similar to the recipe optimized for minimum hydrogen content, the band gap is consistently underestimated by the model. Additionally, the void-volume fraction was measured at 7.6%, consistent with predictions (7.8–8.0%), suggesting the porosity was correctly estimated.

The largest deviation is found in the hydrogen content, where a measured value of 16.3 at.% is substantially lower than both predictions (20.5–22.1 at.%). The physical origin of this difference is unclear, though unmodeled interaction effects may partially account for it. As hydrogen content was the primary optimization target, this underperformance directly explains the lower-than-expected GRG score. Finally, the microstructure parameter was significantly underestimated by both models, with a measured value of 0.51 compared to predicted values around 0.43. This higher-than-expected value is consistent with the observed lower hydrogen content in the film. A reduced Si–H stretching absorption near 2000 cm^{-1}, associated with lower hydrogen, leads to a higher microstructure parameter.

In summary, while most structural and optical properties were predicted with reasonable accuracy, the hydrogen content—central to this optimization—was substantially overestimated. This discrepancy significantly reduced the GRG performance of the recipe, placing it below several other experimental runs.

Property	Actual	Predicted via SNR	Regression model
Grey Relational Grade (-)	0.6397	0.8345	0.8345
Deposition rate (nm/min)	29.85	26.56	28.41
SSP residual stress (MPa)	-744.88	-570.56	-774.54
DSP residual stress (MPa)	-639.32	-693.66	-753.29
Thickness non-uniformity (%)	5.61	5.94	5.88
Optical refractive index (-)	3.420	3.388	3.387
Infrared refractive index (-)	3.186	3.356	3.359
Band gap (eV)	1.730	1.840	1.837
Void-volume fraction (%)	7.6	7.967	7.849
Hydrogen content (at.%)	16.31	22.11	20.52
Microstructure parameter (-)	0.512	0.427	0.436

Table 5.2: Comparison of actual material properties for the optimal recipe maximizing hydrogen content, with predictions obtained using the S/N ratio-based formula (Equation 2.21) and the regression model.

Performance optimal recipe relative to other recipes
The optimal recipe for maximizing hydrogen content is now evaluated against the other experimental runs based on its measured material properties. This comparison is visualized in Section 5.2, where Recipe 20 corresponds to the optimal recipe for maximizing hydrogen content.

Recipe 20 showed a deposition rate of 29.85 nm/min, placing it in the mid-range of the dataset. The highest deposition rates exceed 45 nm/min and the lowest drop below 15 nm/min. With a measured SSP residual stress of -744.9 MPa, Recipe 20 ranks among the most compressively stressed films in the dataset, only slightly less extreme than Recipes 8 and 13. While such high compressive stress can pose a risk to mechanical stability—particularly by increasing the likelihood of buckling—it remains well below the failure threshold of -1200 MPa reported by Johlin et al. [23]. Nonetheless, the elevated stress should be considered carefully when evaluating the suitability of this recipe for practical applications. The DSP residual stress of -639.3 MPa also ranks highly compressive, with most other recipes showing similar stress levels between -600 MPa and -800 MPa. Recipe 20 does not stand out significantly for the DSP measurement, but confirms the consistent presence of stress for recipes with a non-zero table RF.

Recipe 20 exhibited a thickness non-uniformity of 5.6%, which lies near the mean of the dataset. Most other recipes fall within the range of 4% to 7%, indicating that the optimal hydrogen recipe does not sacrifice thickness uniformity. The refractive index measured at 1200 cm^{-1} is 3.42, the highest among all recipes. Most other samples range between 3.2 and 3.35. This elevated refractive index indicates that the film is dense, despite its high hydrogen content. The measured FTIR refractive index of Recipe 20 is approximately 3.19, which is among the lowest values of the dataset, with a few recipes (e.g., 2, 16, 17, 19) that have lower values. Recipe 19, by comparison, has a slightly lower value of 3.14. The low value for Recipe 20 does not agree with the relatively high refractive index of the optical refractive index.

Recipe 20's band gap of 1.73 eV is among the lowest values, where the total range of the dataset is between 1.58 eV and 1.90 eV. This lower band gap corresponds to a lower void-volume fraction and higher refractive index, which is observed for this recipe when considering only the optical refractive index. The void-volume fraction of 7.6% for Recipe 20 is among the lowest observed in the dataset. While most other recipes yield values between 7.5% and 17.5%, the film from Recipe 20 stands out as notably denser. This low porosity is consistent with the relatively low and high measured values for the band gap and the optical refractive index, respectively. However, it does not align with the lower-than-expected infrared refractive index and microstructure parameter.

The hydrogen content of 16.3 at.% is relatively high but below the highest recipes, including Recipe 3 and 11, which exceed 18 at.%. Hence, Recipe 20 does not achieve its design objective to produce the most hydrogen-rich film. This deviation significantly impacted its Grey Relational Grade (GRG), which is ranked 7th of all recipes. The microstructure parameter of 0.51 is above average but not the highest (Recipe 19, 0.61). Compared to the rest of the dataset, Recipe 20's microstructure indicates a slightly higher than average void density. However, this observation does not align with the results of the void-volume fraction, optical refractive index, and the band gap.

5.6. Summary of results

This section contains summary with the main takeaways of the established relations between the deposition parameters and each of the material properties. Additionally, a summary of the performance of the two optimal recipes identified in Section 5.4.3 is presented.

5.6.1. Summary of relations between deposition parameters and material properties

The deposition parameters show distinct influences on the material properties of the films, with varying accuracy of the fitted model regression model, across different properties. For the residual stress, the table RF power stands out as the dominant factor by far. Its influence is clearly evident: increasing the table RF power from 0 W to 25 W shifts the average stress from a tensile value of +80 MPa to a highly compressive stress around -750 MPa. Further increasing the power to 50 W slightly reduces the compressive stress, averaging around -650 MPa. This trend is consistent across both SSP and DSP wafers, with table RF power contributing over 97% of the total variation in both cases. The remaining parameters play only a minimal role in stress evolution.

In the case of thickness non-uniformity, the influence of table RF power is again strongest, though less dominant than in the stress analysis. It contributes nearly 70% of the observed variation. A higher table RF power reduces thickness non-uniformity, while other parameters such as SiH_4 flow rate and chamber pressure lead to increased non-uniformity at higher levels. The measured non-uniformity ranges from 3.5% to 7.5%.

The trends for the refractive index — both optical and infrared — are generally consistent across the two measurement methods. For the optical index, table RF power is the most influential parameter, while for the infrared index, pressure plays the leading role. However, both models suffer from relatively high residuals (42.8% and 48.0%, respectively), indicating that interaction effects or unmodeled factors significantly contribute to the observed variance. The optical refractive index varies between 3.02 and 3.40, while the infrared index ranges from 3.14 to 3.35.

For the band gap, the most significant contribution comes from wafer preparation, where HF-dipped wafers consistently show higher band gap values. Wafer preparation alone accounts for 26.8% of the variation, followed by silane flow rate at 15.2%. Despite these contributions, the residual remains high at 44.6%. The measured band gap spans a relatively wide range, from 1.59 eV to 1.90 eV, with recipe 17 as an outlier.

The void-volume fraction is influenced most strongly by chamber pressure (20.3%) and table RF power (9.7%), although the overall model fit is poor, with a residual of 60.5%. The data shows that increasing table temperature, SiH_4 flow, and table RF generally lowers the void fraction, while increasing ICP power raises it. The measured values vary significantly across the dataset, from as low as 4.9% to as high as 21.9%, highlighting the large unexplained variation.

For hydrogen content, table RF power is again the primary driver, contributing 47.3% to the explained variation, with measured values ranging from 6.8% to 18.9%. It introduces a sharp increase in hydrogen content from the lowest to the mid-level RF power, after which the values plateau. Other parameters, including flow rate, pressure, and wafer preparation, play minor roles. The residual of 31.7% indicates that there are still significant effects excluded in the model.

Finally, the microstructure parameter is governed predominantly by table RF power, which contributes nearly half of the total variation, with measured values between 0.33 to 0.55. This effect is non-linear, with the highest microstructure parameter observed at mid-level RF power. ICP power and chamber pressure also contribute (19.4% and 9.6%, respectively), while other factors play a secondary role.

5.6.2. Summary of optimal recipes

This section summarizes the performance of the two optimal recipes identified in Section 5.4.3. Both were selected to minimize the void density, with Recipe 19 specifically designed to minimize hydrogen content, and Recipe 20 to maximize it.

Minimizing hydrogen content: Recipe 19
Recipe 19 is the most successful recipe overall, achieving the highest measured Grey Relational Grade (GRG) of 0.774. It effectively meets its design objective by yielding the lowest hydrogen content in the dataset (4.3 at.%) significantly below all other recipes, which exhibit values above 6.8 at.%.

In terms of performance relative to the rest of the dataset, Recipe 19 has the highest measured microstructure parameter (0.61), relatively low optical and infrared refractive indices (3.24 and 3.14), and an above-average void-volume fraction (14.9%), all consistent with a lower-density film. However, the relatively low band gap does not align with this trend and may be influenced by surface scattering effects (see Appendix E). Additionally, the film shows the highest thickness non-uniformity (7.6%), suggesting a trade-off between hydrogen minimization and thickness uniformity. The residual stress is low at –29 MPa, which is favorable for film stability.

Overall, Recipe 19 clearly fulfills its optimization goal of minimizing hydrogen content. While it achieves minimal success in reducing the void density, the data suggest that hydrogen content is more sensitive to the process parameters than void formation in this case.

Maximizing hydrogen content: recipe 20
Recipe 20 was intended to maximize hydrogen content, but its measured GRG (0.6397) ranks only 7th

among the 20 recipes. Although the measured hydrogen content of 16.3 at.% is relatively high, it falls significantly short of the predicted values (>20 at.%) and is outperformed by several other recipes (e.g., recipes 11, 6 and 12) based on the recalculated GRGs.

Relative to the rest of the dataset, Recipe 20 exhibits high compressive stress in both SSP and DSP measurements (–745 MPa and –639 MPa, respectively), the highest optical refractive index (3.42), and one of the lowest void-volume fractions (7.6%) and band gap values (1.73 eV). These results indicate a dense film. However, the infrared refractive index (3.19) and microstructure parameter (0.51) do not fully support this interpretation.

Recipe 20 only partially meets its design objective. While it resulted in a hydrogen-rich film, it did not outperform several other recipes and failed to reach the targeted hydrogen levels. However, all material properties—except the band gap—indicate a lower void density compared to Recipe 19. This suggests that Recipe 20 was more effective at minimizing void formation, despite the only difference was the target optimization for hydrogen content.

6

Discussion

This Chapter evaluates the performance and limitations of the optimized recipes, assesses the effectiveness of the Taguchi optimization approach, and reviews the predictive accuracy of the regression model. It also considers measurement uncertainties and qualitative observations not fully represented in the numerical data, such as surface cloudiness.

6.1. Performance of the optimized recipes

Two optimized recipes were identified using Grey Relational Analysis. In both cases, half of the total weight was assigned to material properties associated with void density—the void-volume fraction, optical and infrared refractive indices, band gap, and microstructure parameter—while the remaining weight was assigned to hydrogen content. Recipe 19 was optimized for minimal hydrogen content, and Recipe 20 for maximal hydrogen content.

Recipe 19 successfully achieved its objective, yielding the lowest hydrogen content in the dataset at 4.3 at.% and ranking first with a GRG of 0.774. However, the result came with several trade-offs. The film showed the highest thickness non-uniformity (7.6%), a relatively high void-volume fraction (14.9%), and a band gap significantly lower than predicted. Visually, the film surface appeared cloudy, with a high density of fine surface features. A similar, though more pronounced, surface effect was observed for Recipe 17, as shown in Appendix E. Both films also displayed outlying refractive index spectra and band gaps, suggesting a shared structural deviation from the rest of the dataset. On the other hand, the residual stress or Recipe 19 was modest (–29 MPa), indicating no immediate mechanical concerns.

Despite its successful hydrogen minimization, the combination of high void fraction and surface cloudiness makes the practical application of Recipe 19 uncertain. When selecting a recipe without these concerns, Recipe 9 presents itself as a promising alternative. Ranked third (GRG = 0.621), it exhibits no visible surface defects and combines a tensile residual stress of 125 MPa with a hydrogen content of 11.97 at.%, which is among the lower values, but significantly higher than for recipe 17 and 19. However, Recipe 9 offers the lowest void-volume fraction in the dataset and favorable scores for other void-density related properties. Hence, this recipe is a strong candidate for applications in the filterbank section of the on-chip spectrometer.

Recipe 20, optimized for maximum hydrogen content, reached 16.3 at.% but did not achieve the highest value in the dataset. Its GRG (0.640) placed it seventh, indicating that other recipes outperformed it under the chosen optimization criteria. Nevertheless, the film showed favorable density indicators, with a low void-volume fraction (7.6%) and the highest optical refractive index (3.42). However, internal consistency was limited: the IR refractive index (3.19) and a relatively high microstructure parameter (0.51) did not align with dense, hydrogen-rich film. Additionally, the residual stress was high at -745 MPa, raising potential concerns for mechanical stability, although this remains below the failure threshold suggested in [23].

When the high compressive stress is considered acceptable, recipes 11 and 6—ranked first and second

with GRGs of 0.765 and 0.749, present suitable alternatives. Both contain hydrogen contents exceeding 18 at.%, which is the key reason to their high rank. Between the two, Recipe 6 scored slightly better in the material properties related to the void density. Their residual stresses are comparable to Recipe 20 (–770 MPa and –660 MPa).

If the high compressive stress is considered impractical for device integration, Recipe 9 offers a suitable alternative. It is the highest-scoring recipe with a table RF power of 0 W, which results in a relatively low tensile stress of 125 MPa. Although its GRG of 0.603 ranks it only tenth overall, primarily due to a below average hydrogen content of 11.97 at.%, the film performs well across all void density related material properties. It achieved the lowest void-volume fraction in the dataset and scored better than average for the optical and infrared refractive indices, band gap, and microstructure parameter. These indicators point to a dense film. In addition, no surface irregularities were observed. Therefore, despite its lower GRG ranking, Recipe 9 is the most suitable candidate for application in the parallel-plate capacitor when a high compressive stress is considered impractical.

In summary, the Grey Relational Analysis yielded optimal recipes for both targeted applications. For the filterbank, the predicted optimal recipe (Recipe 19) also performed best experimentally, demonstrating the capability of the design approach that it can make accurate predictions. For the parallel-plate capacitor, however, the predicted recipe (Recipe 20) was outperformed, revealing limitations within the optimization progress. In both cases, the best-scoring recipes presented practical concerns: Recipe 19 showed surface irregularities, while Recipe 20 exhibited high residual stress. Remarkably, Recipe 9 emerged as the best-performing alternative free of these limitations for both application designs, despite the recipes (partially) being optimized for opposing goals; minimizing versus maximizing hydrogen content.

To assess the potential performance of Recipe 9, its material properties can be compared to those of the three a-Si:H films investigated by Bruno Buijtendorp [5]. These films were deposited using a PECVD process with fixed deposition parameters except for the substrate temperature, which was varied across 100 °C, 250 °C, and 350 °C. Although the room-temperature material properties of the films showed a monotonic dependence on substrate temperature, no clear correlation was found with the cryogenic microwave loss tangent. All three films exhibited a microwave tan δ below 10^{-5} at 120 mK and 4–7 GHz [8]. In addition, the film deposited at 250 °C showed a mm-submm loss tangent of 2.1×10^{-4} at 350 GHz [35].

When compared to the 250 °C film, Recipe 9 shows improved material properties: a lower void-volume fraction (4.38% vs. 5.5%), a lower microstructure parameter (0.36 vs. 0.48), a higher infrared refractive index (3.289 vs. 3.20), and a lower hydrogen content (11.97% vs. 16.25%). Although Recipe 9 has a higher residual stress (+125 MPa vs. +3 MPa), this value remains relatively modest and is not expected to cause practical issues, especially considering the compressive residual stress of NbTiN, which can provide partial compensation. Altogether, these material properties suggest a lower void density and reduced hydrogen content—both correlated with reduced dielectric loss in the mm-submm range— indicating that Recipe 9 exhibits lower dielectric losses in the filterbank of on-chip spectrometers compared to the film measured in [35].

For the parallel-plate capacitor application, where dielectric losses are reduced by lowering void density and increasing hydrogen content, the comparison is less conclusive. While the lower void density is promising, the reduced hydrogen content may result in fewer passivated dangling bonds, potentially increasing TLS-related losses. Moreover, as noted by Bruno Buijtendorp, no clear correlation was found between room-temperature material properties and cryogenic microwave loss [8], reinforcing the uncertainty regarding the performance of Recipe 9 in PPCs operating in the microwave regime.

6.2. Effectiveness and limitations of the Taguchi optimization

The Taguchi method provided a structured and efficient route to explore a large parameter space with a reduced number of experiments. The orthogonal array of 18 recipes enabled the estimation of main effects across six process parameters with two wafer preparation methods. However, the method comes with important limitations that affected the quality of the optimization.

Firstly, the Taguchi method assumes that the system response is determined by main effects, and

possible interaction effects are not considered. If such interactions are present, they are not captured by the model, which can lead to incorrect optimization outcomes. This is especially relevant when using Main Effect Plots, as they average over all other parameters and therefore cannot reveal whether interactions influence the observed trends.

Secondly, each material property was measured only once per recipe. While this was a practical decision due to limited time during the project, it introduces uncertainty in the response data. Without repeated measurements, the influence of noise cannot be separated from true process variation, and robustness of the recipes cannot be evaluated. For properties such as the void-volume fraction and refractive indices, this is particularly important, as they exhibited high residual contributions in the ANOVA analysis, indicating substantial unexplained variation.

Moreover, the Taguchi method restricts optimization to the predefined levels of each parameter. While this is useful for the first approximation, it limits the resolution of the parameter space. Both optimized recipes are confined to the available discrete settings, with a possibility that better-performing combination may exist between them.

6.3. Predictive power and limitations of the regression model

Regression models were fitted for each material property using a second-order polynomial including linear and squared terms of each parameter, with wafer preparation treated as a categorical variable. These models served two main purposes: to visualize trends across the parameter space and to make predictions for the optimal recipes.

For several properties—such as SSP residual stress and deposition rate—the regression model provided accurate predictions, with low residual contributions and small deviations from the measured values. This supports the validity of the main-effect, second-order model in capturing the underlying trends for these properties.

However, for properties such as void-volume fraction, IR refractive index, and microstructure parameter, the residual contributions were substantial. This indicates that the fitted model fails to fully capture the underlying variation, likely due to unmodeled interaction effects or noise. The model's predictive surface is inherently parabolic and cannot accommodate more complex dependencies. This limitation became evident in the prediction of the hydrogen-rich film (Recipe 20), for which the model significantly overestimated the hydrogen content.

6.4. Measurement uncertainties

Several sources of uncertainty influenced the material property measurements:

The void-volume fraction was determined from a single point at the center of each wafer. This approach was chosen to avoid fitting both the film thickness and the void fraction simultaneously, which would have increased the risk of overfitting. Because the film thickness varies across the wafer, incorporating additional measurement points would have required thickness to be treated as a free parameter. Instead, by fixing all parameters except the void fraction, a consistent one-parameter fit could be performed across all samples. This approach ensured comparability but came at the cost of robustness: the use of a single point makes the extracted void-volume fraction more sensitive to noise. Furthermore, the same Cody–Lorentz shape was used for all films to maintain consistency, though the quality of the fits varied from sample to sample. This introduces additional uncertainty, but avoids model flexibility that could lead to inconsistent interpretations.

A spline baseline correction was applied to the FTIR spectra because the transmission spectra started to deviate from the fitted Transfer Matrix Method (TMM) model, for higher wavenumbers. This deviation limited the fitting range where the TMM could properly be fitted to the data, which increases the uncertainty of the fitted film thickness. This fitted thickness is required to convert the extinction coefficient k(ω) to the absorption coefficient $\alpha(\omega)$, which is then used to determine the hydrogen content and microstructure parameter. As a result, uncertainty in the fitted thickness introduces additional uncertainty in these derived material properties.

The films deposited using Recipes 17 and 19 showed a cloudy surface appearance, as illustrated in

Appendix E. While the physical origin of this effect remains unclear, microscopic inspection revealed a high density of fine surface features. This cloudiness was most pronounced in Recipe 17, but also visibly present in Recipe 19. This similarity is not unexpected, given that the only difference between the two recipes is the reduction of table RF power from 25 W to 0 W. Both films also exhibited outlying refractive index spectra and low band gap values compared to the rest of the dataset (Appendix A). Although the surface appearance was not quantified, its presence may have contributed to deviations in optical measurements such as transmission and ellipsometry through scattering effects.

7

Conclusion

The objective of this research was to optimize the material properties of hydrogenated amorphous silicon (a-Si:H) thin films for use in on-chip spectrometers by adjusting the deposition parameters of an inductively coupled plasma-enhanced chemical vapor deposition (ICP-CVD) process. This goal was addressed by formulating three sub-objectives: (1) relating film properties to their expected dielectric loss performance, (2) establishing the influence of process parameters on those properties, and (3) assigning and testing the recipe with best expected cryogenic performance.

Relate film properties to expected dielectric loss performance
A set of eight material properties was selected for characterization, due to their relevance to dielectric loss mechanisms or their impact on practical film performance, found through literature research. These include residual stress, thickness non-uniformity, void-volume fraction, hydrogen content, microstructure parameter, optical and infrared refractive index, and band gap. Six of these properties are closely linked to dielectric loss mechanisms, particularly two-level systems (TLS) and vibrational absorption. The void-volume fraction, optical and infrared refractive indices, band gap, and microstructure parameter are all indicators of the film's defect density, which are correlated to the TLS density. The hydrogen content affects the vibrational absorption tail in the mm-submm regime and also plays a role in TLS behavior by passivating dangling bonds.

The remaining two properties, residual stress and thickness non-uniformity, are not directly linked to dielectric losses but are critical for assessing the mechanical stability of the films in device applications. High stress may lead to buckling, while non-uniformity decreases the reproducibility of devices across large wafer areas.

Establish the relations between various deposition parameters and the film's properties
The conducted Taguchi orthogonal array, consisting of 18 recipes with orthogonal variations in seven deposition parameters, revealed clear trends in how process conditions influence material properties. Table RF power emerged as the most influential parameter overall, significantly affecting five out of the eight properties. It was the dominant factor in residual stress (explaining >97% of the variation), where higher power levels shifted the film from tensile to strongly compressive stresses. Table RF power also had the highest contribution to the thickness uniformity, optical refractive index, hydrogen content and the microstructure parameter.

Other parameters exerted more moderate effects. Chamber pressure had the strongest influence on the void-volume fraction and infrared refractive index, while silane flow rate and wafer preparation contributed strongest to variations in the band gap. Despite some models exhibiting high residuals, indicating higher order individual effects and possible interactions between the parameters, the overall analysis successfully mapped key relationships between the deposition parameters and the material properties. The measurement ranges observed (e.g., hydrogen content from 6.8–18.9%, void fraction from 4.9–22.3%) indicate the strong tunability of a-Si:H properties within the explored parameter space.

Assign and test the recipe with the best expected cryogenic performance

Two optimized recipes were identified using Grey Relational Analysis, with equal weighting assigned to hydrogen content and void-related properties. Recipe 19 was optimized for minimal hydrogen content, while Recipe 20 targeted maximal hydrogen content. Recipe 19 achieved the highest Grey Relational Grade (GRG = 0.774) and successfully minimized hydrogen content (4.3 at.%), outperforming all other recipes. While it exhibited relatively high void volume fraction and thickness non-uniformity, its low residual stress (–29 MPa) makes it mechanically stable and suitable for reducing dielectric losses due to the vibrational absorption tail in the mm-submm wavelength range.

However, Recipe 19 displayed a cloudy surface, similar to outlier Recipe 17, indicating possible structural inhomogeneity. These surface defects, along with the elevated void density, introduce uncertainty regarding the film's practical applicability in the on-chip spectrometers.

In contrast, Recipe 20 only partially fulfilled its optimization goal. Although it achieved a relatively high hydrogen content (16.3 at.%), it did not outperform several other recipes and achieved a lower GRG (0.640). Nevertheless, the film showed promising indicators of high density, such as the highest optical refractive index (3.42) and a low void-volume fraction (7.6%). However, its high compressive stress (-745 MPa) raises mechanical stability concerns.

Given these limitations, the practical application of both optimal recipes remains uncertain. As a more robust alternative, Recipe 9 emerged as a safer candidate for both applications. It combines a relatively low tensile stress (+125 MPa) with the lowest void-volume fraction in the dataset and performs well across all void-density-related properties. With no visible surface inhomogeneities and lower than average hydrogen content (11.97 at.%), it provides a balanced trade-off between all material properties. Recipe 9 is thus the most viable option for integration in both filterbank and parallel-plate capacitor applications when the practical limitations are to be avoided.

Evaluation of research goal

The research goal—to optimize the dielectric material properties of a-Si:H films by tuning ICP-CVD process parameters—was largely achieved. The work established quantitative relationships between process variables and material characteristics and demonstrated targeted material optimization. The successful identification and validation of Recipe 19 marks a significant achievement, offering a recipe which is expected to contain low dielectric losses in the mm-submm range.

However, Recipe 19 showed surface irregularities and an elevated void fraction, while Recipe 20 exhibited high compressive stress, potentially limiting their suitability for integration into devices. As a more robust alternative, Recipe 9 emerged as the most practically viable option, combining low void content, below-average hydrogen incorporation, and favorable residual stress. When compared to the films characterized by Bruno Buijtendorp [8], Recipe 9 is expected to exhibit lower dielectric losses in the mm–submm wavelength range (350 GHz) than previously reported ($\tan\delta = 2.1 \times 10^{-4}$). For applications in the microwave regime (1–10 GHz), however, the expected performance remains uncertain.

Nonetheless, the study also revealed certain limitations. Some models exhibited high residual errors, suggesting the presence of unmodeled parameter interactions or significant noise contributions. Additionally, while the characterization was performed at room temperature the dielectric loss tangent and TLS density must ultimately be measured under cryogenic conditions to confirm the performance in the low-temperature detector applications.

Despite these limitations, the experimental and analytical framework developed in this work offers a suitable approach to thin-film process optimization. It not only enabled targeted tuning of material properties but also provided insight into practical trade-offs between dielectric performance and mechanical reliability.

8

Recommendations for future work

While this thesis has addressed key aspects of the relationship between deposition parameters and material properties of a-Si:H, several directions remain open for further investigation, particularly with respect to the performance of these films in their intended applications.

The most logical next step is to characterize the dielectric loss of the optimized films, which falls outside the scope of this project. It is recommended to measure the dielectric losses in both the millimeter-submillimeter (mm–submm) regime and the low-power microwave regime, focusing on the two optimal recipes identified in Section 5.4.3. These measurements will verify if the films indeed exhibit low losses in the relevant frequency bands. At the same time, they can provide experimental support for the hypothesized correlations between material properties and dielectric performance. A follow-up master thesis project has been proposed, in which these loss measurements will be performed.

To further interpret the loss data, the measured mm–submm transmission can be fitted using the Maxwell–Helmholtz–Drude (MHD) dispersion model, in combination with the FTIR spectra presented in this thesis. This would construct a dispersion curve, which makes it possible to investigate whether the crossover in the loss origin—suggested by Buijtendorp [5] to occur between the microwave and mm–submm range—is also present in these films.

If the dielectric loss of the current optimal recipes turns out to be too high for integration into the on-chip spectrometer, several options exist to explore alternative recipes. One approach is to adjust the weighting of material properties within the Grey Relational Grade Analysis (GRA). For example, if the two-level systems responsible for dielectric loss are predominantly linked to hydrogen content, the GRA could be redefined to focus solely on maximizing hydrogen content. This would directly target the material characteristic most strongly associated with dielectric loss, potentially leading to a recipe better suited for integration without requiring additional fabrication runs.

Another option is to repeat the orthogonal array presented in this work. Repeating the same Taguchi design would enable separation of variation due to process noise from effects caused by deposition parameter changes, improving the reliability of the estimated trends. By reducing the influence of random variation, the accuracy of the model could be increased, potentially altering the observed trends and, in turn, shifting the predicted optimal recipe. However, this approach would be relatively inefficient given the time and resources required, and the improvement in results may be limited.

Alternatively, the parameter space can be explored more broadly by running a new Taguchi array with different factor levels. This would allow evaluation of recipes further from the original design space. Insights from the regression-based contour plots generated in this work can also be used to manually select new parameter combinations that are predicted to perform well.

More targeted optimization is also possible by varying a single deposition parameter at a time. From the ANOVA analysis, it was found that some parameters—such as table temperature and ICP power—have dominant influence on certain material properties. Adjusting only these dominant parameters across

several new recipes may allow fine-tuning of specific properties without re-running a full design of experiments.

Finally, more advanced experimental designs could be considered. For instance, the Response Surface Methodology (RSM) could be used in future work to reduce the number of required experiments. This is especially relevant as some parameters, such as the gas ratio, showed only minor influence on most material properties in the ANOVA analysis. Reducing the dimensionality of the optimization problem may improve the efficiency of the search for optimal films.

Aside from recipe optimization, further attention could be given to the characterization process itself. For example, the baseline deviation observed in the FTIR spectra remains unexplained and could influence the accuracy of the TMM fitting. Understanding and correcting this deviation would increase confidence in the extracted film thickness and thereby in the derived values for the hydrogen content and microstructure parameter.

In summary, the optimization performed in this thesis forms a strong foundation, but additional experimental work—ranging from dielectric loss measurements to refined process tuning—will be required to fully qualify these films for use in ultra-low-loss on-chip spectrometers.

References

[1] M. Rybak, T. Bakx, J. Baselmans, *et al.*, "Deshima 2.0: Rapid redshift surveys and multi-line spectroscopy of dusty galaxies," en, *J. Low Temp. Phys.*, vol. 209, no. 5-6, pp. 766–778, May 2022.

[2] A. Endo, K. Karatsu, A. P. Laguna, *et al.*, "Wideband on-chip terahertz spectrometer based on a superconducting filterbank," *J. Astron. Telesc. Instrum. Syst.*, vol. 5, no. 03, p. 1, Jun. 2019.

[3] A. Taniguchi, T. J. L. C. Bakx, J. J. A. Baselmans, *et al.*, "DESHIMA 2.0: Development of an integrated superconducting spectrometer for science-grade astronomical observations," en, *J. Low Temp. Phys.*, vol. 209, no. 3-4, pp. 278–286, Nov. 2022.

[4] A. Patel, A. Brown, W. Hsieh, *et al.*, "Fabrication of MKIDS for the MicroSpec spectrometer," *IEEE Trans. Appl. Supercond.*, vol. 23, no. 3, pp. 2 400 404–2 400 404, Jun. 2013.

[5] B. T. Buijtendorp, "Low-loss deposited dielectrics for superconducting integrated circuits," Available via TU Delft Repository, PhD thesis, Delft University of Technology, 2025. DOI: 10.4233/uuid:50173f5f-cf91-4353-b4a7-2c681fc898d8.

[6] A. Pascual Laguna, K. Karatsu, D. Thoen, *et al.*, "Terahertz band-pass filters for wideband superconducting on-chip filter-bank spectrometers," *IEEE Trans. Terahertz Sci. Technol.*, vol. 11, no. 6, pp. 635–646, Nov. 2021.

[7] D. J. Thoen, V. Murugesan, A. Pascual Laguna, K. Karatsu, A. Endo, and J. J. A. Baselmans, "Combined ultraviolet- and electron-beam lithography with Micro-Resist-Technology GmbH ma-n1400 resist," en, *J. Vac. Sci. Technol. B Nanotechnol. Microelectron.*, vol. 40, no. 5, p. 052 603, Sep. 2022.

[8] B. T. Buijtendorp, J. Bueno, D. J. Thoen, *et al.*, "Characterization of low-loss hydrogenated amorphous silicon films for superconducting resonators," *J. Astron. Telesc. Instrum. Syst.*, vol. 8, no. 02, Jun. 2022.

[9] K. Kouwenhoven, G. P. J. van Doorn, B. T. Buijtendorp, *et al.*, "Geometry dependence of two-level-system noise and loss in a - SiC : H parallel-plate capacitors for superconducting microwave resonators," en, *Phys. Rev. Appl.*, vol. 21, no. 4, Apr. 2024.

[10] A. Mavropoulou, S. O. Dabironezare, J. Baselmans, and A. Endo, "On the design of wide band multi-lens focal plane arrays for the TIFUUN instrument," in *2023 48th International Conference on Infrared, Millimeter, and Terahertz Waves (IRMMW-THz)*, Montreal, QC, Canada: IEEE, Sep. 2023, pp. 1–2.

[11] K. Kohno, A. Endo, Y. Tamura, *et al.*, "Sub/millimeter-wave dual-band line intensity mapping using the terahertz integral field units with universal nanotechnology (TIFUUN) for the atacama submillimeter telescope experiment (ASTE)," in *Millimeter, Submillimeter, and Far-Infrared Detectors and Instrumentation for Astronomy XII*, J. Zmuidzinas and J.-R. Gao, Eds., Yokohama, Japan: SPIE, Aug. 2024, p. 14.

[12] European Southern Observatory (ESO), *Integral field units*, https://www.eso.org/public/teles-instr/technology/ifu/, Accessed: Jul. 14, 2025, 2025.

[13] S. de Boer, "Compact mkids miniaturization of microwave kinetic inductace detectors," Master's thesis, Delft University of Technology, Delft, The Netherlands, 2022.

[14] M. Roesch, A. Benoit, A. Bideaud, *et al.*, "Development of lumped element kinetic inductance detectors for NIKA," 2012. eprint: 1212.4585 (astro-ph.IM).

[15] S. Beldi, F. Boussaha, J. Hu, *et al.*, "High Q-factor near infrared and visible Al $_2$ O $_3$ -based parallel-plate capacitor kinetic inductance detectors," *Optics Express*, vol. 27, no. 9, p. 13 319, Apr. 2019, ISSN: 1094-4087. DOI: 10.1364/OE.27.013319. (visited on 10/02/2024).

[16] Y. Hamedani, P. Macha, T. J. Bunning, R. R. Naik, and M. C. Vasudev, "Plasma-Enhanced Chemical Vapor Deposition: Where we are and the Outlook for the Future," in *Chemical Vapor Deposition - Recent Advances and Applications in Optical, Solar Cells and Solid State Devices*, S. Neralla, Ed., InTech, Aug. 2016, ISBN: 978-953-51-2572-3 978-953-51-2573-0. DOI: 10.5772/64654.

[17] T. Frischmuth, M. Schneider, D. Maurer, T. Grille, and U. Schmid, "Inductively-coupled plasma-enhanced chemical vapour deposition of hydrogenated amorphous silicon carbide thin films for MEMS," en, *Sens. Actuators A Phys.*, vol. 247, pp. 647–655, Aug. 2016.

[18] B. T. Buijtendorp, S. Vollebregt, K. Karatsu, *et al.*, "Hydrogenated amorphous silicon carbide: A low-loss deposited dielectric for microwave to submillimeter-wave superconducting circuits," en, *Phys. Rev. Appl.*, vol. 18, no. 6, Dec. 2022.

[19] K. Kouwenhoven, D. Fan, E. Biancalani, *et al.*, "Resolving power of visible-to-near-infrared hybrid βTa/NbTiN kinetic inductance detectors," en, *Phys. Rev. Appl.*, vol. 19, no. 3, Mar. 2023.

[20] F. Defrance, A. D. Beyer, S. Shu, J. Sayers, and S. R. Golwala, "Characterization of the low electric field and zero-temperature two-level-system loss in hydrogenated amorphous silicon," en, *Phys. Rev. Mater.*, vol. 8, no. 3, Mar. 2024.

[21] Oxford Instruments Plasma Technology, *Plasmapro®100 icpcvd operator manual*, Oxford Instruments Nanotechnology Tools Ltd., Nov. 2021.

[22] Oxford Instruments. "Inductively coupled plasma chemical vapor deposition (icpcvd)." Accessed: 2025-07-05. (2025), [Online]. Available: https://plasma.oxinst.com/technology/icpcvd.

[23] E. Johlin, N. Tabet, S. Castro-Galnares, *et al.*, "Structural origins of intrinsic stress in amorphous silicon thin films," *Phys. Rev. B Condens. Matter Mater. Phys.*, vol. 85, no. 7, Feb. 2012.

[24] N. Sharma, M. Hooda, and S. K. Sharma, "Stresses in thin films: An experimental study," en, *Indian J. Phys. Proc. Indian Assoc. Cultiv. Sci. (2004)*, vol. 93, no. 2, pp. 159–167, Feb. 2019.

[25] M. R. Ardigo, M. Ahmed, and A. Besnard, "Stoney formula: Investigation of curvature measurements by optical profilometer," *Adv. Mat. Res.*, vol. 996, pp. 361–366, Aug. 2014.

[26] F. Vaz, "Residual stress states in sputtered Ti1âxSixNy films," *Thin Solid Films*, vol. 402, no. 1-2, pp. 195–202, Jan. 2002.

[27] M. R. Linford, H. G. Tompkins, and J. N. Hilfiker, "A review of tompkins' and hilfiker's book entitled: *Spectroscopic Ellipsometry: Practical Application to Thin Film Characterization*," *Vacuum Technology & Coating*, vol. 19, no. 7, pp. 1–7, Jul. 2018. [Online]. Available: https://www.researchgate.net/publication/325882489.

[28] J. A. Woollam Co., Inc., *Completeease data analysis manual*, Version 4.63, Lincoln, NE, USA: J. A. Woollam Co., Inc., Oct. 2011.

[29] G. E. Jellison Jr and F. A. Modine, "Parameterization of the optical functions of amorphous materials in the interband region," en, *Appl. Phys. Lett.*, vol. 69, no. 3, pp. 371–373, Jul. 1996.

[30] H. Fujiwara and R. W. Collins, Eds., *Spectroscopic ellipsometry for photovoltaics* (SPringer series in optical sciences), en, 2018th ed. Cham, Switzerland: Springer International Publishing, Jan. 2019.

[31] A. S. Ferlauto, G. M. Ferreira, J. M. Pearce, *et al.*, "Analytical model for the optical functions of amorphous semiconductors from the near-infrared to ultraviolet: Applications in thin film photovoltaics," en, *J. Appl. Phys.*, vol. 92, no. 5, pp. 2424–2436, Sep. 2002.

[32] G. A. Niklasson, C. G. Granqvist, and O. Hunderi, "Effective medium models for the optical properties of inhomogeneous materials," en, *Appl. Opt.*, vol. 20, no. 1, pp. 26–30, Jan. 1981.

[33] Daey Ouwens J and R. E. Schropp, "Hydrogen microstructure in hydrogenated amorphous silicon," en, *Phys. Rev. B Condens. Matter*, vol. 54, no. 24, pp. 17 759–17 762, Dec. 1996.

[34] W. A. Phillips, "Tunneling states in amorphous solids," en, *J. Low Temp. Phys.*, vol. 7, no. 3-4, pp. 351–360, May 1972.

[35] S. Hähnle, K. Kouwenhoven, B. Buijtendorp, *et al.*, "Superconducting microstrip losses at microwave and submillimeter wavelengths," en, *Phys. Rev. Appl.*, vol. 16, no. 1, Jul. 2021.

[36] A. D. O'Connell, M. Ansmann, R. C. Bialczak, *et al.*, "Microwave dielectric loss at single photon energies and millikelvin temperatures," en, *Appl. Phys. Lett.*, vol. 92, no. 11, p. 112 903, Mar. 2008.

[37] A. A. Langford, M. L. Fleet, B. P. Nelson, W. A. Lanford, and N. Maley, "Infrared absorption strength and hydrogen content of hydrogenated amorphous silicon," en, *Phys. Rev. B Condens. Matter*, vol. 45, no. 23, pp. 13 367–13 377, Jun. 1992.

[38] B. A. Mazin, D. Sank, S. McHugh, *et al.*, "Thin film dielectric microstrip kinetic inductance detectors," en, *Appl. Phys. Lett.*, vol. 96, no. 10, p. 102 504, Mar. 2010.

[39] J. Gao, M. Daal, J. M. Martinis, *et al.*, "A semiempirical model for two-level system noise in superconducting microresonators," en, *Appl. Phys. Lett.*, vol. 92, no. 21, p. 212 504, May 2008.

[40] C. Müller, J. H. Cole, and J. Lisenfeld, "Towards understanding two-level-systems in amorphous solids: Insights from quantum circuits," en, *Rep. Prog. Phys.*, vol. 82, no. 12, p. 124 501, Dec. 2019.

[41] D. R. Queen, X. Liu, J. Karel, H. C. Jacks, T. H. Metcalf, and F. Hellman, "Two-level systems in evaporated amorphous silicon," en, *J. Non Cryst. Solids*, vol. 426, pp. 19–24, Oct. 2015.

[42] H. C. Jacks, "Identifying structures responsible for two-level systems in amorphous silicon," Advised by Frances Hellman, Ph.D. dissertation, University of California, Berkeley, Spring 2018.

[43] M. Molina-Ruiz, Y. J. Rosen, H. C. Jacks, *et al.*, "Origin of mechanical and dielectric losses from two-level systems in amorphous silicon," en, *Phys. Rev. Mater.*, vol. 5, no. 3, Mar. 2021.

[44] R. K. Roy, *A Primer on the Taguchi Method*, 2nd ed. Dearborn, MI: Society of Manufacturing Engineers, 2010, ISBN: 9780872638622.

[45] R. Unal and E. B. Dean, "Taguchi approach to design optimization for quality and cost: An overview," in *Proceedings of the Annual Conference of the International Society of Parametric Analysts*, International Society of Parametric Analysts, Washington, D.C., 1991.

[46] S. Banerjee, "Super-growth of cnts based on zrn for tsv application," MSc Thesis, Delft University of Technology, Delft, The Netherlands, 2014.

[47] A. Mitra, "The taguchi method," en, *Wiley Interdiscip. Rev. Comput. Stat.*, vol. 3, no. 5, pp. 472–480, Sep. 2011.

[48] C. L. Lin, "Use of the taguchi method and grey relational analysis to optimize turning operations with multiple performance characteristics," *Mater. Manuf. Process.*, vol. 19, no. 2, pp. 209–220, Dec. 2004.

[49] E. Kuram and B. Ozcelik, "Multi-objective optimization using taguchi based grey relational analysis for micro-milling of al 7075 material with ball nose end mill," en, *Measurement (Lond.)*, vol. 46, no. 6, pp. 1849–1864, Jul. 2013.

[50] J. L. Lin and C. L. Lin, "The use of the orthogonal array with grey relational analysis to optimize the electrical discharge machining process with multiple performance characteristics," en, *Int. J. Mach. Tools Manuf.*, vol. 42, no. 2, pp. 237–244, Jan. 2002.

[51] W. Lin, S. Ma, and C.-C. J. Kuo, "Application of grey-relational analysis to find the most suitable watermarking scheme," in *Proceedings of the 2002 IEEE International Conference on Multimedia and Expo (ICME)*, IEEE, 2002, pp. 333–336. DOI: 10.1109/ICME.2002.1035944.

[52] M. Zawierta, M. Martyniuk, R. D. Jeffery, *et al.*, "A high deposition rate amorphous-silicon process for use as a thick sacrificial layer in surface-micromachining," *J. Microelectromech. Syst.*, vol. 26, no. 2, pp. 406–414, Apr. 2017.

[53] C. B. Singh, S. Bhattacharya, S. Prayogi, U. S. Patel, P. B. Bhargav, and N. Ahmed, "A new look at an explanation of band gap of PECVD grown a-Si:H thin films using absorption spectra, spectroscopic ellipsometry, raman, and FTIR spectrosopy," en, *Opt. Mater. (Amst.)*, vol. 154, no. 115809, p. 115 809, Aug. 2024.

[54] J. W. Lee, K. D. Mackenzie, D. Johnson, J. N. Sasserath, S. J. Pearton, and F. Ren, "Low temperature silicon nitride and silicon dioxide film processing by inductively coupled plasma chemical vapor deposition," en, *J. Electrochem. Soc.*, vol. 147, no. 4, p. 1481, 2000.

[55] D. K. Tripathi, F. Jiang, M. Martyniuk, *et al.*, "Optimization of ICPCVD amorphous silicon for optical MEMS applications," *J. Microelectromech. Syst.*, vol. 24, no. 6, pp. 1998–2007, Dec. 2015.

[56] D. K. Tripathi, H. Mao, K. K. M. B. D. Silva, and L. Faraone, "Compositional and mechanical properties of PECVD silicon for thin-film optical applications," in *COMMAD 2012*, Melbourne, Australia: IEEE, Dec. 2012.

[57] D. C. Montgomery, *Design and Analysis of Experiments*, 8th. Hoboken, NJ: John Wiley & Sons, Inc., 2013, ISBN: 978-1-118-14692-7.

[58] G. Chen, E. J. H. Cheung, Y. Cao, J. Pan, and A. J. Danner, "Analysis of perovskite oxide etching using argon inductively coupled plasmas for photonics applications," en, *Nanoscale Res. Lett.*, vol. 16, no. 1, p. 32, Feb. 2021.

[59] A. H. M. Smets, W. M. M. Kessels, and M. C. M. van de Sanden, "Vacancies and voids in hydrogenated amorphous silicon," en, *Appl. Phys. Lett.*, vol. 82, no. 10, pp. 1547–1549, Mar. 2003.

[60] S. H. Lin, Y. C. Chan, D. P. Webb, and Y. W. Lam, "Optical characterization of hydrogenated amorphous silicon thin films deposited at high rate," en, *J. Electron. Mater.*, vol. 28, no. 12, pp. 1452–1456, Dec. 1999.

[61] G. Zalczer and V. Gurfein, "Spectroscopic ellipsometry near the brewster angle on transparent substrates," en, *Rev. Sci. Instrum.*, vol. 63, no. 4, pp. 2132–2134, Apr. 1992.

[62] A. Richter, J. Benick, and S. W. Glunz, "Spectral ellipsometry analysis of ultrathin amorphous silicon layers," in *Proceedings of the 23rd European Photovoltaic Solar Energy Conference and Exhibition*, Conference Paper, Valencia, Spain: WIP-Renewable Energies, Sep. 2008. [Online]. Available: https://www.researchgate.net/publication/234125541.

[63] A. Tarifa and N. M. Ravindra, "Optical properties of crystalline silicon in the infrared," en, in *The Minerals, Metals & Materials Series*, ser. The minerals, metals & materials series, Cham: Springer Nature Switzerland, 2023, pp. 364–382.

[64] G. Lucovsky, R. J. Nemanich, and J. C. Knights, "Structural interpretation of the vibrational spectra ofa-si: H alloys," *Phys. Rev. B Condens. Matter*, vol. 19, no. 4, pp. 2064–2073, Feb. 1979.

A

Overview general results

This appendix contains the results of the non-uniformity measurements, including front-side thickness variation and radial curvature. It also includes the complex refractive index curves obtained from spectroscopic ellipsometry, and the transmission spectra measured by FTIR. Finally, the Kramers-Kronig consistent $k(\omega)$ and $n(\omega)$ curves obtained with the FTIR are presented. These results provide additional insight into the uniformity and optical properties of the deposited a-Si:H layers.

A.1. Deposition non-uniformity

From the front-side view shown in Figure A.1, the thickness non-uniformity is observed to be radially symmetric, with the thickness decreasing from the center toward the edge of the wafer. This same trend is visible in the radial thickness curves of all 18 recipes, shown in Figure A.2, where each curve exhibits a downward slope from the center to the edge.

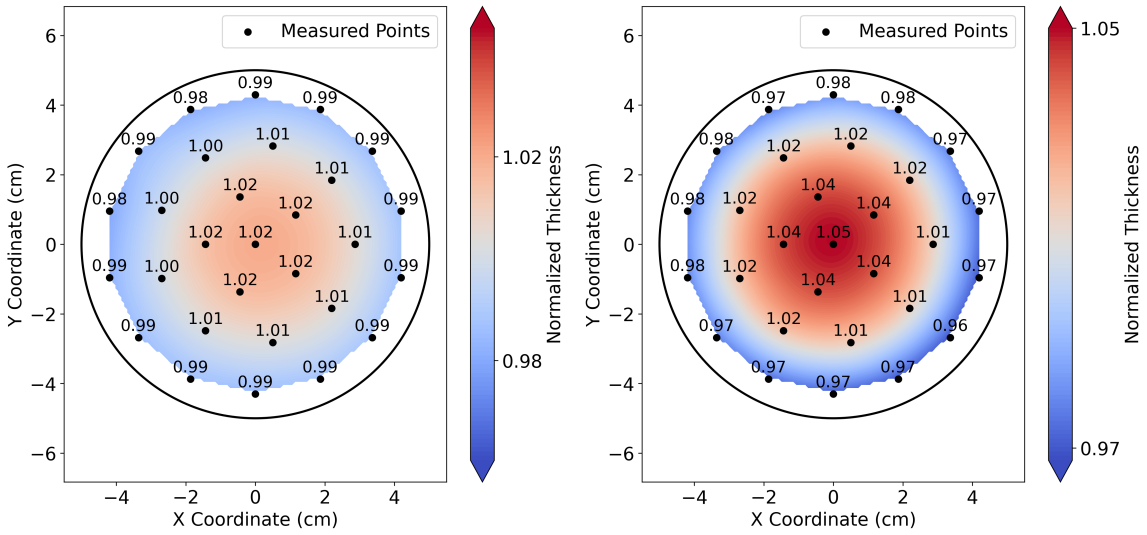

Figure A.1: Radially averaged, normalized thickness maps of the wafers with the lowest (left, recipe 4) and highest (right, recipe 2) non-uniformity among all tested recipes. Black dots indicate ellipsometry measurement locations.

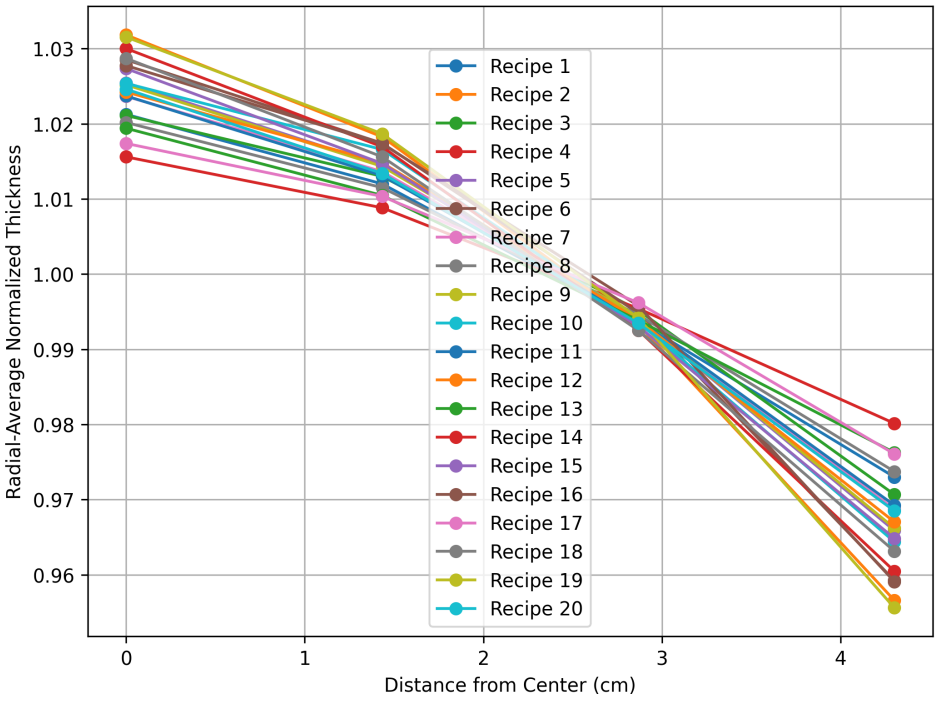

Figure A.2: Radial non-uniformity of film thickness for 18 deposition recipes, normalized to the radial average. Also included are the two additional recipes conducted after the Grey Relational Analysis: Recipe 19 (optimized for minimum hydrogen content) and Recipe 20 (optimized for maximum hydrogen content). Each curve shows the thickness as a function of distance from the center, revealing a consistent decrease in thickness toward the wafer edge across all recipes.

Below are the front-side view of the non-uniformity plots of the recipes conducted after the Grey Relational Analysis. The thickness non-uniformity is observed to be radially symmetric, with the thickness decreasing from the center toward the edge of the wafer. This same trend is visible for all recipes performed earlier.

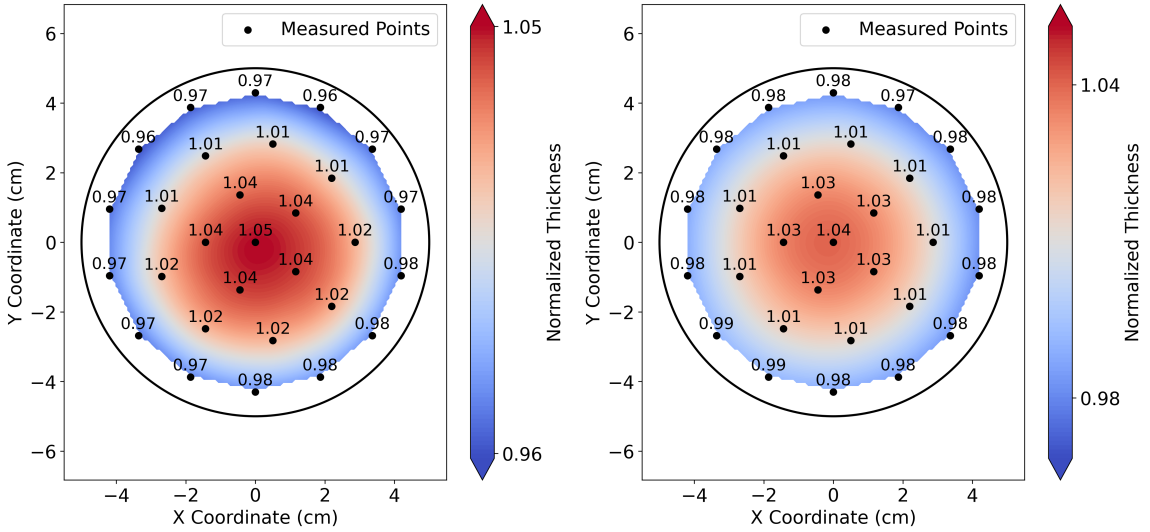

Figure A.3: Radially averaged, normalized thickness maps of the wafers with minimizing the hydrogen content (left) and maximizing the hydrogen content (right) non-uniformity. Black dots indicate ellipsometry measurement locations.

A.2. Complex refractive index from ellipsometry

The figure below shows the refractive index n (solid lines) and extinction coefficient k (dashed lines) as a function of wavelength for all 18 a-Si:H deposition recipes, and the two recipes conducted after the Grey Relational analysis. These values were extracted by fitting a Tauc-Lorentz dispersion model to the ellipsometry measurements. This plot illustrates the variation in optical constants between recipes and shows recipe 17 and the recipe designed to minimize the hydrogen content, exhibits a significantly different complex refractive index.

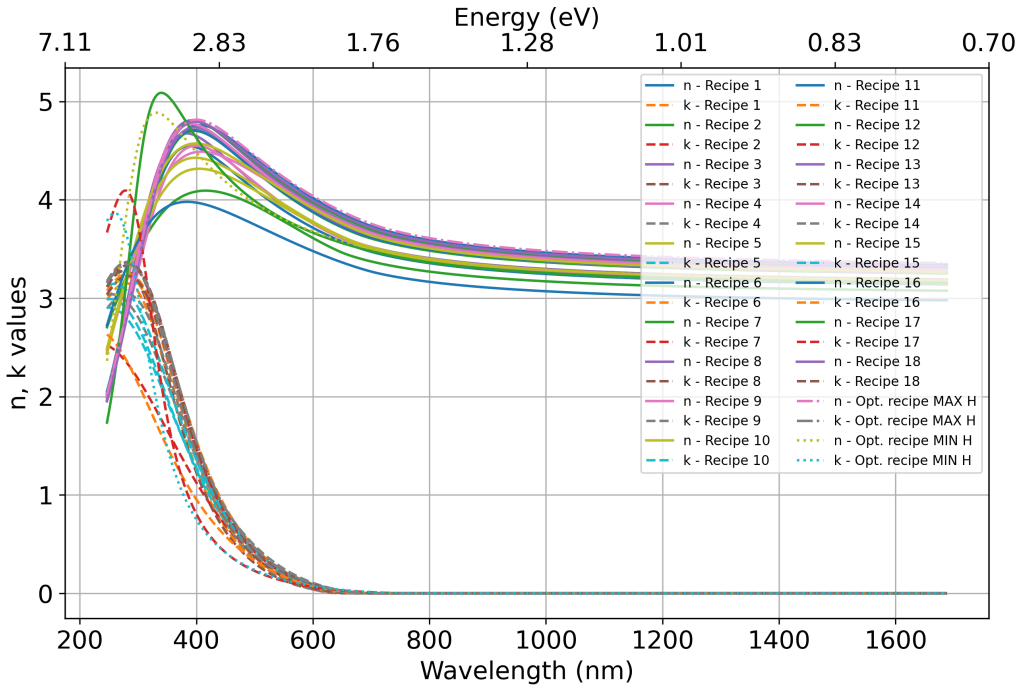

Figure A.4: Refractive index n (solid lines) and extinction coefficient k (dashed lines) as a function of wavelength for 18 different a-Si:H deposition recipes, measured using spectroscopic ellipsometry. Additionally, the two recipes conducted after the Grey Relational Analysis are shown.

A.3. Transmission spectra from FTIR

The figure below shows the FTIR transmission spectra of all 18 samples (film deposited on substrate) in the Taguchi matrix, including the reference spectrum of the bare double-side polished c-Si substrate. The absorption dips relevant for the analysis are observed near 640 cm^{-1} and in the region of 2000–2200 cm^{-1}. Interference fringes are visible across the spectrum and result from multiple internal reflections within the a-Si:H layer. These fringes carry information about the film thickness. The Transfer Matrix Method (TMM) was applied to these spectra to simultaneously extract the complex refractive index and thickness of each film.

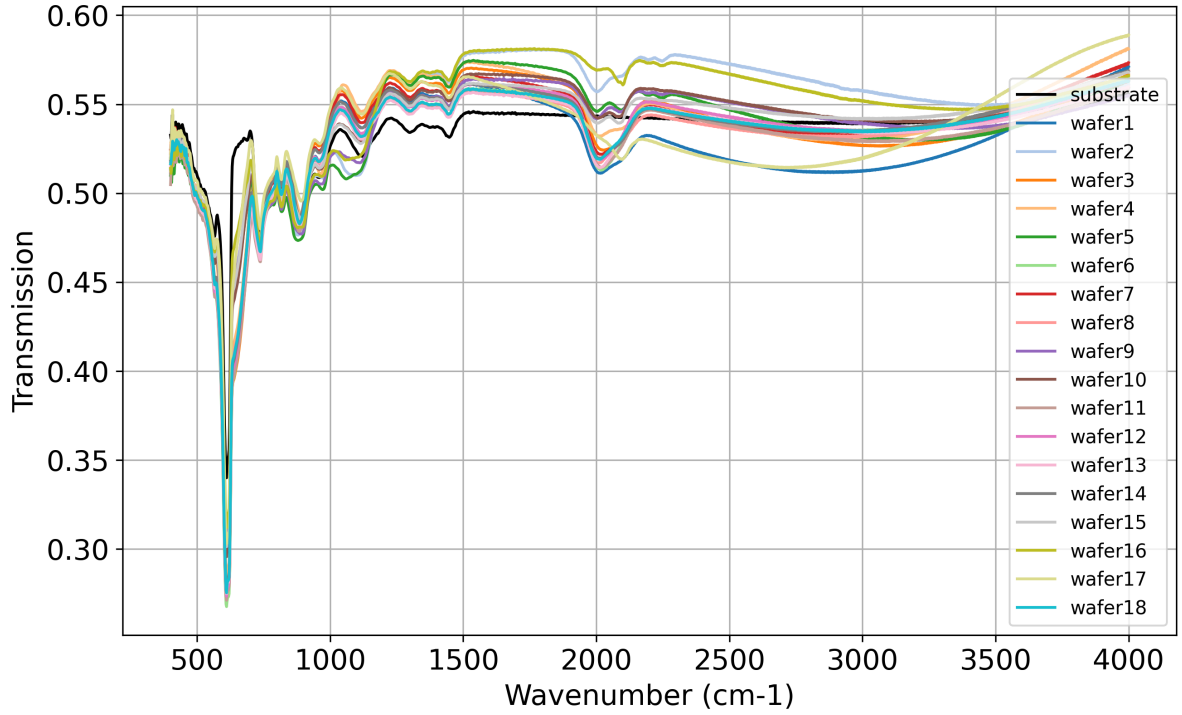

Figure A.5: FTIR transmission spectra of all 18 a-Si:H samples, measured on double-side polished c-Si substrates. The black curve shows the transmission of the bare substrate. Spectral features around 640 cm^{-1} and 2000–2200 cm^{-1} correspond to characteristic absorption bands of a-Si:H.

A.4. Kramers-Kronig consistent $k(\omega)$ and $n(\omega)$ curves

Below the Kramers-Kronig consistent $k(\omega)$ and $n(\omega)$ curves of both recipes conducted after the Grey Relational Analysis are shown.

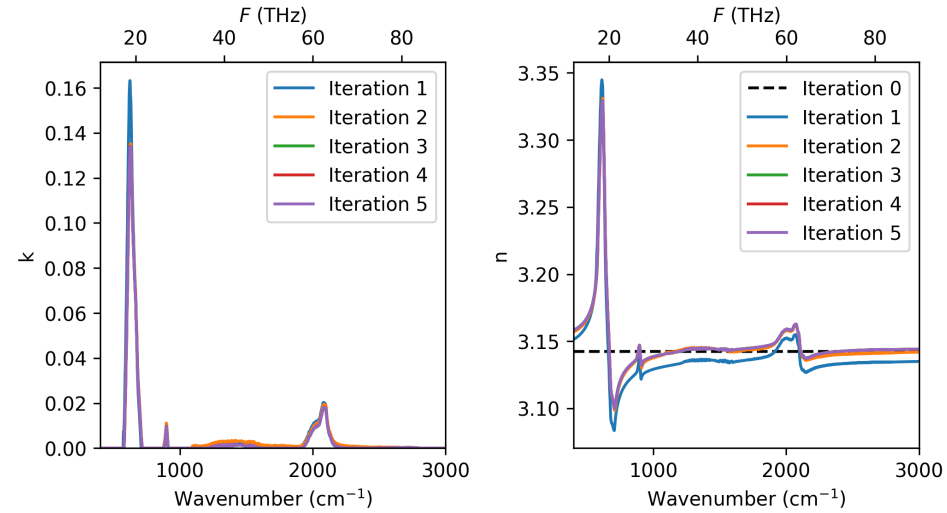

(a)

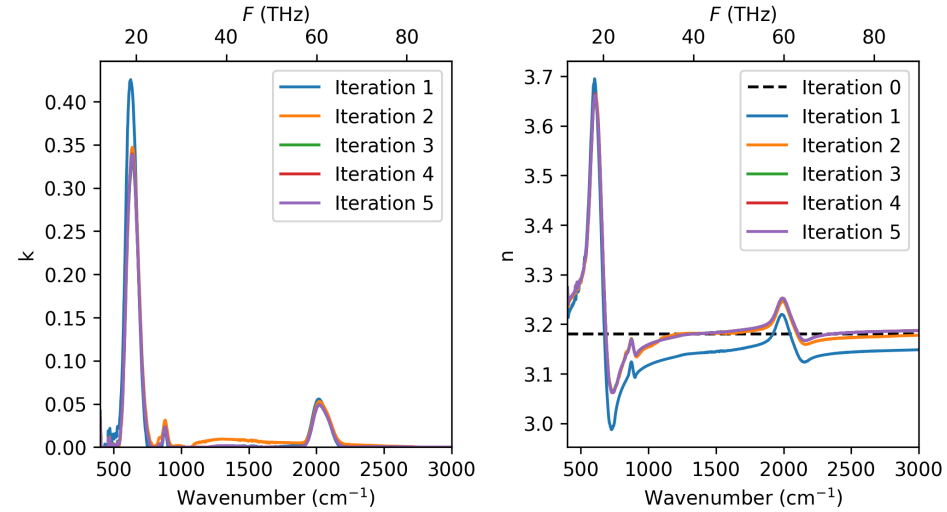

(b)

Figure A.6: Kramers-Kronig consistent $k(\omega)$ and $n(\omega)$ curves of both recipes conducted after the Grey Relational Grade for two design targets: (a) minimizing hydrogen content and (b) maximizing hydrogen content.

B

Contour plots from regression model

This appendix presents the contour plots generated from the regression models described in Section 5.2. For each material property, the predicted values are visualized in the parameter space surrounding the optimal recipe identified in Section 5.3, offering insight beyond the discrete levels defined in the Taguchi design. Similarly, contour plots are shown for the two optimal recipes identified through Grey Relational Analysis in Section 5.4, which correspond to the two application targets: the parallel-plate capacitors (PPCs) used in KIDs, and the microstrip lines constructing the filterbank.

These plots should be interpreted with caution. The regression models include only the main effects—linear and quadratic terms—without interaction terms. As a result, the predicted surfaces shown in the contour plots follow simplified parabolic shapes. While they provide qualitative insight into the parameter space, the actual response surfaces may exhibit additional complexity not captured by the model.

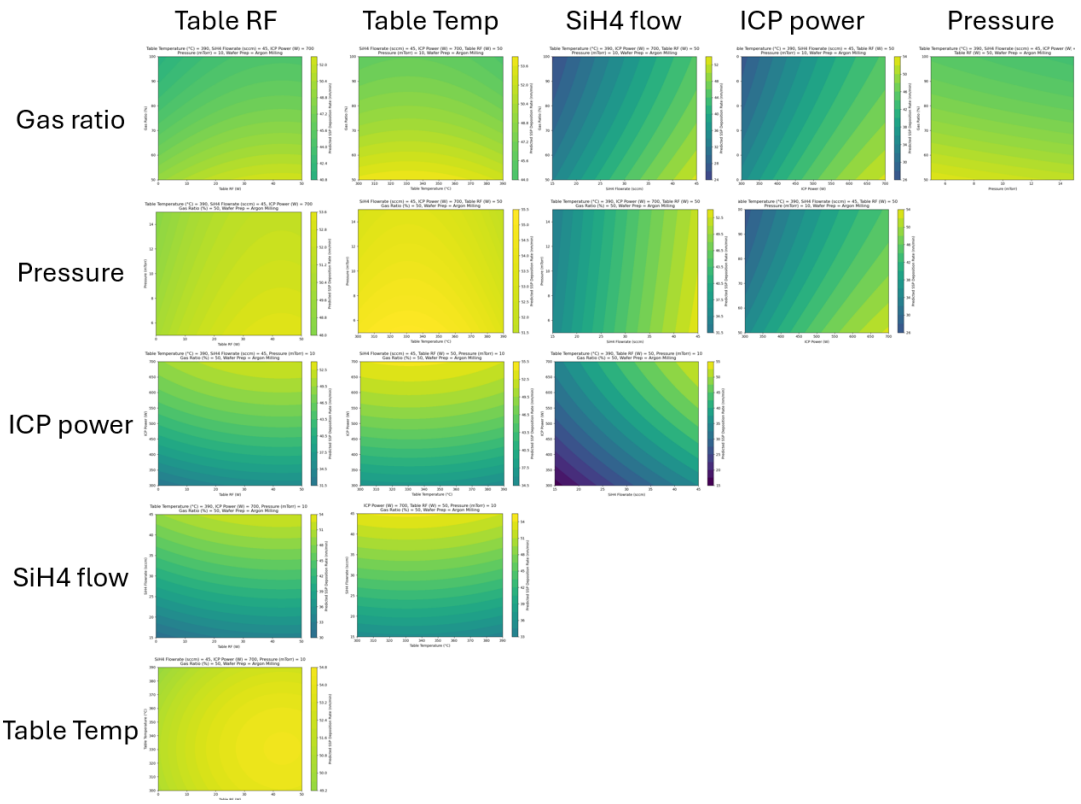

Figure B.1: Contour plots of the deposition rate, with brighter colors indicating higher deposition rates. Deposition parameter levels increase from left to right and from bottom to top.

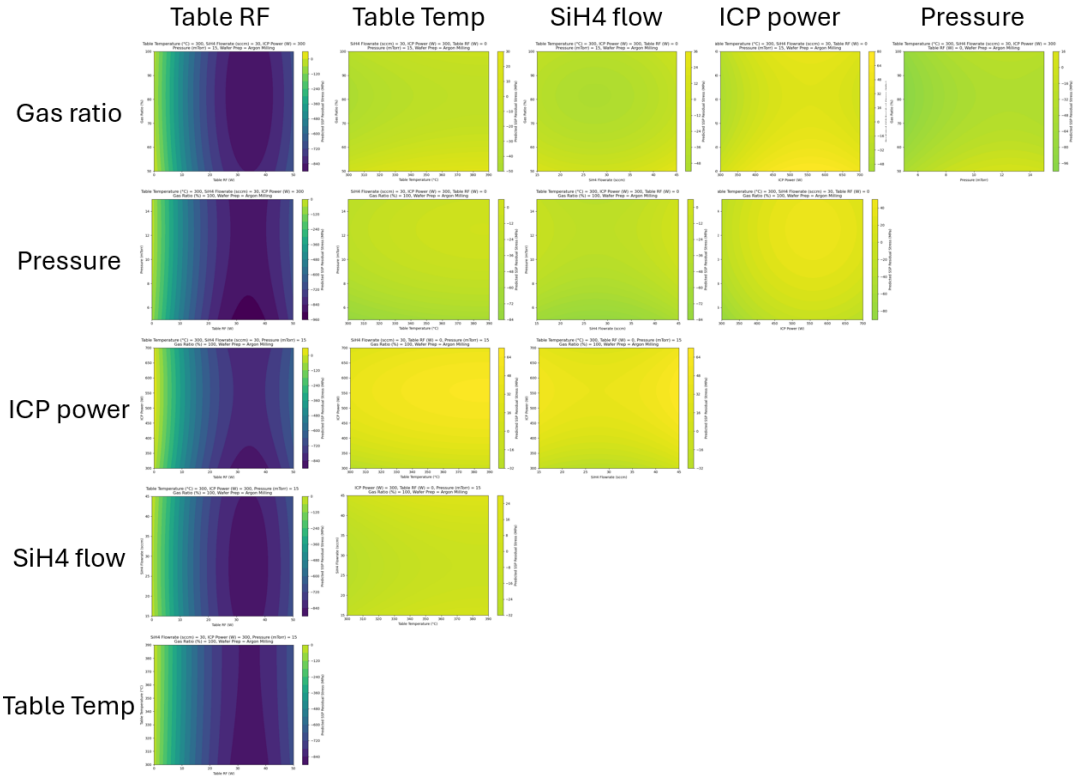

Figure B.2: Contour plots of the SSP residual stress, with brighter colors indicating more positive stresses. Deposition parameter levels increase from left to right and from bottom to top.

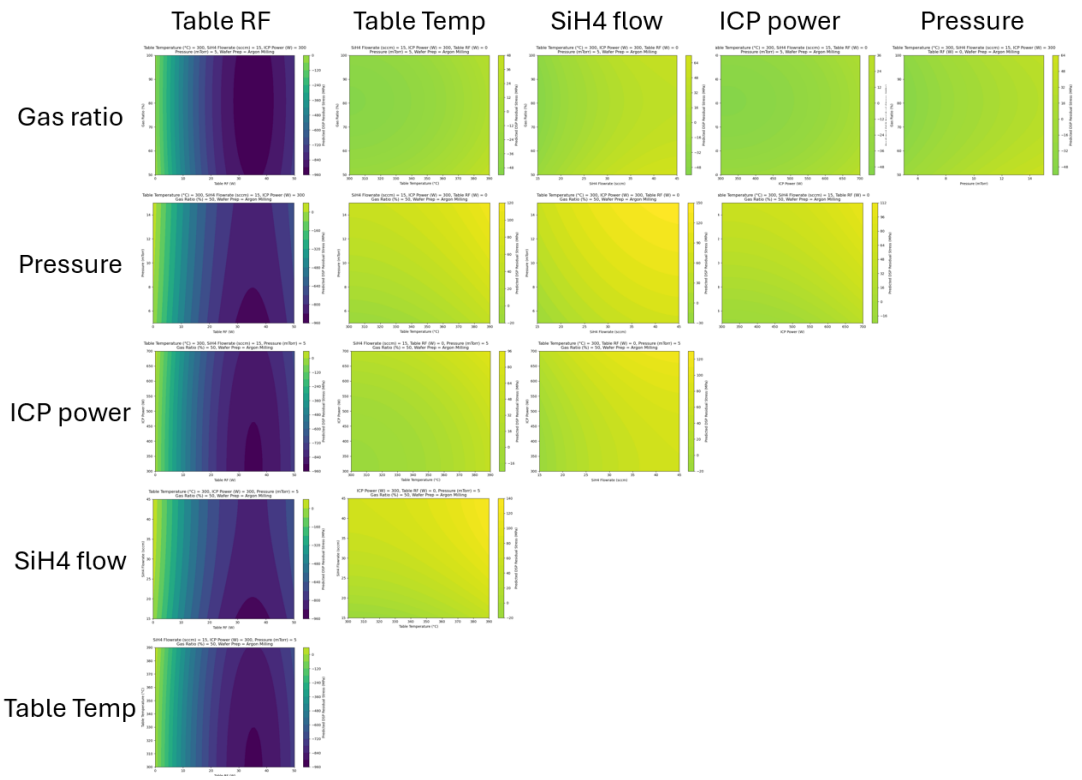

Figure B.3: Contour plots of the DSP residual stress, with brighter colors indicating more positive stresses. Deposition parameter levels increase from left to right and from bottom to top.

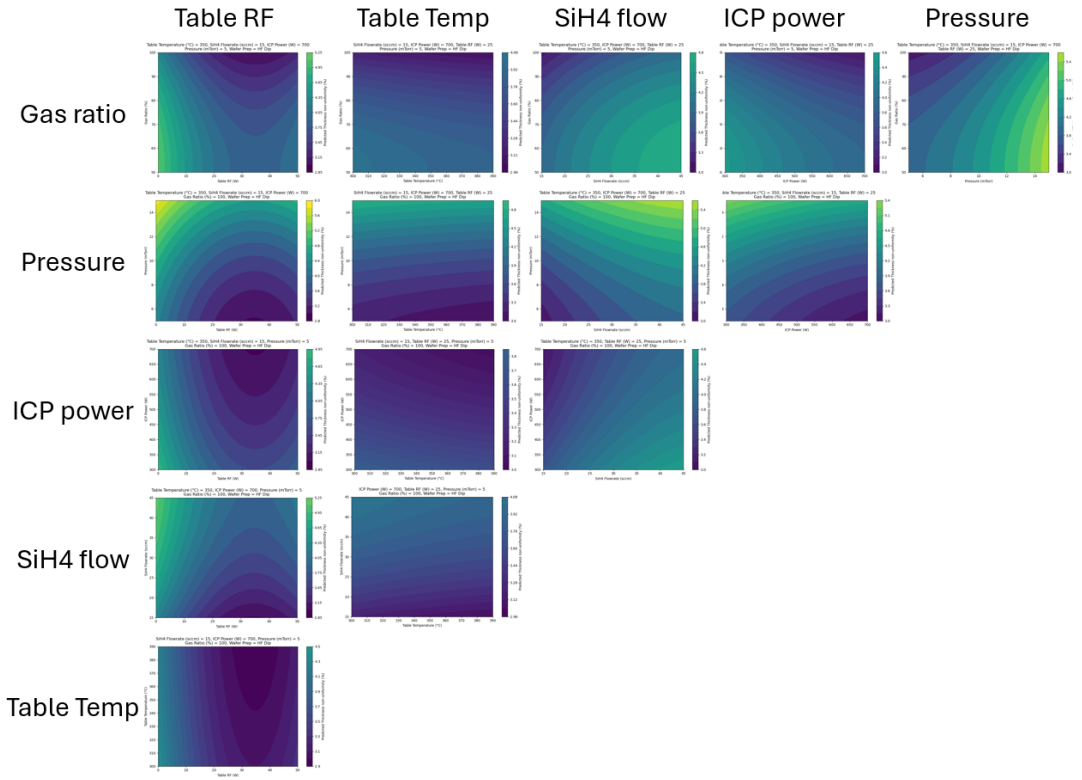

Figure B.4: Contour plots of the thickness non-uniformity, with brighter colors indicating higher non-uniformities. Deposition parameter levels increase from left to right and from bottom to top.

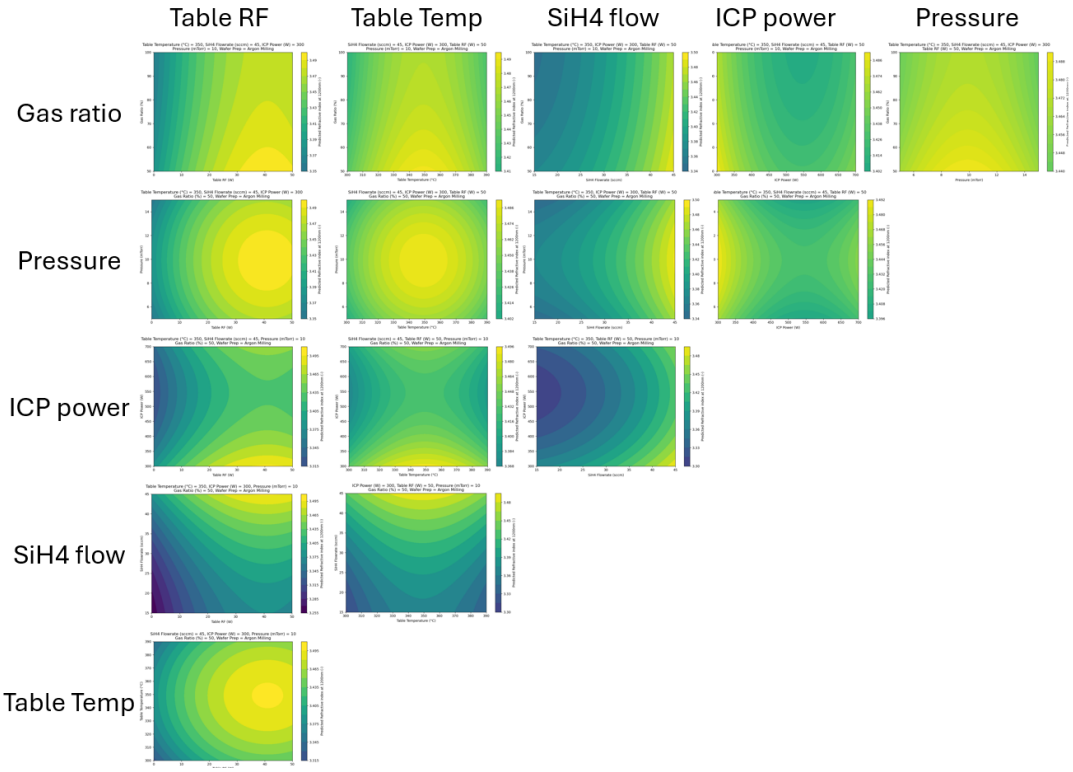

Figure B.5: Contour plots of the optical refractive index, with brighter colors indicating higher indices. Deposition parameter levels increase from left to right and from bottom to top.

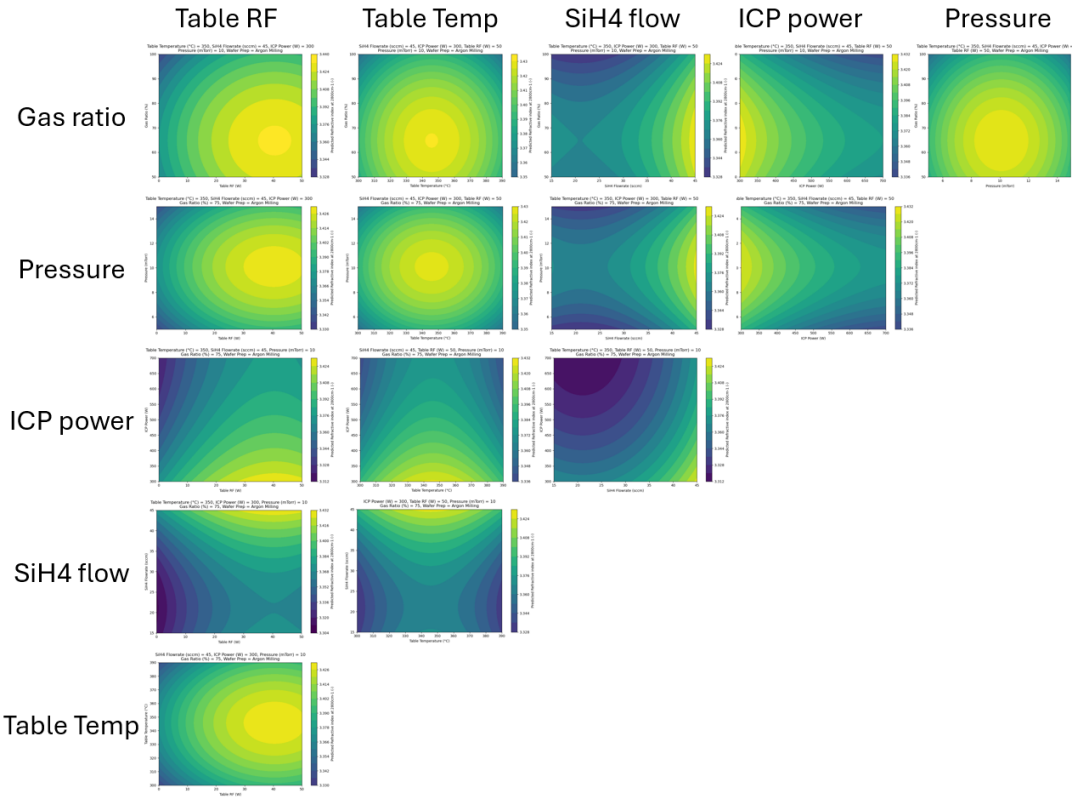

Figure B.6: Contour plots of the infrared refractive index, with brighter colors indicating higher indices. Deposition parameter levels increase from left to right and from bottom to top.

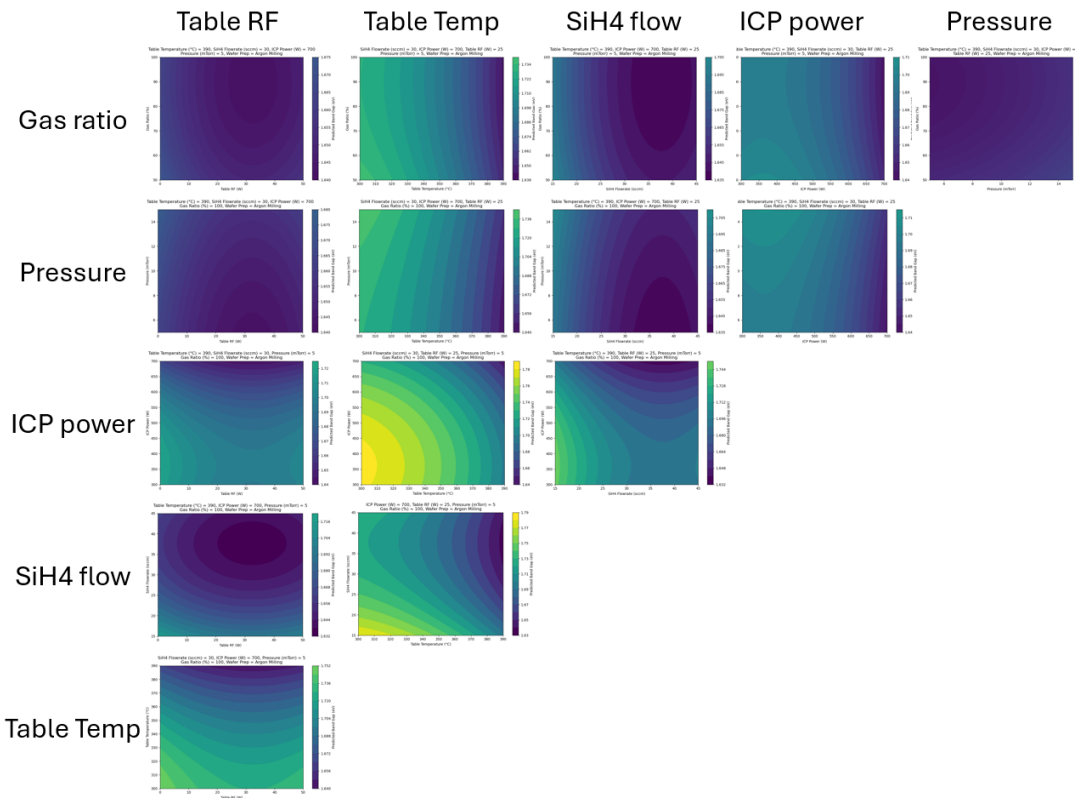

Figure B.7: Contour plots of band gap, with brighter colors indicating higher band gaps. Deposition parameter levels increase from left to right and from bottom to top.

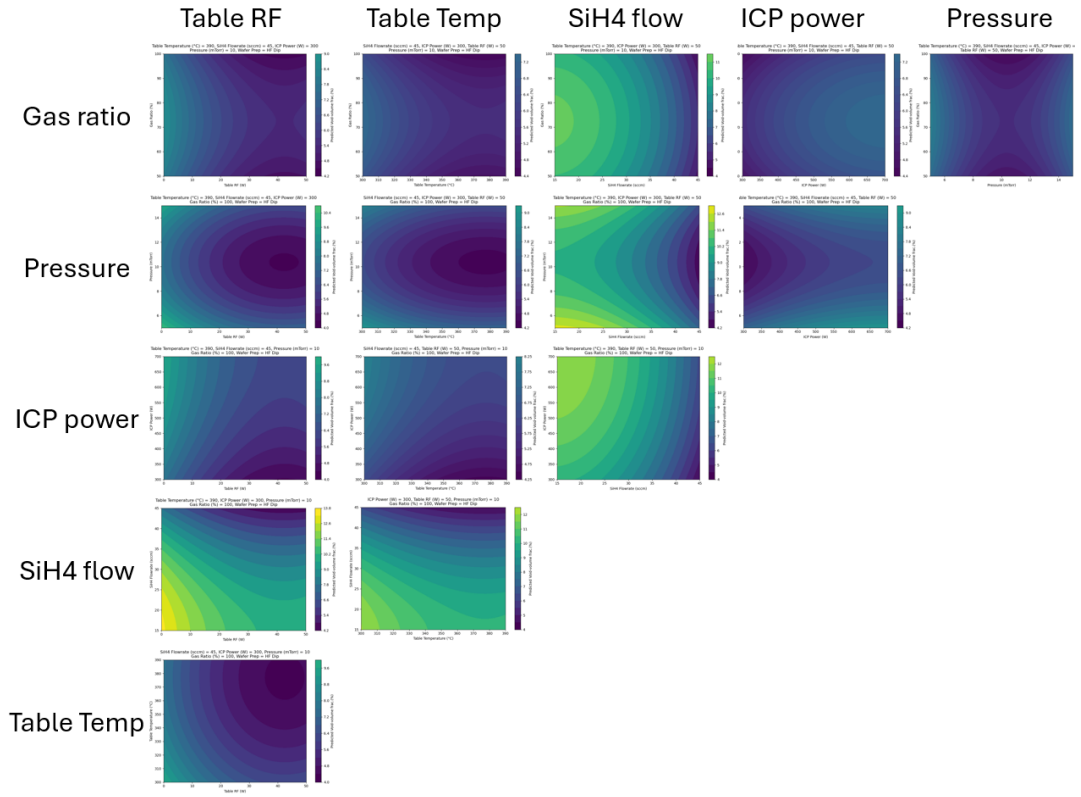

Figure B.8: Contour plots of the void-volume fraction, with brighter colors indicating higher void-volume fraction. Deposition parameter levels increase from left to right and from bottom to top.

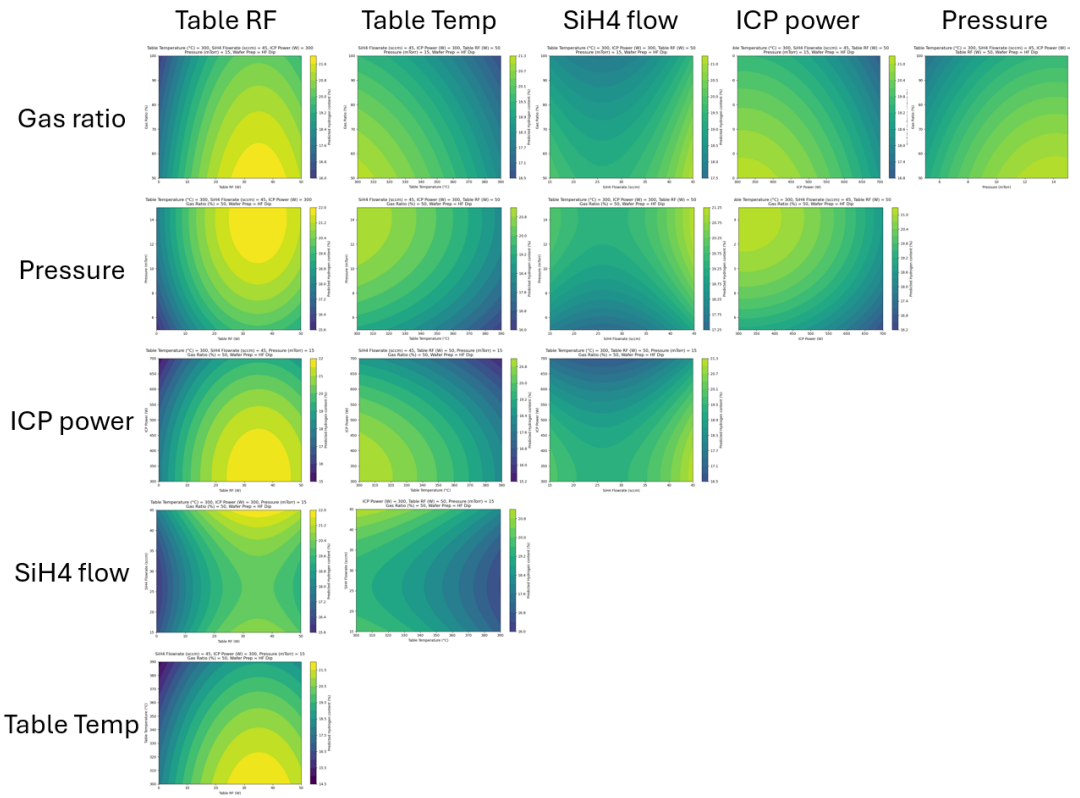

Figure B.9: Contour plots of the hydrogen content, with brighter colors indicating higher hydrogen contents. Deposition parameter levels increase from left to right and from bottom to top.

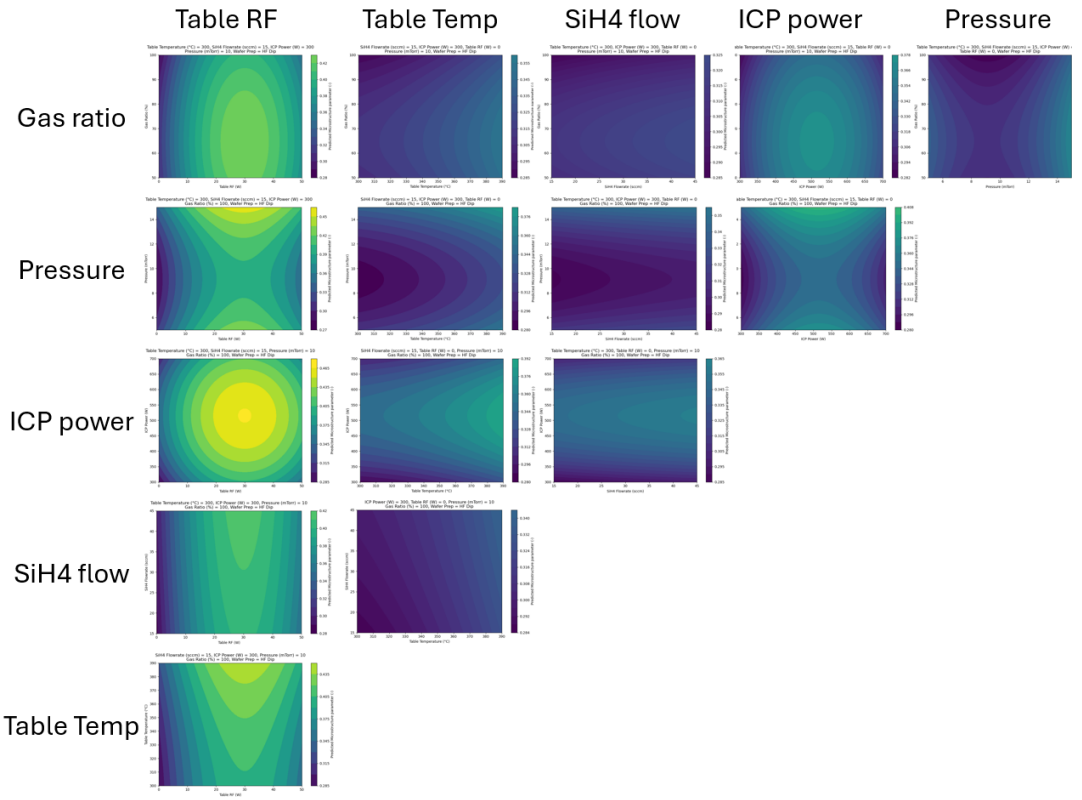

Figure B.10: Contour plots of the microstructure parameter, with brighter colors indicating higher microstructure parameters. Deposition parameter levels increase from left to right and from bottom to top.

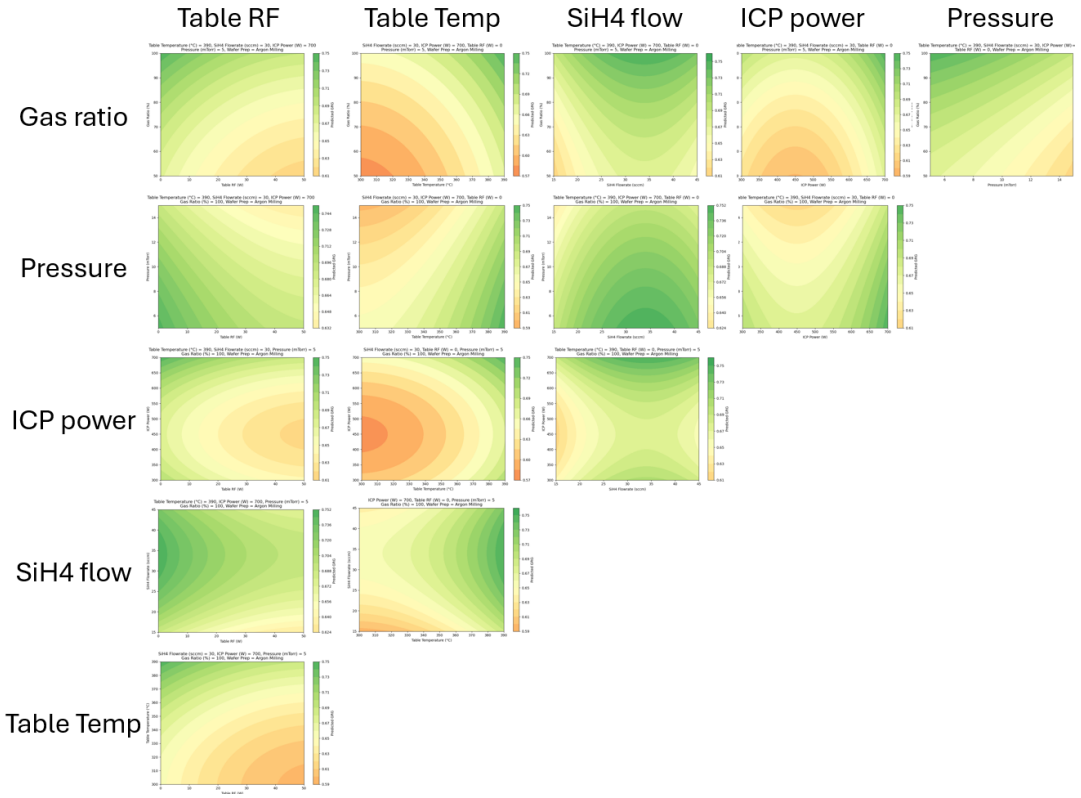

Figure B.11: Contour plots of the Grey Relational Grade of the recipe that minimizes the hydrogen content, with greener colors indicating higher Grey Relation Grades. Deposition parameter levels increase from left to right and from bottom to top.

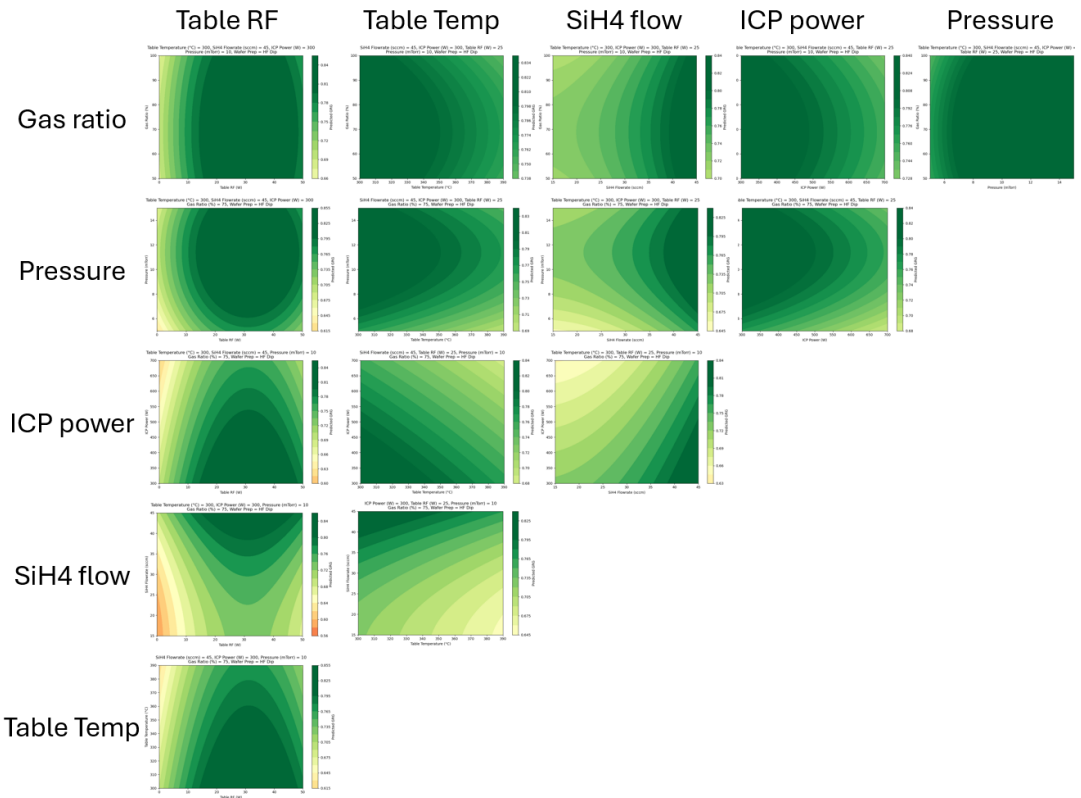

Figure B.12: Contour plots of the Grey Relational Grade of the recipe that maximizes the hydrogen content, with greener colors indicating higher Grey Relation Grades. Deposition parameter levels increase from left to right and from bottom to top.

C

Photo's of used tools in cleanroom

Figure C.1: Picture of the Oxford Instuments PlasmaPro 100 ICPCVD, the ICP-CVD tool used for the thin film depositions. This tool is located in the Else Kooi Laboratory. Next to the computer, which runs the operation software, is the loadlock. When a wafer is loaded into this loadlock, the pressure is pumped down to closely match the high vacuum of the deposition chamber before it is transferred inside. It includes two gas rings, as can be seen in Figure C.2.

Figure C.2: Chamber of the Oxford Instruments PlasmaPro 100 ICPCVD system during maintenance, with the top section lifted (see Figure C.3) to reveal the bottom half. At the center, the wafer lift is visible, which supports the wafer during processing. Two gas inlet rings are mounted along the chamber wall, through one of which argon and SiH_4 are introduced into the chamber.

Figure C.3: Top view of the Oxford Instruments PlasmaPro 100 ICPCVD chamber during maintenance. The gas inlet, used for introducing argon in this application, is clearly visible. The ICP coil, responsible for ionizing the gases to generate plasma, is located behind the chamber wall and not visible in this image.

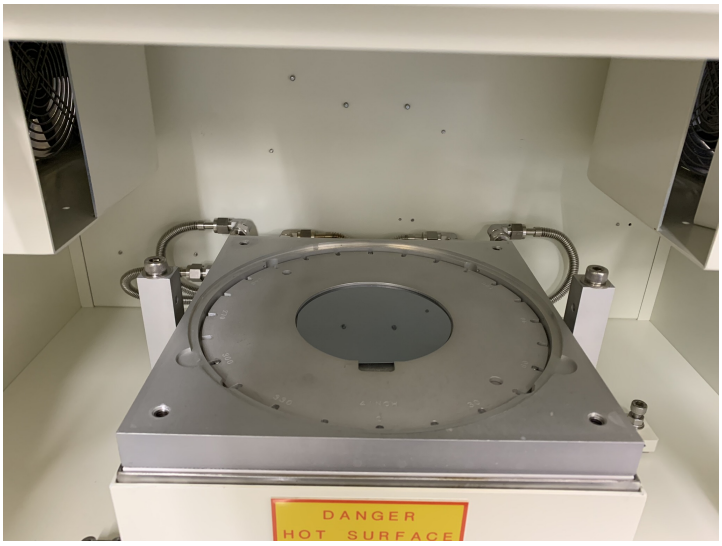

Figure C.4: Picture of the inside of the FLX-2320-S stressmeter system, located in the Else Kooi Laboratory. The wafer is placed at the center of the platform, resting on three pins to minimize contact. The orientation of the measurement is determined by the alignment ring surrounding the wafer. A laser scans along a straight line through the center of the wafer to measure its bow. By comparing the wafer bow before and after deposition, and using the film thickness, the residual stress is calculated.

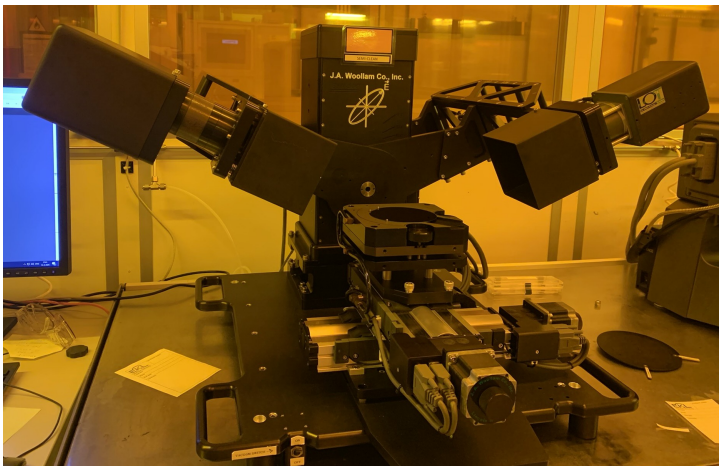

Figure C.5: Picture of the Woollam Spectroscopic Ellipsometer system, located in the Else Kooi Laboratory. In the center of the image, the wafer stage is visible. The light source and detector are mounted on the left and right arms, respectively. Prior to measurement, the wafer stage must be manually aligned to ensure that the reflected light is correctly detected.

Figure C.6: Picture of the Thermo Fischer Nicolet Fourier Transform Infrared Spectroscopy (FTIR), located in the Else Kooi Laboratory. In the center of the image, the window used to load the sample is visible. The machine has two slots: one for the sample, and the other for the reference substrate or left empty. After opening the window, it is recommended to purge the chamber with nitrogen for at least 15 minutes before starting a measurement. This step helps remove water vapor and ensures a stable background signal.

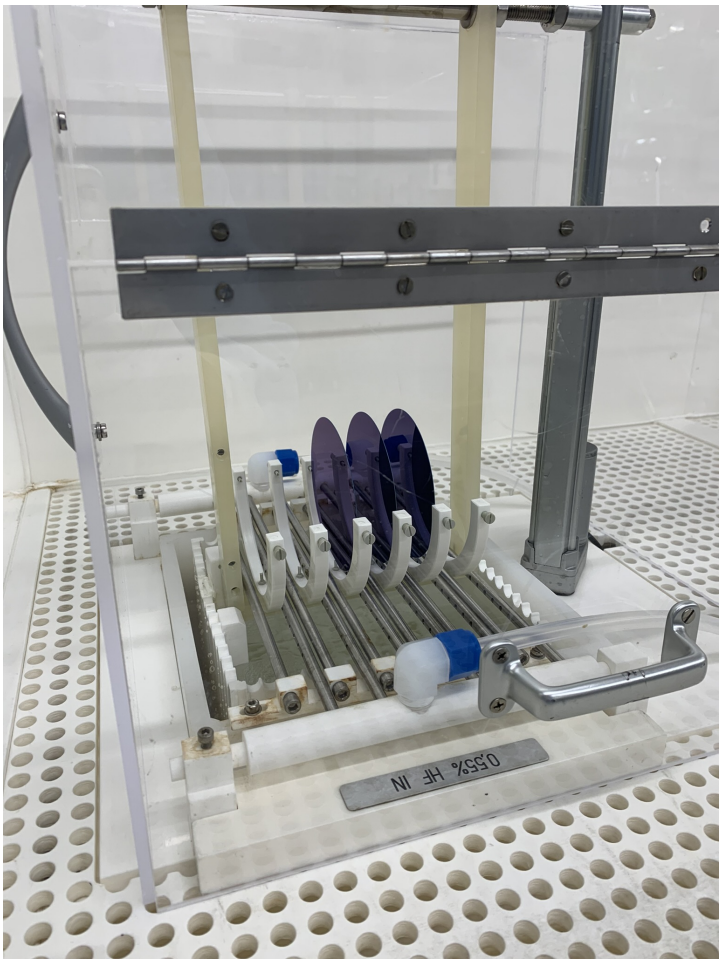

Figure C.7: Picture of the HF Marangoni Bath.The bluish color of the wafers is due to the thermal oxide layer present on the Single Side Polished wafers. The wafers are lowered into the 0.55% HF solution for 4 minutes. Afterward, the bath is rinsed, and the wafers are raised out of the solution through an IPA layer on top of the bath, which passivates the wafers for 72 hours. The procedure is explained in more detail in the flowchart in Appendix F.

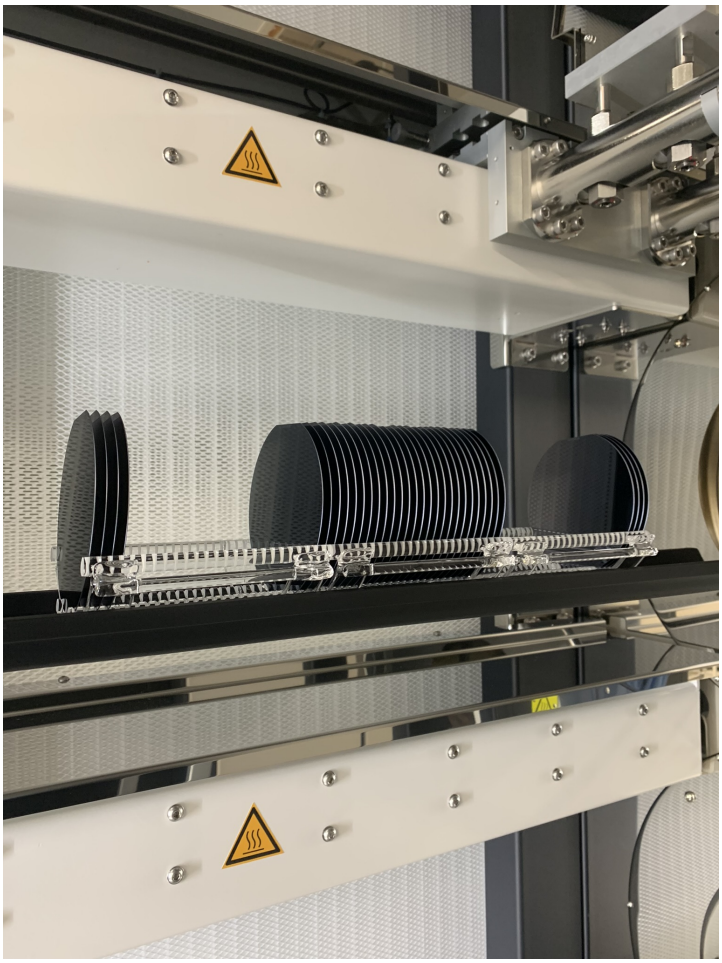

Figure C.8: Picture of the stack-furnace used to apply wet oxidation to the Single Side Polished wafers. The thermal oxide layer had an average thickness of 123 nm, measured using ellipsometry. The corresponding recipe is shown in the flowchart in Appendix F.

D

Scanning Electron Microscope photo's of cross section wafers

This appendix presents scanning electron microscope (SEM) images of the cross sections of selected films. To prepare the samples, the wafers were cleaved into 1 × 1 cm squares, which I measured edge-on together with my daily supervisor Leon. These measurements provided an independent estimate of the film thickness, used to verify the values obtained from fitting the FTIR transmission spectra.

Figure D.1 shows the SEM image of Recipe 3 deposited on a single-side polished wafer. The thermal oxide layer is clearly visible as a horizontal band and served as a convenient reference, since its thickness (116 nm) had already been measured by ellipsometry. At the upper part of the a-Si:H film, vertical structures can be seen. Similar features appear in the SEM image of Recipe 3 deposited on a double-side polished wafer (Figure D.2), suggesting that the microstructure is consistent across both substrate types. However, much of Figure D.1 also shows horizontal streaks, which are likely artifacts introduced during cleaving due to imperfections in the cross-sectional cut. An additional image of Recipe 5 on a double-side polished wafer is shown in Figure D.3. Here, finer vertical features are visible, indicating a distinct microstructure compared to Recipe 3.

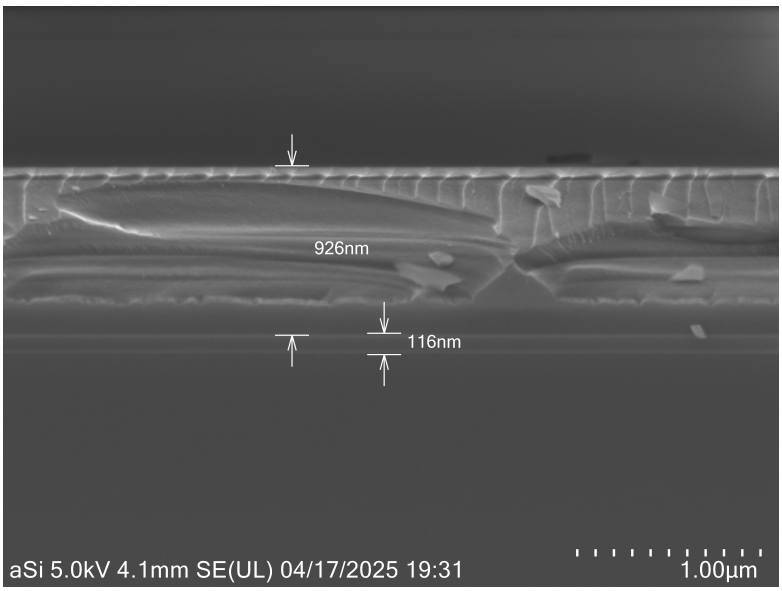

Figure D.1: Cross-sectional SEM image of the film deposited using Recipe 3 on a single-side polished (SSP) wafer. The film thickness is measured at 926 nm, and the underlying thermal oxide layer is clearly visible with a thickness of 116 nm, as verified by ellipsometry. Horizontal features in the lower part of the a-Si:H film are attributed to cleaving artifacts, while vertical features in the upper region may indicate aspects of the film's microstructure.

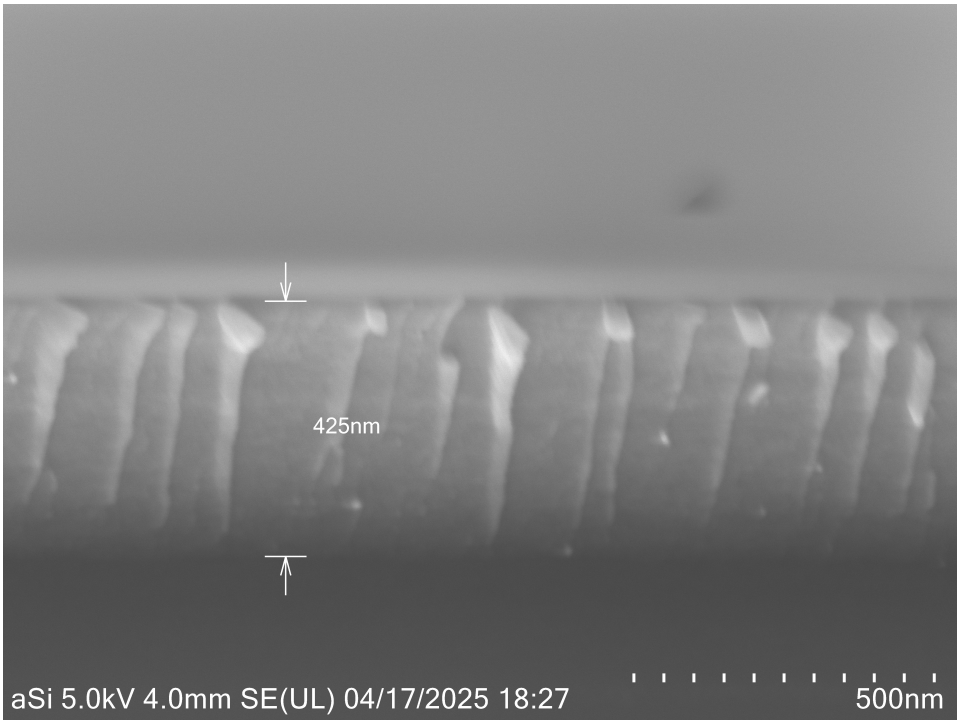

Figure D.2: Cross-sectional SEM image of the a-Si:H film deposited using Recipe 3 on a double-side polished (DSP) wafer, with a measured thickness of 425 nm. The film exhibits pronounced vertical columnar features, consistent with the microstructure observed in the corresponding single-side polished sample. These features may reflect the intrinsic growth behavior of this recipe.

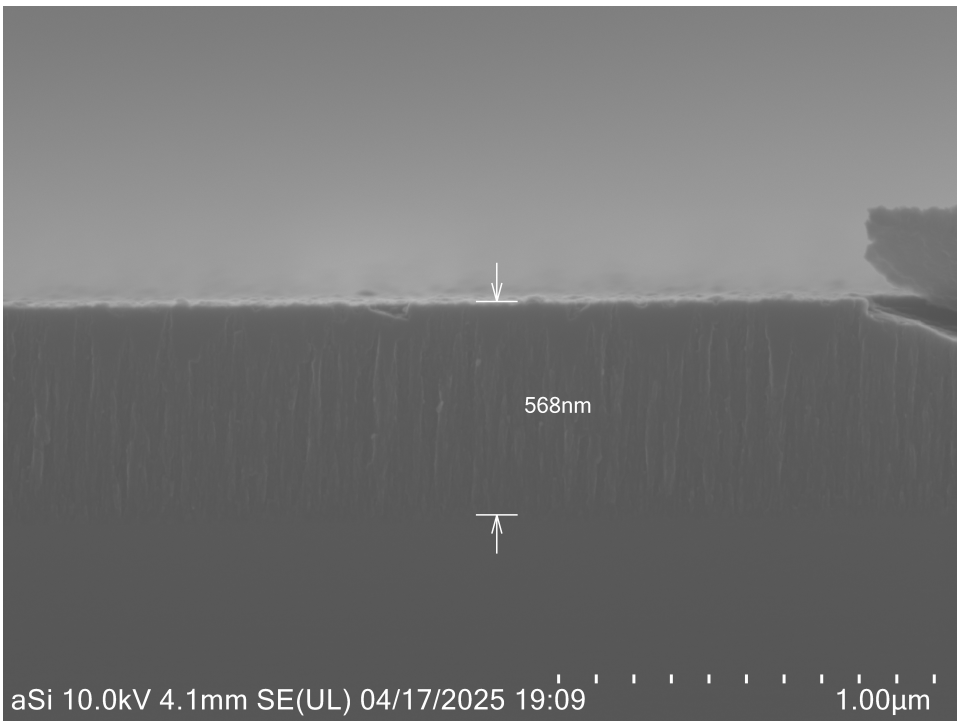

Figure D.3: Cross-sectional SEM image of the a-Si:H film deposited using Recipe 5 on a double-side polished wafer. The measured film thickness is 568 nm. The image reveals fine vertical features throughout the film. No visible cleaving artifacts are present, indicating a clean cross-section.

E

Surface appearance recipe 17

This appendix presents the surface appearance of the film deposited with wafer 17. Both a phone photograph and a microscope image of the wafer surface are included. The phone image (Figure E.1) reveals an inhomogeneous surface, described here as cloudiness. The microscope image (Figure E.2) shows a high density of small surface features. A similar, though less pronounced, surface texture was observed in the recipe identified through Grey Relational Analysis for minimizing hydrogen content.

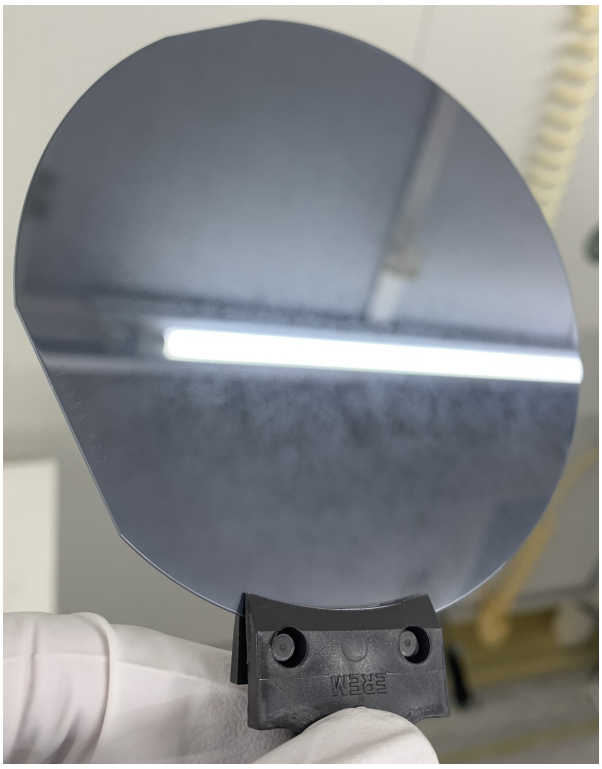

Figure E.1: Photo after deposition of recipe 17, showing cloudiness across the surface.

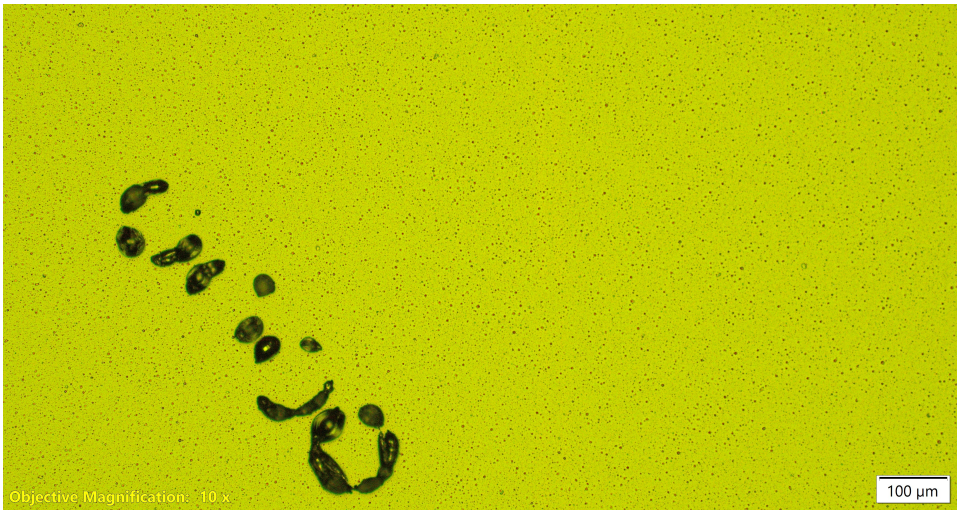

Figure E.2: Microscopic image of after deposition of recipe 17, taken at 10× magnification. The wafer exhibits a high density of fine surface features, indicative of significant surface roughness. The laser mark is also clearly visible.

F

Flowchart used at Else Kooi Laboratory

Jurre Heeringa
Optimization a-Si:H
Oxford PlasmaPro 100 ICPCVD

FLOWCHART

VERSION 1

BATCH INFORMATION			
NAME OF OWNER :	Jurre Heeringa	MASK SET :	N.A.
NAME OF MENTOR :	Leon Olde Scholtenhuis	MASK BOX :	N.A.
RUN NUMBER :	P2025-03	DIE SIZE :	N.A.
WAFER AMOUNT :	22 + 20 = 42	START DATE :	29/01/2025
SUBJECT TO PCC :	No	PCC APPROVED :	N.A.

DELFT UNIVERSITY OF TECHNOLOGY ELSE KOOI LABORATORY		
Adress	:	Feldmannweg 17, 2628 CT Delft, The Netherlands
P.O. Box	:	5053, 2600 GB Delft, The Netherlands
Phone	:	+31 - (0)15 - 2783868
Fax	:	+31 - (0)15 - 2622163
Website	:	www.tudelft.nl/ewi/onderzoek/faciliteiten/else-kooi-lab

STARTING MATERIAL

22 **SINGLE SIDE** polished **LOW RESISTIVITY** wafers, with the following specifications:

Type:	n / phosphorus
Orientation:	<100>
Resistivity:	1-20 Ωcm
Thickness:	525 ± 25 μm
Diameter:	100 mm

20 **DOUBLE SIDE** polished **HIGH RESISTIVITY** wafers, with the following specifications:

Type:	p / boron
Orientation:	<100>
Resistivity:	>1000 Ωcm
Thickness:	500 ± 15 μm
Diameter:	100 mm

1. MEASUREMENT: Native oxide thickness + model substrate **SSP wafers (all 22)** **Front side**

Use the Woollam Ellipsometer system for layer thickness measurements of the native oxide on the wafers. Try to fit a Woollam model to the optical model of these wafers.
Follow the operating instructions from the manual when using this equipment.

2. MEASUREMENT: Stress initial **SSP wafers (all 22)** **Front side**

Use the Flexus 2320-S to measure the wafer-bow of the wafers before the thermal oxidation step.
For any stress measurement, the thickness of the layer must be measured. If that is not applicable, we can still measure the wafer bow.

MY DEFINITION OF ANGLE: 0 IS 6 OCLOCK (CLOSEST TO DOOR), EASIEST TO LOAD
50 measurements is more than sufficient
Store the measurement if the following format: Recipe_nr_prior_thermal_oxidation_ID
Make sure the ID corresponds to the right wafer location in the wafer box.
Do two measurements, orientation = 0 and 90

3. CLEANING: HNO_3 99% and 69.5% **SSP wafers (all 22)** **Both sides**

Clean	10 minutes in fuming nitric acid at ambient temperature. This will dissolve organic materials. Use wet bench "HNO_3 99% (Si)" and the carrier with the white dot.
Rinse	Rinse in the Quick Dump Rinser with the standard program until the resistivity is 5 MΩ.
Clean	10 minutes in concentrated nitric acid at 110 °C. This will dissolve metal particles. Use wet bench "HNO_3 69,5% 110C (Si)" and the carrier with the white dot.
Rinse	Rinse in the Quick Dump Rinser with the standard program until the resistivity is 5 MΩ.
Dry	Use the "Avenger Ultra-Pure 6" rinser/dryer with the standard program, and the white carrier with a red dot.

4. DRY OR WET OXIDATION: 110 nm thermal SiO_2 on **SSP wafers (all 22)** **Both sides**

Need to choose which process to run, depends on time schedule cleanroom-employee.
THERE IS A NEW FURNACE STACK, MAX-TEMP IS 1050, HAVE RECALCULATED THE DURATIONS!

Furnace tube: **D1** Program name: **DRY1100/WET1100** Total time: 203 min + oxidation time

PROCESS	TEMPERATURE (in °C)	GASSES & FLOWS (in liter/min)	TIME (in minutes)	REMARKS
boat in	600	nitrogen: 8.0	5	
stabilize	600	nitrogen: 6.0	10	
heat up	+10 °C/min	nitrogen: 6.0	50	
stabilize	1050	nitrogen: 6.0	10	
purge	1050	nitrogen: 2.0 oxygen: 4.0	1	Wet oxidation only
oxidation	1050	hydrogen: 4.25 oxygen: 2.50	1	Wet oxidation only
oxidation	1050	Wet: hydrogen: 8.50 Wet: oxygen: 5.00 Dry: oxygen 6	Dry: 1:59:29 Wet: 0:6:8	DURATION FOR TEMP = 1050
purge	1050	oxygen: 9.0	1	Wet oxidation only
cool down	-10 °C/min	nitrogen: 6.0	120	wait for operator
boat out	600	nitrogen: 6.0	5	

Oxidation time:
Use an oxide growth calculator to calculate the oxidation time that is needed to reach the desired thickness.
Check out cleanroom.byu.edu/OxideTimeCalc or www.lelandstanfordjunior.com/thermaloxide.html.
Then input the calculated time at the variable command line of the **WETOX** recipe.

5. MEASUREMENT: Ellipsometer Thermal oxide thickness + model **SSP wafers (all 22)** **Front side**

Use the Woollam Ellipsometer system for layer thickness measurements of the thermal oxide on the wafers. Try to fit a Woollam model to the optical model of these wafers, as this is important to properly characterize the a-Si:H onto this substrate. Follow the operating instructions from the manual when using this equipment.

6. MEASUREMENT: Stress after Thermal oxidation **SSP wafers (all 22)** **Front side**

Use the Flexus 2320-S to measure the wafer-bow of the wafers after the Thermal oxidation step.
For any stress measurement, the thickness of the layer must be measured. If that is not applicable, we can still measure the wafer bow.

MY DEFINITION OF ANGLE: 0 IS 6 OCLOCK (CLOSEST TO DOOR), EASIEST TO LOAD
50 measurements is more than sufficient
Store the measurement if the following format: Recipe_nr_after_thermal_oxidation_ID
Make sure the ID corresponds to the right wafer location in the wafer box.
Do two measurements, orientation = 0 and 90

7. ICP-PECVD: ARGON MILLING TEST **SSP wafers 19 – 22** **Front side**

Use the Oxford PlasmaPro 100 ICPCVD reactor.

I may adjust the recipe-parameters to finetune the recipe.

Argon milling ICPECVD	
Recipe	Jurre 300C Argon milling
Etch duration:	5 – 10 min
Argon flow:	30 sccm
SiH4 flow:	N.A.
Chamber Pressure:	15 sccm
Chamber Heater:	60C
Ring Heater:	60C
Table Temperature:	300C
ICP RF:	800W
Table RF:	50W

8. MEASUREMENT: Stress after Argon Milling test **SSP wafers 19 – 22** **Front side**

Use the Flexus 2320-S to measure the wafer-bow of the wafers after the Argon milling test.
For any stress measurement, the thickness of the layer must be measured. If that is not applicable, we can still measure the wafer bow.

MY DEFINITION OF ANGLE: 0 IS 6 OCLOCK (CLOSEST TO DOOR), EASIEST TO LOAD
50 measurements is more than sufficient
Store the measurement if the following format: Recipe_nr_after_ArgonMilling_ID
Make sure the ID corresponds to the right wafer location in the wafer box.
Do two measurements, orientation = 0 and 90

9. MEASUREMENT: Ellipsometer Thermal oxide thickness + model **SSP wafers 19 – 22** **Front side**

Use the Woollam Ellipsometer system for layer thickness measurements of the thermal oxide on the wafers. Try to fit a Woollam model to the optical model of these wafers.
Follow the operating instructions from the manual when using this equipment.

Calculate the etch rate of the Argon milling test.
Use this rate to compute the duration of the Argon milling step prior to deposition.

Francesco questioned if the surface of the wafer will be flat enough after the Ar milling to have a good fitting of the ellipsometer thickness. When the fitting fails, consider adding an extra 'roughness-parameter'.

10. WET ETCHING: 'Native oxide removal' with Marangoni drying **SSP wafers 1-9** **Both sides**

Dip the wafers (with thermal oxide layer) in the HF Marangoni Si Bath. The goal of this Marangoni step is to ensure consistency with the DSP wafers for which the native oxide layer will be removed by this same procedure.
Follow the standard procedure as indicated on the on the operation manual.
The etch rate of thermal oxide is 2.2-3.3 nm/min, as seen in a catalogue located in the cleanroom.

Etch Read the Marangoni manual and follow all the instructions.

Use the Marangoni wet etch & drying system for **Si wafers.**
After rinsing the bath with DI water, fill it up with a "0.55% HF" solution (at room temperature), and lift up the wafer carrier.

Time — Place the wafers in the carrier slots and lower them into the solution for 4 minutes.

Rinse — Open the DI water valve to rinse the wafers for 5 minutes.

Dry — One minute before lifting up the wafers, open the IPA valve.
Lift up the wafers and remove the dried wafers from the carrier slots.
Close all valves and lower the empty wafer carrier into the DI water.

Note: **Deposition must be performed within 72 hours.**

Calculate what the expected thickness of the remaining oxide layer is.

11. MEASUREMENT: Thermal oxide thickness + model substrate — **SSP wafers 1 – 9** — **Front side**

Use the Woollam Ellipsometer system for layer thickness measurements of the thermal oxide on the wafers. Try to fit a Woollam model to the optical model of these wafers, as this is important to properly characterize the a-Si:H onto this substrate. Follow the operating instructions from the manual when using this equipment.

12. MEASUREMENT: Stress after Marangoni — **SSP wafers 1 – 9** — **Front side**

Use the Flexus 2320-S to measure the wafer-bow of the substrate before the deposition of the a-Si:H layer.
For any stress measurement, the thickness of the layer must be measured. If that is not applicable, we can still measure the wafer bow.

MY DEFINITION OF ANGLE: 0 IS 6 OCLOCK (CLOSEST TO DOOR), EASIEST TO LOAD
50 measurements is more than sufficient
Store the measurement if the following format: Recipe_nr_after_Marangoni_ID
Make sure the ID corresponds to the right wafer location in the wafer box.
Do two measurements, orientation = 0 and 90

13. ICP-PECVD DEPOSITION: a-Si:H — **SSP wafers 1 – 18** — **Front side**

Check if the Marangoni step was less than 72 hours ago. Otherwise this step has to be repeated before this deposition step.
THIS MEANS THE THERMAL OXIDE THICKNESS CHANGES, MEASURE THE THICKNESS AGAIN!

Use the Oxford PlasmaPro 100 ICPCVD reactor.

After

a-Si:H deposition ICPECVD			**Target Thickness = 400 nm**
1.	**Argon milling**	See recipe table, if extra argon milling phase is required	
2.	**a-Si:H Deposition**	**Recipe:**	See recipe Table
		Deposition time:	See recipe Table
		Argon flow:	See recipe Table
		SiH4 flow:	See recipe Table
		Chamber Pressure:	See recipe Table
		Chamber Heater:	See recipe Table
		Ring Heater:	See recipe Table
		Table Temperature:	See recipe Table
		ICP RF:	See recipe Table
		Table RF:	See recipe Table

the deposition recipes, run the 'Plasma Short Clean'!

14. MEASUREMENT: Stress after the deposition — **SSP wafers 1 – 18** — **Front side**

Use the Flexus 2320-S to measure the wafer-bow of the substrate + a-Si:H layer after the deposition.
For any stress measurement, the thickness of the layer must be measured. If that is not applicable, we can still measure the wafer bow.

MY DEFINITION OF ANGLE: 0 IS 6 OCLOCK (CLOSEST TO DOOR), EASIEST TO LOAD
50 measurements is more than sufficient
Store the measurement if the following format: Recipe_nr_after_Deposition_ID
Make sure the ID corresponds to the right wafer location in the wafer box.
Do two measurements, orientation = 0 and 90

15. MEASUREMENT: Thickness + material properties of a-Si:H **SSP wafers 1 – 18** **Front side**

Use the Woollam Ellipsometer system for layer thickness measurements of the a-Si:H layer on the wafers. Try to fit a model to the optical model of these wafers. With this model we can deduce the material properties of the a-Si:H layer.
Export the raw measurements via email/surfdrive, so I can analyze the data via the remote desktops of the Kavli cleanroom at home.
When modeling, first make a copy of the raw data. Therefore the data will not be lost!

Next: Process the DSP wafers Lasermark on FRONTside

16. MEASUREMENT: Native oxide thickness + model substrate **DSP wafers (all 20)** **Front side**

Use the Woollam Ellipsometer system for layer thickness measurements of the native oxide on the DSP wafers. Try to fit a Woollam model to the optical model of these wafers.
Follow the operating instructions from the manual when using this equipment.

17. MEASUREMENT: Stress initial DSP **DSP wafers (all 20)** **Front side**

Use the Flexus 2320-S to measure the wafer-bow of the DSP wafers before the Marangoni bath.
For any stress measurement, the thickness of the layer must be measured. If that is not applicable, we can still measure the wafer bow.

MY DEFINITION OF ANGLE: 0 IS **6** OCLOCK (**CLOSEST TO** DOOR)**, EASIEST TO LOAD**
50 measurements is more than sufficient
Store the measurement if the following format: DSP_Recipe_nr_initial_ID
Make sure the ID corresponds to the right **wafer location in the wafer box.**
Do two measurements, orientation = 0 and 90

18. WET ETCHING: Native oxide removal with Marangoni drying **DSP wafers 1 - 9** **Both sides**

Dip the wafers in the HF Marangoni Si Bath. The goal of this Marangoni step is to remove the native oxide layer.
Follow the standard procedure as indicated on the on the operation manual.

Etch	Read the Marangoni manual and follow all the instructions. Use the Marangoni wet etch & drying system for **Si wafers.** After rinsing the bath with DI water, fill it up with a "0.55% HF" solution (at room temperature), and lift up the wafer carrier.
Time	Place the wafers in the carrier slots and lower them into the solution for 4 minutes.
Rinse	Open the DI water valve to rinse the wafers for 5 minutes.
Dry	One minute before lifting up the wafers, open the IPA valve. Lift up the wafers and remove the dried wafers from the carrier slots. Close all valves and lower the empty wafer carrier into the DI water.

Note: **Deposition must be performed within 72 hours.**

19. ICP-PECVD DEPOSITION: a-Si:H **DSP wafers 1 – 18** **Front side**

Check if the Marangoni step was less than 72 hours ago. Otherwise this step has to be repeated before this deposition step.
Use the Oxford PlasmaPro 100 ICPCVD reactor.
After the deposition recipes, run the 'Plasma Short Clean'

a-Si:H deposition ICPECVD			**Target Thickness = 400 nm**
3.	**Argon milling**	See recipe table, if extra argon milling phase is required	
4.	**a-Si:H Deposition**	**Recipe:**	See recipe Table
		Deposition time:	See recipe Table
		Argon flow:	See recipe Table
		SiH4 flow:	See recipe Table
		Chamber Pressure:	See recipe Table
		Chamber Heater:	See recipe Table
		Ring Heater:	See recipe Table
		Table Temperature:	See recipe Table
		ICP RF:	See recipe Table
		Table RF:	See recipe Table

20. MEASUREMENT: Stress after the deposition **SSP wafers 1 – 18** **Front side**

Use the Flexus 2320-S to measure the wafer-bow of the substrate + a-Si:H layer after the deposition.
For any stress measurement, the thickness of the layer must be measured. If that is not applicable, we can still measure the wafer bow.

MY DEFINITION OF ANGLE: 0 IS 6 OCLOCK (CLOSEST TO DOOR), EASIEST TO LOAD
50 measurements is more than sufficient
Store the measurement if the following format: DSP_Recipe_nr_after_Deposition_ID
Make sure the ID corresponds to the right wafer location in the wafer box.
Do two measurements, orientation = 0 and 90

21. MEASUREMENT: Thickness + material properties of a-Si:H **SSP wafers 1 – 18** **Front side**

Use the Woollam Ellipsometer system for layer thickness measurements of the a-Si:H layer on the wafers. Try to fit a model to the optical model of these wafers. With this model we can deduce the material properties of the a-Si:H layer.

However, characterizing a-Si:H on top of a DSP c-Si wafer, WITH removal of the native oxide layer will be challenging. Keep that in mind for the interpretation of the results!

Export the raw measurements via email/surfdrive, so I can analyze the data via the remote desktops of the Kavli cleanroom at home.
When modeling, first make a copy of the raw data. Therefore the data will not be lost!

22. CLEAVING/DICING: Divide each wafer in quarters **SSP wafers 1 – 18 + 19 (ref. sample)** **Front side**

ONLY DO THIS STEP IF THE DATA ANAYSIS OF THE ELLIPSOMETER IS SUCCESFUL!

This step is necessary to make measurements with the FTIR, located at the CR10000. Whole wafers do not fit in the sample holder of the machine.

Perform this step only at the allocated locations in the cleanroom.
Store the quarter wafers in transparent boxes. This will require temporary use of 3 extra transparent boxes from EKL.

23. MEASUREMENT: FTIR **SSP wafers 1 – 18 + 19 (ref. sample)** **Front side**

Use the FTIR (Fourier Transform Infrared Spectroscopy), to measure the transmission through the substrate + a-Si:H layer.

Use wafer 19 as a reference sample!

FLUSH THE CHAMBER WITH NITROGEN, WAIT AT LEAST 15 MINUTES BEFORE START EXPERIMENT

Export the data onto a USB-stick to do the data analysis with the python code written by Bruno Buijtendorp.
For the full step-by-step procedure, check the Obsidian file named “Cleanroom experimental plan”.